

UNIVERSITY OF OKLAHOMA
GRADUATE COLLEGE

ENGINEERING A PEPTIDE-BASED TOOL FOR BIOMEDICAL APPLICATIONS

A DISSERTATION
SUBMITTED TO THE GRADUATE FACULTY
in partial fulfillment of the requirements for the
Degree of
DOCTOR OF PHILOSOPHY

By

SEREN HAMSICI
Norman, Oklahoma
2022

ENGINEERING A PEPTIDE-BASED TOOL FOR BIOMEDICAL APPLICATIONS

A DISSERTATION APPROVED FOR THE
STEPHENSON SCHOOL OF BIOMEDICAL ENGINEERING

BY THE COMMITTEE CONSISTING OF

Dr. Handan Acar, Chair

Dr. Stefan Wilhelm

Dr. Qinggong Tang

Dr. Shanteri Singh

Acknowledgments

I would like to thank Dr. Acar for her support and guidance throughout my PhD studies. I have a deep gratitude to Dr. Acar for her patience and feedbacks during my PhD. This four-year helped me to improve myself both mentally and scientifically. Also, I'd like to acknowledge my thesis committee members Dr. Stefan Wilhelm, Dr. Qinggong Tang and Dr. Shanteri Singh for their fruitful discussions.

I would like to express my special thanks to Gokhan Gunay for not only contribution to my studies and but also for his support, love, and encouragement. I would never forget all beautiful moments that we catch even in stressful and difficult times.

Finally, I would like to thank all undergraduate students in AcarLab especially Advika Kamatar and Ofelya Baghdasaryan for being a wonderful lab mate.

TABLE OF CONTENTS

ABSTRACT	xii
CHAPTER 1. INTRODUCTION	1
1.1 Protein Mimetic Peptides for Bio-material Design	2
1.1.1. Peptides are Composed of Amino Acids	3
1.1.2 Amyloid-like Peptides	6
1.1.2.1 Kinetics of Amyloid Fibril Formation	7
1.1.2.2 Design Considerations of Amyloid-like Peptides	9
1.1.2.3 Co-assembling Peptides	10
1.1.2.4 Amyloid-like Peptides for Biomedical Applications	12
1.1.2.4.1 The Relationship between Aggregation and Toxicity	14
1.2 Characterization Techniques of Peptide Assembly	16
1.2.1 Spectroscopic Methods	16
1.3.1 Fluorescence-based Methods	19
CHAPTER 2. PEPTIDE FRAMEWORK FOR SCREENING THE EFFECT OF AMINO ACIDS ON ASSEMBLY	23
2.1 INTRODUCTION	24
2.2 RESULTS	26
2.2.1 Co-assembled Peptide Design and Validation with Molecular Dynamics	26
2.2.2 Co-assembled Peptide Characterization	37
2.2.2.1 Co-assembly of Peptides into 1D Structures	37
2.2.2.2 Characterization of Assembly Kinetics and Mechanism	38
2.2.2.3 Secondary Structure Analysis of 1D Structures	43
2.2.3 Mechanical Properties of Co-assembled Peptides	47
2.3 DISCUSSION	51
2.4 CONCLUSIONS	57
2.5 MATERIALS AND METHODS	59
CHAPTER 3. CONTROLLABLE MEMBRANE DAMAGE BY TUNABLE AGGREGATION	64
3.1 INTRODUCTION	65
3.2 RESULTS AND DISCUSSION	68
3.2.1 Peptide Design and Aggregation Analysis	68
3.2.2 Cell Viability Analysis	73
3.2.3 Cell Membrane Rupture through Peptide Aggregation	75
3.2.4 Integration of [II] Peptides into Liposome Membranes	79
3.2.5 Controlling Peptide Aggregation Kinetics	82
3.2.6 Delayed Aggregation Increased the Lipid Membrane Integration of [II]	89

3.2.7	Fret Analysis for Albumin and [II] Interactions	92
3.2.8	Aggregation of [II] Induces Cell Stress	95
3.3	CONCLUSIONS	98
3.4	MATERIALS AND METHODS.....	99
CHAPTER 4. MODULATING PEPTIDE AGGREGATION KINETICS		110
4.1	INTRODUCTION	111
4.2	RESULTS AND DISCUSSION	115
4.2.1	The Change of Peptide Aggregation Kinetics Affects Cellular Viability	115
4.2.2	Cell Membrane Damage Modulated through Control of [II] Aggregation ...	117
4.2.3	DAMP Release with Peptide Aggregation	119
4.2.4	The Change of Peptide Aggregation Kinetics Affects the Antibody Levels in Vaccine Applications	120
4.2.5	Controlled Peptide Aggregation for Controlling the Cellular Immunity	123
4.3	CONCLUSIONS	124
4.4	MATERIALS AND METHODS.....	125
CHAPTER 5. CONCLUSIONS AND FUTURE PERSPECTIVES.....		131
REFERENCES.....		135

LIST OF FIGURES

Figure 1. 1 Twenty natural amino acids. Classifications with their name and one letter abbreviations. Reproduced with the permission from 1	4
Figure 1. 2 Non-covalent interactions during the assembly process. Electrostatic and hydrophobic interactions interactions, hydrogen bonding and p-stacking were illustrated.	5
Figure 1. 3 A schematic of energy landscape of amyloid folding (purple) and fibril formation (pink). Top part of the funnel represent the highest free energy. During folding process (purple part), free energy decreases and results in native state of folded protein. In the case of off-pathway folding (pink part), the lowest free energy observed in fibrillar form of amyloid, which yields the most stable thermodynamic state. Reproduced with permission from ²¹	8
Figure 1. 4 The kinetics of amyloid fibrillization follows a sigmoidal kinetic curve. There are three steps involving in kinetics which are lag phase, growth phase and saturation phase. Reproduced with permission from ¹	9
Figure 1. 5 A schematic showing three different co-assembly strategy. Individual components are assembled separately in the presence of one another during orthogonal (self-sorting) co-assembly (a). Building blocks in cooperative co-assembly are very similar with each other and interact one another with donor and acceptor molecules in the sequence (b). Components in disruptive co-assembly incorporate partially and one of the components is disrupted by the other (c). Reproduced with the permission from ³⁶	11
Figure 2. 1 CoOP design composed of oppositely charged hexapeptide units which represent the minimalistic assembly template. Schematic description of peptide co-assembly triggered by oppositely charged hexapeptides (A). Chemical representation of hexapeptides (B). E and K residues at both ends provided electrostatic interactions, FF at the core contributed self-assembly with π -stacking and replacing [XX] with either dialanine, ditryptophan or diisoleucine to enable tunable hydrophobic interactions.	29
Figure 2. 2 Free energy surfaces of three co-assembly systems from a metadynamics calculation. r is average distance between all centers of mass and R_g is the average radii of gyration (both only consider backbone atoms). Panels A-C show free energy as computed via the metadynamics bias. Panel D shows the integrated free energy surface along the average distance. This plot does not predict the occurrence of self-assembly but is instead a measure of solvated peptide aggregation.	30
Figure 2. 3 Free energy of intra- and inter-chain contact between amino acids in the WW sequence. Contact is defined as there being a pair of two heavy atoms in an amino acid within 3.5 \AA . These are computed from a single 392 ns simulation via $F = -kT \ln P(c)$. No enhanced sampling was used, so should not be numerically comparable with main text due to inefficient sampling.	32
Figure 2. 4 Free energy of intra- and inter-chain contact between amino acids. Contact is defined as there is a pair of two side-chain heavy atoms in an amino acid within 3.5 \AA . These are computed via reweighting the metadynamics simulations. (Bigger size of circles and lighter color defines lower free energy, higher probability of contact).	33

Figure 2. 5 Probability of first contacting residues from 40 unbiased molecular dynamics simulations. Contact is defined as there being a pair of two side-chain heavy atoms in an amino acids within 3.5 Å°. Simulations ended at a four-chain aggregate and began with the chains at least 2.5 nm apart. Working from end, this plot shows the minimum non-zero contact maps averaged across the 40 simulations. (Lighter color represent more contact).	36
Figure 2. 6 Secondary structure of peptides at initial contact. Coil is random coil, Strand includes beta-sheet forming dihedral angles. Reweighted as described in maintext.	36
Figure 2. 7 Zeta potential measurements. Individual positively and negatively charged peptides and 1:1 (molar ratio) mixed forms.	38
Figure 2. 8 Morphological analysis of peptide structures. AFM images of CoOPs. Diameter analysis of [AA], [WW] and [II].	38
Figure 2. 9 Hydrogel formation and 1D nanofibrillar assembly kinetics. Upon mixing two oppositely charged peptides, [II] and [WW] formed gels (A) consisting of nanofibers (B) while [AA] did not form any organized structure (A,B). Molecular co-assembly of the peptides was characterized by CAC determination (C). Characterization of amyloid-like aggregation mechanism probed by congo red assay for two days (D) 40	40
Figure 2. 10 Determination of aggregation concentration of CoOPs. Dynamic light scattering (DLS) measurements were performed by co-assembled peptides with immediate incubation.	41
Figure 2. 11 DLS measurements of CoOPs. DLS measurements were performed by co-assembled peptides with overnight incubation.	42
Figure 2. 12 DLS measurements of single peptides. DLS measurements were performed with freshly prepared and overnight incubated samples for both positively (A) and negatively (B) charged peptides at 500 μM.	43
Figure 2. 13 Structural determination of CoOPs. Secondary structure analysis of CoOPs and the individual counterparts in water with different concentrations by using FTIR and CD measurements (A,B))	45
Figure 2. 14 Secondary structure analysis CoOPs. Positively (A) and negatively charged (B) individual peptides in water by using FTIR.	47
Figure 2. 15 Mechanical characterization of CoOPs. Time sweep and strain sweep tests of [AA], [WW] and [II] for immediate analysis.	48
Figure 2. 16 Mechanical characterization of CoOPs. Time sweep and strain sweep tests of [AA], [WW] and [II] for overnight characterization.	48
Figure 2. 17 Storage modulus of [WW] and [II]. One phase association of storage modulus of [WW] and [II] during 20 min.	50
Figure 3. 1 Peptide groups and aggregation kinetics. (A) CoOP groups and individual counterparts were used in this study. (B) CAC of co-assembled peptides with DPH. (C) Macroscopic CoOP aggregates incubated with Congo Red. (D) Determination of aggregation kinetics of CoOPs and (E) individual counterparts by ThT assay. Data are representative of three experiments.	69
Figure 3. 2. LC and MS analysis of [LL] and [VV] peptides. The exact molecular weight of KFFVVK: 765.49, KFFLLK:793.52 , EFFVVE: 809.4 , EFFLLE: 837.43.	70

Figure 3. 3 Morphological analysis of peptide structures. TEM images of [VV], [WW], [LL] and [II] peptides. Scale bar: 500 nm.....	72
Figure 3. 4 Cytotoxicity of peptides to ovcar-8 cells. Negative peptides were added to the cells, followed by corresponding positive peptides. (A) live-dead images of ovcar-8 cells treated with peptide combinations and corresponding individual counterparts at 6h (peptide concentration is 0.5 mM) (B) zeta potential of individual and combined peptides. (C) illustration of peptide preparation for [WW] and [II]. The effect of peptide preparation on cell viability for [WW] (D) and [II] (E). The scale bar is 200 μ m. Data are representative of at least three experiments. Statistical analysis via one-way anova test, data are mean \pm sd, ****p<0.0001.	76
Figure 3. 5 [II] induces membrane rupture. (A) time and concentration-dependent cell membrane damage of [II] were analyzed through pi uptake (scale bar is 100 μ m). (B) time-dependent viability measurement and (C) time-dependent nuclear size analysis. (d) actin cytoskeleton staining of [II] treated ovcar-8 cells at 1,3 and 6h, scale bar is 20 μ m. (e) internalization of FITC-KFFIIK and (f) FITC-[II] for 1, 3 and 6h, scale bar is 100 μ m. Data are representative of at least three experiments. Statistical analysis was done with one-way anova test. Data are mean \pm sd, ****p<0.0001.....	78
Figure 3. 6 Liposome diameters. Films of agarose enable rapid formation of giant liposomes having around 100 μ m in diameter.....	79
Figure 3. 7 Characterization of peptides after purification. LC and MS analysis of KFFIIK and EFFIIE peptides.....	80
Figure 3. 8 Liposome (blue) membrane integration of [II] and individual peptides; KFFIIK (green), EFFIIE (red). (A) The schematic of membrane localization experiment by using agarose embedded liposomes. (B) Membrane localization of 30 min premixed of EFFIIE+KFFIIK. (C) EFFIIE addition followed by KFFIIK and (D) KFFIIK addition followed by EFFIIE. (Scale bar = 100 μ m).....	81
Figure 3. 9 Charge measurements. Zeta potential of individual oppositely charged peptides, co-assembled form and albumin only in PBS.	82
Figure 3. 10 Aggregation kinetics depend on albumin concentration. (A) The schematic of [II] aggregation with albumin. Aggregation kinetics performed with (B) ThT and (C) DPH assays in increasing albumin content. (D) AFM images of [II]-albumin structures (Scale bar = 100 nm). (E) DLS measurements [II]-albumin mixtures.	85
Figure 3. 11 ThT analysis of albumin and individual peptides in different concentrations. Albumin only and peptide counterparts did not give any fluorescence increase respect to time due to non-fibrillar organization.	86
Figure 3. 12 DPH analysis of albumin and albumin+[II] in different concentrations. Albumin intensity increased with increased concentration, however [II] disrupted albumin aggregation which leads to decrease in DPH intensity.	87
Figure 3. 13 DPH analysis of individual peptides in different albumin concentrations. Individual peptides did not form aggregation.....	88
Figure 3. 14 Delayed [II] aggregation increases its integration on the lipid membranes. (A) Liposomal membrane localization of 0.5 mM [II] in 0.2w% albumin; liposome = blue, EFFIIE = red, KFFIIK = green (Scale bar = 100 μ m). (B) Relative viability and (C) LDH release of EMT6 cells treated with individual and aggregates with 0.5 mM [II] in 0 and 0.2 w% of albumin in PBS.	90

Figure 3. 15 Individual peptide localization on the liposomal membrane. (A) EFFIIE and KFFIIK (B) localization on the liposomal membrane with and without 0.2w% albumin	92
Figure 3. 16 Albumin and [II] interaction. (A) The FRET analysis of the presence and absence of TRITC-albumin with FITC-KFFIIK and (B) with [II]. (C) Confocal analysis of cells treated with 0.5 mM [II] for 30 min, 1h, and 2h in the presence of 0.2 w% albumin. Membrane stained with WGA, gray; cells treated with Rhodamine B labelled EFFIIE, red; FITC labelled KFFIIK, green. (Scale bar = 10 μ m).....	94
Figure 3. 17 The treatment of cells with preincubated [II] without albumin for 1h and 2h. [II] did not accumulate on the cell membrane due to fibrillar formation.	95
Figure 3. 18 [II] aggregation on the cell membrane induces cell stress. (A) Immunocytochemistry of YAP localization (YAP = green, Actin = red, Nuclei = blue) (B) and phosphorylation based on aggregation (YAP-P = green). (C) Western blot analysis of YAP, YAP phosphorylation, eIF2 α and eIF2 α phosphorylation in different time points β -actin was used as an internal loading control. (D) Immunocytochemistry of calreticulin cell surface localization (calreticulin = green, Actin = red, Nuclei = blue). (Scale bars = 20 μ m).....	98
Figure 4. 1 The change of peptide aggregation kinetics affects the cellular viability. ThT measurement of [II] aggregation controlled through albumin concentration (A). Albumin modulates the [II] aggregation state (B). Relative viability of cells treated with 0.5 mM [II] peptide prepared in indicated albumin %w/v for 3, 6 and 24h (C).	116
Figure 4. 2 Cell membrane damage can be modulated through control of [II] peptide aggregation. LDH release of cells treated with 0.5 mM [II] peptide prepared in indicated albumin %w/v for 3, 6 and 24h (A). Schematic illustrating the effect of fibrillar networks and globular structures on the membrane damage (B). Propidium iodide staining of cells treated with 0.5 mM [II] peptide prepared in indicated albumin %w/v for 3, 6 and 24h, the scale bar is 50 μ m (C). SEM images of the cells (top row) and magnified images (bottom row) treated with 0.5mM peptide prepared in indicated albumin %w/v for 6h (D). The scale bars are 20 μ m and 5 μ m. (%w/v indicates weight/volume).....	118
Figure 4. 3 DAMP release can be modulated through control of [II] peptide aggregation. Cells were treated with 0.5mM [II] peptide in indicated albumin w/v% for 1.5, 3 and 6h. Western blot images of HMGB-1 release (A) and HSP90 release (B) at 3 and 6h. Extracellular ATP (C) and dsDNA release (D) release at 1.5, 3 and 6h. Heat map of DAMP release at 3 and 6h (E).	120
Figure 4. 4 OVA addition does not change aggregation and cell membrane damage. 10 μ g of OVA was added into the [II] peptide mixture prepared in indicated albumin w/v% and ThT measurement was carried out (A). Viability measurement at 6h with 0.5mM [II] peptide prepared in indicated albumin w/v% with and without the addition of 10 μ g OVA. Statistical analysis was done by one-way analysis of variance (ANOVA) with Tukey's multiple-comparison test, data are mean \pm SD, ns, not significant.	121
Figure 4. 5 Experimental planning of vaccination and antibody responses. Injection groups were control (only PBS), only OVA and 0.5mM [II] prepared in 0 w/v%, 0.02 w/v% and 0.2 w/v% MSA. Booster vaccinations were carried out at week 4 and 8,	

identical to first vaccination. Serum was collected to analyze antibody levels at week 3, 4, 6 and 10. Statistical analysis was done by one-way analysis of variance (ANOVA) with Tukey's multiple-comparison test, data are mean \pm SD, **** p<0.0001, *** p<0.001, ** p<0.01. 122

Figure 4. 6 Peptide aggregation induced cell death stages effect immunogenicity. Experimental design involving the treatment of EMT6 cells for 1.5 and 3h with 0.5 mM [II] peptide prepared in 0.02 w/v%, 0.2 w/v% and 2 w/v% albumin. Propidium iodide uptake (A) and ATP analysis (B) of dying cells prior to injection. Experimental design for prophylactic vaccination (C). Tumor-free mice survival graph (D). Statistical analysis was done by one-way analysis of variance (ANOVA) with Tukey's multiple-comparison test, data are mean \pm SD, **** p<0.0001, ** p<0.01, * p<0.1. 124

LIST OF TABLES

Table 2. 1 Sequences of the CoOPs used in this study. Each CoOPs has negatively and positively charged counterparts.....	27
Table 2. 2 Physical properties of CoOPs. The overall characterization of substitution domains and CAC of CoOP pairs. N/A: not available, Pho: hydrophobic, and Phi: hydrophilic	34

ABSTRACT

Numerous technological and scientific advancements have been developed by the structural organization and functional capabilities of natural materials. A field known as "biomaterials" focuses on adapting engineering concepts found in biological models to create materials that can solve enduring issues in the biomedical engineering field. The fundamental molecules in a living organism are comprised of proteins. Protein structures are guided by combined and complex intermolecular interactions of peptides which ultimately influence the functionality of proteins. Synthetic engineering approaches of peptides can overcome the limitations of the complexity of protein intermolecular interactions and provide scalable technological solutions.

In the current dissertation, an engineering platform called CoOP (co-assembled oppositely charged peptides) was introduced and studied to understand the complex intermolecular interactions of proteins. Inspired by naturally found amyloid-beta ($A\beta$) protein, a hexapeptide framework was designed to determine the effect of π -stacking, hydrophobic and electrostatic interactions. By using computational and experimental approaches, this unique framework showed the importance of electrostatic interactions to initiate peptide assembly and enhanced stability due to hydrophobic interactions. The usability of this framework was first tested by changing the hydrophobic interactions. Then, assembly kinetics and structural organizations were studied depending on hydrophobicity indexes of amino acids. It was found that the highest hydrophobicity in the framework called [II], formed by co-assembly of KFFIIK and EFFIIE, resulted in the fastest assembly kinetics, showed the most organized secondary structure and similar physical properties as in $A\beta$ protein. Given that there is a strong correlation between different

aggregated states (fibrillar or globular aggregates) and toxicity of A β , [II] platform provided to study and model these aggregated states. Similar to A β , oligomeric and fibrillar forms of [II] resulted in a difference in cell membrane damage. However, unlike A β , [II] platform was implemented to modulate the aggregation where each aggregated state provided different toxicity levels depending on biophysical features. A change in aggregation had a control over cell membrane damage, leading to differential and synergistic release of immune system-related molecules. This approach was tested with model antigen Ovalbumin, and antigen-specific antibody production was achieved based on aggregation kinetics. Furthermore, a change of aggregation of [II] was applied to the prophylactic tumor vaccine application, which shows the potential of system for cancer-related applications.

Based on the aggregation kinetics, an engineering platform, CoOP, can be applied to correlate structural changes with a biological effect. In this thesis, biological effect is limited based on the applications related to cell membrane damage. However, CoOP provides the discovery of new peptides and functionalities with an understanding of intermolecular interactions.

CHAPTER 1. INTRODUCTION

Part of this section is adapted from the following publication:

Hamsici, S., Gunay, G., Kirit, H., Kamatar, A., Loving, K., & Acar, H. (2020). Drug Delivery Applications of Peptide Materials. In *Peptide-based Biomaterials* (pp. 291-334).

Bioinspired or biomimetic materials are on the cutting edge of biological and material science, chemistry, physics and biotechnology.^{1,2} The combination of design principles inherent to these fields enables the creation of materials capable of quickly diagnosing diseases, delivering a drug directly to its target organ, presenting bioactive signals for the development of cells, regenerating tissues, and providing a vaccine platform.³⁻⁵ The scope of these efforts has been significantly broadened by recent developments in the synthesis of biomaterials, polymers, and natural or synthetic biomacromolecules, which enable the creation of multifunctional materials that induce desired biological effects due to surface chemistry, attached ligands, mechanical and physical properties.^{6,7}

For a wide range of biomedical applications, material synthesis should be low-cost, high-yield, and impurity-free. Numerous bottom-up and top-down methodologies are available to accomplish this.⁸ Top-down approaches scale down the bulk material into its component parts, whereas bottom-up approaches assemble supramolecular structures from fundamental constituents like atoms and molecules.⁹ Specifically, top-down strategies involve a miniaturization of the bulk material and require an external force such as UV light and electron beam, which can be limited because of the high cost of equipment, fabrication facilities, and control of physical parameters such as homogeneity.¹⁰ However, the bottom-up strategy allows to engineer of a nanomaterial in which the final structure is formed by the self-assembly of precursor molecules, so that control over material properties can be achieved by modifications of precursor molecules

or processing conditions.¹¹ There are many examples taking advantage of self-assembly in biological systems, including the formation of cell membranes, DNA double helix formation, and the protein folding from a polypeptide chain into tertiary and quaternary structures.⁵ Synthetic nanomaterials have been produced using nature as an inspiration by small molecular building blocks.

Peptides and peptide derivatives are particularly inspiring building blocks for the design of self-assembled materials due to the potential of exploiting of self-assembly processes in laboratory conditions.⁷ A specific advantage of synthetic peptides is that they can be generated as exact copies of protein fragments as well as in various chemical modifications, which can include the incorporation of an extensive range of non-proteinogenic amino acids, as well as the modification of the peptide backbone. Furthermore, peptide-based materials offer a variety of amino acid side chains (unlike what is currently possible with synthetic polymers) which are responsible for determining the structure, physicochemical characteristics, and biological functions.

1.1 PROTEIN MIMETIC PEPTIDES FOR BIO-MATERIAL DESIGN

Proteins are the primary functional molecules in organisms. They carry out a variety of tasks, such as acting as enzymes, hormones, membrane channels, extracellular matrix (ECM), and participating in cell signaling mechanisms.¹² ECM acts as structural support and includes a wide range of polysaccharide chains and fibrous proteins such as laminin, fibronectin, elastin and collagen, offering the biochemical and biomechanical cues for cells to proliferate, differentiate and migrate.¹³ The fundamental concept that allowed evolution to use this class of molecules for a diverse range of functions is that proteins

are biopolymers made from an infinite number of different building blocks, amino acids.¹⁴ The linear arrangement of the amino acids determines all the protein's characteristics. Still, most proteins must fold into a highly specific three-dimensional to carry out their intended function in the organism, limiting the use of proteins as a biomaterial. The other factors limiting the usefulness of protein as a biomaterial design are the complexity of preparation, instability, cost, and batch-to-batch variation.¹⁴ Therefore, instead of using a large protein, a reductionist approach known as a minimalistic design enables the identification of short peptide sequences that can organize themselves into well-ordered assemblies similar to those found in larger proteins.

1.1.1. PEPTIDES ARE COMPOSED OF AMINO ACIDS

Peptides are composed of amino acids, which consist of an alpha carbon atom, an amino group (-NH₂), a hydrogen atom (H), a carboxy group (-COOH), and a side chain. Based on their side chains, amino acids can be categorized into four groups: hydrophobic, aromatic, charged (positive and negative) and hydrophilic (polar) (Figure 1.1)

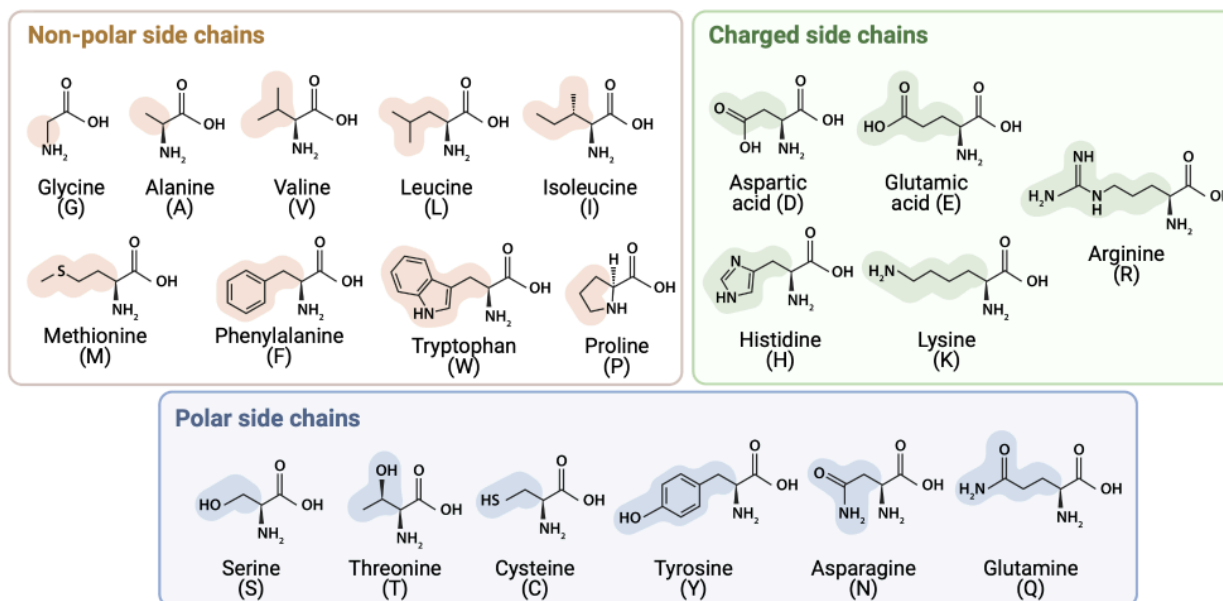


Figure 1. 1 Twenty natural amino acids. Classifications with their name and one-letter abbreviations. Generated by BioRender.

Charged side chains of amino acids (positively charged (histidine (H), lysine (K), arginine (R)) or negatively charged (aspartic acid (D) and glutamic acid (E)) can be used to modify the self-assembly to promote the aggregation by adding oppositely charged amino acids through electrostatic interactions which resulted in the salt-bridge formation, or to halt the self-assembly by introducing similar charges through repelling forces. Another significant driving force for a structural organization is hydrogen bonding, form throughout the peptide backbone between amide and carboxylate groups. Also, polar (hydrophilic) amino acids are mainly part of hydrogen bonding interactions with their backbone carbonyl and amide groups.¹⁵ The amino acids containing hydrophilic side chains are cysteine (C), serine (S), asparagine (N), threonine (T) and glutamine (Q). Hydrophobic amino acids are divided into two categories aliphatic and aromatic. Aliphatic amino acids (alanine (A), proline (P), isoleucine (I), glycine (G), leucine (L), methionine (M), and valine (V)) are those amino acids that are non-polar and create a hydrophobic environment around them.

Hydrophobicity contributes to the stabilization of the ordered peptide assemblies, and supports the growth of fibrillar formation.¹⁶ π - π interactions are another type of non-covalent interaction that defines and rule the self-assembly processes leading to the formation of supramolecular structures. π -stacking takes place between a π -electron deficient-unit and a π -electron-rich unit, which can occur between aromatic peptides (phenylalanine (F), tyrosine (Y), and tryptophan (W)).¹⁷

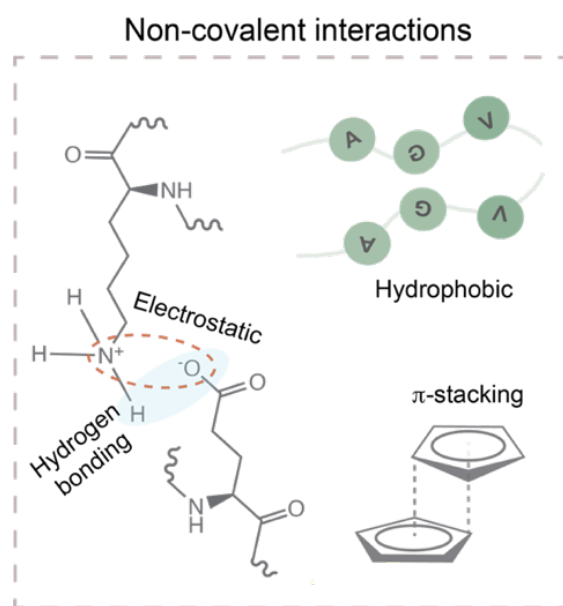


Figure 1. 2 Non-covalent interactions during the assembly process. Electrostatic and hydrophobic interactions, hydrogen bonding, and π -stacking were illustrated.

The residues impact how peptides and proteins self-assemble, influencing how these molecules are structured at the higher ordered organization levels. Also, these non-covalent interactions (Figure 1.2) work together to create a synergistic effect that determines the thermodynamic stability and the minimum energy state of the final nanostructures.¹⁸ As a result, material properties (e.g., stiffness) and functionality (e.g., bioactivity) can be modulated and result in tunable characteristics.

Unlike proteins, peptides do not fold into complex tertiary structures; instead, they may form α -helices and β -sheets, which are two main secondary structure motifs originating from intramolecular hydrogen bonding in localized regions of the sequence, producing specific arrangements of the peptide “backbone”.¹⁹ α -helices are formed as repeating helical structures involving a hydrogen bond between the carbonyl group of one amino acid and the amide group of the fourth amino acid ahead in the sequence.²⁰ As a result, amino acid side chains become exposed on each helix’s surface. Two or more α -helices can bundle together and form coiled-coil structures.²¹ On the other hand, in β -sheet structures, two or more polypeptide chains line up with each other, and hydrogen bonding occurs between carbonyl and amide groups of the peptide backbone.²² This arrangement forms either in parallel arrays (where strands point in the same direction) or in antiparallel arrays (where strands point in the opposite directions). A β -sheet-forming peptide is generally designed by using hydrophobic and hydrophilic domains. While hydrophobic segments hide themselves from the aqueous environment within the core of the self-assembled structure, the hydrophilic parts expose themselves to the aqueous environment.²³ By designing hydrophilic domains with amino acids of specific functionalities, the surface of the structure can be modified for specificity to particular tasks in certain types of cell.

The success of designing peptide structures inspires scientists to mimic the behavior of the proteins which can be complex to provide scalable technological solutions. Therefore, minimalistic versions like peptides can give rise to new technologies with tunable properties and functions instead of studying and using a whole protein.

1.1.2 AMYLOID-LIKE PEPTIDES

In more recent years, it has become apparent that a class of diseases with late onset and slow progression are caused by a gain in function brought on by a protein that has been folded abnormally.²⁴ Common neurodegenerative pathologies like Alzheimer's (AD) and Parkinson's disease (PD) are among these conditions, which are characterized by ordered, fibrillar protein aggregates known as amyloid fibrils.²⁵ β -sheet motif, which demonstrates distinct morphological and mechanical properties, is the structural hallmark of self-assembly into amyloid fibrils.

1.1.2.1 KINETICS OF AMYLOID FIBRIL FORMATION

The kinetics of amyloid fibril formation suggests a nucleation-dependent polymerization process that converts soluble monomeric forms of protein fragments (amyloid-forming peptides) into amyloid fibrils.²⁶ Overall process is explained by a funnel-like landscape kinetic energy model, in which protein folding (purple part) and amyloid fibril formation (pink part) can be seen with an energy landscape (Figure 1.3).²⁷ In this energy landscape, there are two pathways: on- and off-pathway folding.²⁷ During on-pathway folding, unfolded polypeptide chains run through several folding intermediates to reach the native folded state (purple part).²⁷ The energy landscape toward the thermodynamically advantageous native state is difficult, so molecules must overcome kinetic energy barriers to reach the native state. In the end, the highest energy states are occupied by on- or off-pathway intermediates (folding intermediates or partially folded states).²⁷

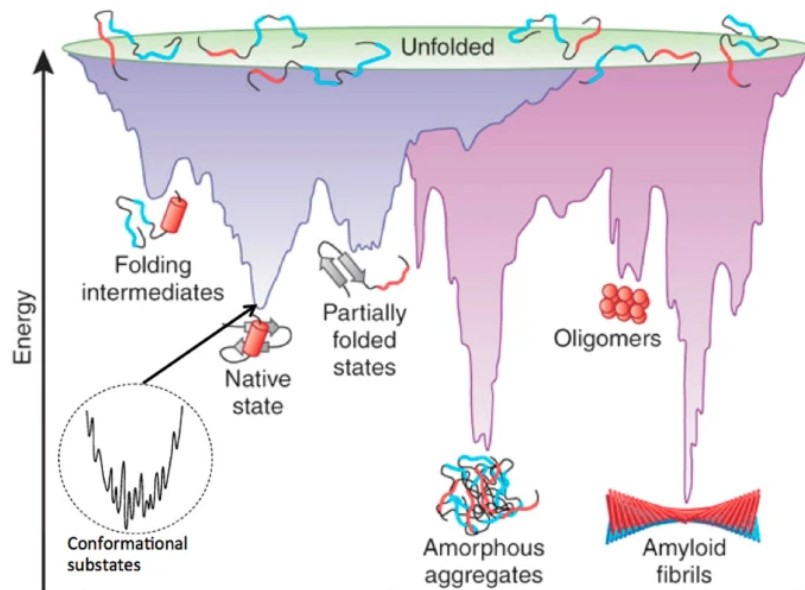


Figure 1. 3 A schematic of the energy landscape of amyloid folding (purple) and fibril formation (pink). The top part of the funnel represent the highest free energy. During folding process (purple part), free energy decreases and results in native state of folded protein. In the case of off-pathway folding (pink part), the lowest free energy observed in fibrillar form of amyloid, which yields the most stable thermodynamic state. Reproduced with permission from²⁷

In the case of amyloid fibril formation, intermolecular interactions (mainly hydrophobic forces) initiate off-pathway folding (pink part). This step begins with forming “nuclei, N ” from misfolded or unfolded proteins during the lag phase (Figure 1.4). Then, it proceeds with the formation of oligomers whose size is concentration dependent. Hence, nucleation is rate-limiting for amyloid fibril formation; the aggregation rate is expected to have a high-order dependence (the order is related to N) on protein or peptide monomer concentration. Following the lag phase, the growth phase occurs where larger aggregates of oligomers called protofibrils form. Then, protofibrils proceed with the formation of mature fibrils in the saturation phase. In addition, amyloid assemblies can bind specific amyloid dyes like Thioflavin T (explained in Section 1.3 in detail), which helps to observe the kinetics of amyloid fibril assembly.

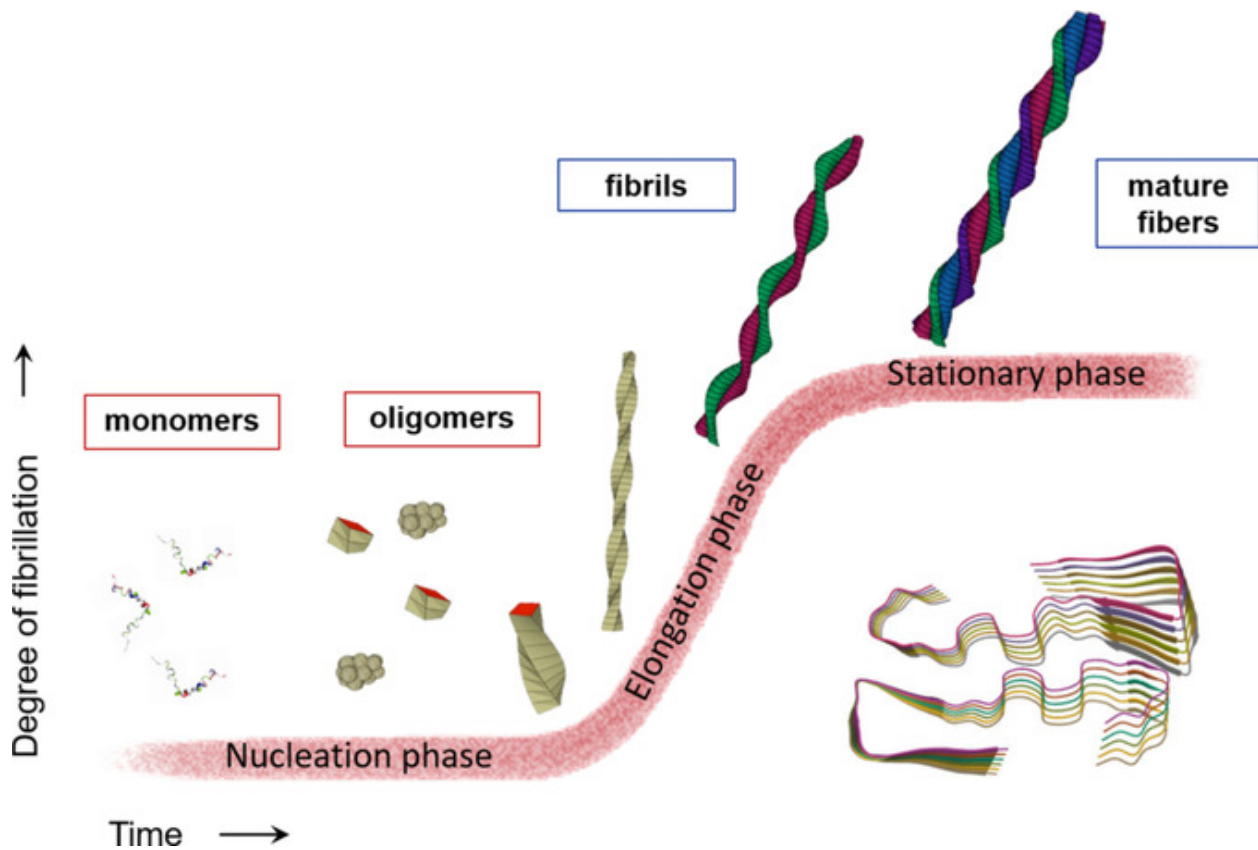


Figure 1. 4 The kinetics of amyloid fibrillization follows a sigmoidal kinetic curve. There are three steps involved in kinetics which are lag phase, growth phase and saturation phase. Reproduced with permission from²⁸

1.1.2.2 DESIGN CONSIDERATIONS OF AMYLOID-LIKE PEPTIDES

In amyloid β - peptides, the central hydrophobic domain (LVFFA) has been involved in fibril formation.²⁹ Particularly, the simplest peptide building block, FF, was found to be a core recognition motif of β - amyloid peptide.³⁰ Furthermore, in the case of type-II diabetes, it was found that while FGAIL is involved in forming fibrillar structures similar to a natural polypeptide, GAIL did not form any fibrils.³¹ Those two examples highlighted the importance of the F side chain (common in both sequences) which contributes to π - π interaction.

Besides π - π interaction, other non-covalent interactions such as hydrogen bonding, hydrophobic and electrostatic (ionic bonds) interactions can be coordinated to promote self-assembly into one-dimensional (1D) nanofibers.³² To determine some of the potential mechanisms in protein misfolding, extensive research on the amyloid formation of peptide fragments has also revealed the significance of hydrophobic interactions in short peptide assembly.³³ It was found that hydrophobic interaction occurred between Leu and Phe at the central hydrophobic domain of amyloid β - peptide (LVFFA) is another strongest driving force for self-assembly besides FF.³⁴ Furthermore, a computational analysis of all 400 natural dipeptide combinations previously demonstrated the propensity of hydrophobic residues to influence the self-assembly of short peptides.³⁵

Simplistic modifications of diphenylalanine peptides such as introducing an aromatic capping group,³⁶ co-assembly with other hydrophobic residues³⁷ can even further enhance the application areas such as producing hydrogels with tunable mechanical properties and creating structural diversity in self-assembly. In general, self-assembly of dipeptides is triggered by external stimuli such as pH changes,³⁸ ion addition,³⁹ temperature changes⁴⁰ or solvent mediation.⁴¹ However, temperature change, ion addition or solvent mediation could limit the usability of these systems for biomedical applications in terms of toxicity and limited range of temperature.

1.1.2.3 CO-ASSEMBLING PEPTIDES

Compared with those techniques, the co-assembly strategy provides to control of the spatial orientation of peptides in the assembled state and the morphology of the assemblies at neutral pH.⁴² Also, it does not involve any external stimuli to create nanomaterials.

The co-assembly strategy combines two or more peptide building blocks to form ordered structures, unlike peptide self-assembly which occurs within the same motif.⁵ There are three different co-assembly types: orthogonal (self-sorting), destructive and cooperative (Figure 1.5).

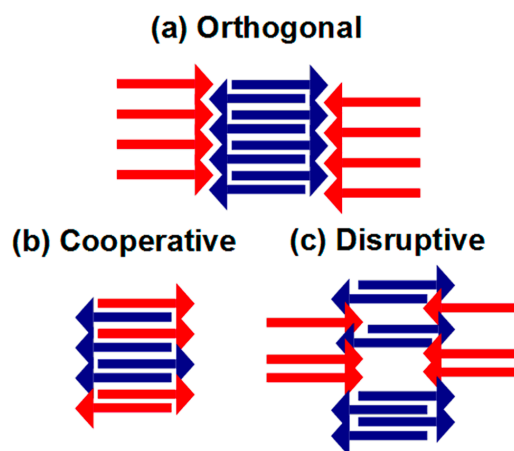


Figure 1. 5 A schematic shows three different co-assembly strategies. Individual components are assembled separately in the presence of one another during orthogonal (self-sorting) co-assembly (a). Building blocks in cooperative co-assembly are very similar to each other and interact with one another with donor and acceptor molecules in the sequence (b). Components in disruptive co-assembly incorporate partially and one of the components is disrupted by the other (c). Reproduced with the permission from ⁴³

In an orthogonal (self-sorted) co-assembly strategy, peptide building blocks are assembled independently while in the presence of each other. As a result, the rate of assembly of each component is likely different, and any variations in the assembly could be caused by the other component in the system, which can be seen in a mixture of Fmoc-FF and Fmoc-GG.⁴⁴ Therefore, designing and controlling orthogonally co-assembled systems is difficult because two components involve various non-covalent interactions.⁴⁵ Disruptive co-assembly is another type of co-assembly strategy in which one building block in the system serves as a barrier for the assembly; so that the physical properties of the resulting architectures can be easily controlled.⁴⁶ It was shown that integration of

FF peptides with Boc-FF (acts as a capping molecule) resulted in length control of nanotube formation.⁴⁶ In cooperative co-assembly, two peptide components interact with each other and architectures are created in which both parts are arranged alternately. This assembly typically used when individual components are very similar and have only minor differences. Employing electrostatic interaction is the most common way for the co-assembly process, which was designed by two complementary charge peptides.⁴⁵ Unlike other co-assembly strategies, cooperative co-assembly provides control of the assembly process by reducing the competition between self and co-association events due to the electrostatic repulsion of one component.³ For those reasons, our research focused on cooperative co-assembly for biomedical applications.

1.1.2.4 AMYLOID-LIKE PEPTIDES FOR BIOMEDICAL APPLICATIONS

One of the most promising applications of nanobiotechnology in healthcare is regenerative medicine. By enabling scaffolds functionalized with cells and biologically active molecules, bioinspired materials seek to mimic the extracellular matrix (ECM) to replace the degenerated tissues of the human body.⁴⁷ An ECM, a complex, three-dimensional (3D), fibrous, and hierarchically organized network that transmits various biochemical and physical signals, surrounds cells within tissues.⁴⁸ In addition, the ECM supports cells, regulates cell behavior, initiates cascades of intracellular signaling pathways, and controls soluble factors in and between cells.⁴⁹ Therefore, it is essential for regenerative medicine to mimic the same level of complexity and functionality of ECM with engineered biomaterials.⁵⁰

Development of amyloid-like peptide systems has attracted in the past years due to their ease of design, low cost, diverse functionalization options, and most importantly biocompatibility and biodegradability. Furthermore, having a short sequence (less than 8 amino acids) makes them non-immunogenic.⁶ A combination of two aromatic short peptide derivatives, Fmoc-FF, Fmoc-RGD (bioactive epitope), and Fmoc-RGE (non-bioactive epitope as a negative control) was used to create the hydrogel scaffold inspired by the ECM. Fibroblast encapsulated hydrogels support adhesion and cell spreading with the aid of RGD bioactive epitope.⁵¹ In addition to attaching bioactive ligands, FF-based hydrogels were also modified with the conductive polymer polyaniline (PAni).⁵² It was found that Fmoc-FF-PAni composite hydrogels were mechanically strong, conductive and showed self-healing properties. Also, they support cardiac cell growth with self-healing properties, allowing cardiac cells to endure the continuous contractions of the heart. Similar design approaches were conducted by using Fmoc-RGD with Fmoc-FF-PAni to enhance the application areas such as for DNA binding for rapid and effective detection of pathogens.⁵³ FF motif was also used by modifying with additional cationic peptides (R and K) to evaluate membrane-interacting and delivery capability.⁵⁴ The penetrating ability was performed with a model fluorophore carboxytetramethylrhodamine (TAMRA). R contained FF motif (RFFR) penetrated porcine skin and showed a potential transdermal penetration of small molecule drugs with RFFR peptide.

Overall, FF-based designs were used in different biomedical applications including tissue engineering and drug delivery. However, FF designs based on hydrogel applications have some limitations. First, since the main intermolecular interaction driving the assembly is $\pi-\pi$ stacking between the FF motif, hydrogels are formed in very concentrated forms and

thus, additional moieties such as Fmoc group would be necessary. Second, to prepare FF-based systems, organic solvents such as acetone or 1,1,1,3,3,3-hexafluoro-2-propanol (HFIP) are used for solubilization due to their highly hydrophobic nature. We consider both solubility and additional intermolecular interactions in our design to overcome these limitations. Furthermore, although general trends can be observed with respect to the hydrophobicity/aromaticity associated with the peptide sequence and the corresponding physical properties of the resultant systems; it is currently not possible to predict whether a given molecule will form a secondary structure or not reliably.

1.1.2.4.1 THE RELATIONSHIP BETWEEN AGGREGATION AND TOXICITY

The factors related to the mechanism of toxicity, the structure of amyloid fibrils and intermediate species are still open questions regarding amyloid fibril formation.⁵⁵ During the series of processes that transform monomers into mature fibrils, several important intermediates, including soluble oligomers and protofilaments, are populated.⁵⁶ Furthermore, aggregation is a complex process known to be influenced by several fundamental characteristics, such as secondary structure, hydrophobicity, and charge, as well as the composition and concentration of solutes in the surrounding environment. Therefore, understanding of this aggregation process, and kinetics of fibril formation is crucial because it is possible for soluble oligomers of amyloidogenic peptides to be even more toxic than the final amyloid fibril product.⁵⁷

A major finding causing the cytotoxicity of amyloid- β is cell membrane perturbations.⁵⁸⁻⁶² It was suggested that small size and hydrophobic surfaces of small intermediate molecules (such as oligomers) have a high affinity to biological membranes, and therefore

they are toxic.⁶³ The effect of hydrophobicity on cell cytotoxicity was further enhanced by systemically substituting hydrophobic core residues with polar amino acids.⁶⁴ It was found that if two-point mutations were introduced (F and I replaced by N), the assembly was suppressed from the early onset of aggregation and cell toxicity was reduced.

However, there are several challenges in understanding the leading cause of this toxicity. First, no probes can track the various protein aggregate types created or structures produced during this dynamic process.⁶⁵ Second, the variety of intermediate structures produced by different nucleation processes makes it more challenging to isolate and accurately predict the toxic agents causing amyloid disease.⁶⁶ Third, since the amyloid fibrillation process is concentration-dependent phenomenon, higher concentrations of amyloid peptides are needed to observe fibril formation in vitro within hours. Otherwise, to compare with physiological concentrations (at nanomolar level), several days and even months of incubation are needed to understand the process.⁶⁷

Hence, instead of using the whole sequence of amyloid peptide, amyloid mimicking peptides could be an alternative for understanding the amyloid aggregation and studying the intermolecular interactions with simplified models to find key residues that are responsible for toxicity. Although key residues in amyloid- β are defined as mentioned in the previous section, there is no or very limited research in the literature using those residues to correlate the toxicity and aggregation based on simplified models. Therefore, the abovementioned examples about aggregation and toxicity are mainly based on the change of amino acids in amyloid- β protein. Nevertheless, it is still helpful to understand the key findings related to toxicity and the aggregation process to create a peptide-based tool to study the aggregation process.

1.2 CHARACTERIZATION TECHNIQUES OF PEPTIDE ASSEMBLY

Different nanostructures can form with peptide assembly, which is crucial interest in biomaterials due to biocompatibility and other functionalities for biotechnological applications such as antimicrobial activities, tissue engineering, and drug and gene delivery.⁶⁸ As discussed, amino acids have a variety of physical properties such as polarity, charge, and hydrophobicity. Those characteristics give a unique feature to peptides in terms of secondary structures leading to different mechanical, chemical and physical properties.⁶⁹ Furthermore, environmental differences can also change those structures, including pH, temperature, and enzymatic reactions for desired applications. Therefore, it is essential to analyze the effect of intermolecular forces, which are part of the dynamic process of peptide assembly or aggregation process. In this part, the characterization techniques of peptide assembly will be discussed with recent studies.

1.2.1 SPECTROSCOPIC METHODS

Spectroscopic tools provide information at the global or atomic level based on the measuring the electromagnetic radiation (i.e., light) produced, absorbed, or scattered by matter. In peptide assembly, absorption spectroscopy techniques, which use electromagnetic spectra in which substance absorbs, are widely used to determine secondary structures such as infrared (IR), nuclear magnetic (NMR) spectroscopy and circular dichroism (CD).⁷⁰

IR results from energy absorption by vibrating chemical bonds in the molecule so that each bond can vibrate in different ways such as stretching or bending motions and absorb in different wavelengths.⁷¹ These vibrational modes, which intermolecular forces can

influence, can be quantitatively measured by Fourier transform IR (FTIR) spectroscopy in a non-destructive manner.⁷² In peptide self-assembly, amide I and II are major bands to analyze in the spectrum. The most sensitive region towards secondary structure is amide I (1600-1700 cm^{-1}) which results from C=O stretching in the amide group of peptide backbone.⁷³ Depending on the secondary structures: α -helical formation has strong amide I between 1650-1655 cm^{-1} while β -sheet show a strong band between 1612 and 1640 cm^{-1} .⁷⁴ Amide II is resulted from N-H bending and C-N stretching (strong band at 1540-1550 cm^{-1} and weaker shoulder at 1510-1525 cm^{-1}) and give information about parallel (1530-1550 cm^{-1}) or antiparallel (1510-1530 cm^{-1}) structures. The supramolecular assembly behavior of pentapeptide, KYFIL, was analyzed by changing specific amino acid residues to identify the intermolecular forces behind the self-assembly.⁷⁵ In FT-IR, self-assembly propensity was correlated based on β -sheet intensities (1700-1600 cm^{-1} region) and found that π -stacking and π -cation interactions with F play a major role in self-assembly. While KYAIL did not form any secondary structures, KYFIL showed the strongest and highest peak at β -sheet region.

NMR is another spectroscopic technique that uses the local magnetic properties around atomic nuclei to understand the molecule's structure in both solution and solid state.⁷⁶ It has been widely used to analyze peptide secondary structures and self-assembly mechanisms at the atomic level.⁷⁷ Since self-assembly is an equilibrium state in which both monomers and fibrils are at equilibrium, solution state NMR can be used to quantitatively compare the amount of non-assembled monomers and fibrils. Rajbhandary *et al.* analyzed the self-assembly of Fmoc-FF peptides with pH 10.5 (monomeric stage) and pH 7 (fibril stage) and determined the percentage of fibril assembly by analyzing

signal reduction.⁷⁸ Another study used solution state NMR to understand the effect of peptide concentration in self-assembly. For this purpose, IF dipeptide was used with a range of concentrations. As peptide concentration increases, the signals corresponding to aromatic protons become broadened, indicating a decrease in molecular motion due to the supramolecular organizations.⁷⁹ However, solution NMR can be limited in terms of spectra interpretation because molecular self-assembly causes frequency shifts, decrease intensity levels, and broadens the spectra.⁶⁹ Therefore, solid state NMR (ssNMR) is often the method of choice if there are close intermolecular contacts between amino acids (i.e. co-assembled peptide structures) with highly constrained molecular motions.⁷⁸ Jekhmane *et al.* discovered the design parameters in tissue scaffolds at the atomic level by using ssNMR to determine the effect of self-assembly degree and homogeneity in peptide functionalization.⁸⁰ They found that decreased levels of secondary structures and conformational heterogeneity in tissue scaffolds were correlated with less favorable platform stem cells. Another study analyzed the co-assembly strategy of oppositely charged peptides with NMR and simulation techniques to understand the time-based kinetics of peptide aggregation and organization of β -sheet-rich structures of peptides.⁸¹ It was found that Lys and Glu residues contribute to self-assembly with equimolar concentrations and encode molecular level of organization.

CD spectroscopy is another widely used technique to determine the secondary structures of peptides. The technique measures the actively chiral molecules based on the difference in absorbance of right and left circularly polarized light.⁸² For example, the optically active amino acids such as W, Y, F and C give spectra in the near-UV (320-250 nm). However, the far-UV CD spectra (260-180 nm) originate from absorbed light

resulting from peptide bonds (amide bonds) which give information about peptide secondary structure.⁸³ Although getting information about the physical interactions is limited when compared with NMR, it is useful in terms of analyzing a range of concentrations and environmental effects on peptide self-assembly in a short time and with a low sample volume.⁸⁴ The secondary structure transition from α -helix to β -sheets was shown with pyrene (aromatic motif) conjugated RMLRF and IQEVN.⁸⁵ While individual peptides showed α -helix in the solution (negative peaks at 202 and 228 nm), the mixture of two samples showed β -sheet like structure (positive peak at 202 nm and a negative peak at 220 nm), which highlights the importance of aromatic interactions to promote β -sheet structure. A similar secondary structure transition was also observed in amyloid-derived supramolecular structures with pyridine derivatives.⁸⁶ The transition from β -sheet to α -helix was obtained by changing the molar ratios of Fmoc protected FF (Fmoc-FF) peptide and 4,4-bipyridine (BPY). While β -sheet rich co-assembly was obtained with a 1:1 (Fmoc-FF:BPY) ratio at 192 (positive peak) and 216 nm (negative peak), α -helix transformation occurred with 2:1 (Fmoc-FF:BPY) ratio at 203 and 213 nm (two negative peaks) and twisted β -sheet was observed with 1:2 (Fmoc-FF:BPY) ratio at 196 nm (positive peak) and 226 nm (negative peak). The results demonstrated that stoichiometric change could be achieved by tuning the secondary structures and inhibiting intermolecular forces (hydrogen bonding and aromatic interactions).

1.3.1 FLUORESCENCE-BASED METHODS

The application of fluorescent dyes for high throughput screening studies (being able to measure in small volumes) is a common and suitable technique to understand peptide

self-assembly and aggregation behavior, including the kinetics.⁸⁷ Amyloid β -peptide aggregation is a highly studied biomolecule to understand the molecular mechanisms of self-assembly and at the basis of the building blocks for nanotechnological applications.⁸⁸ The aggregation mechanism is divided into three steps: i) lag phase in which peptides are mostly in monomeric form; ii) polymerization step where larger aggregates occur as a result of peptide monomer aggregation and iii) saturation where grown aggregates form nanostructures. In the case of peptide aggregation, interactions between fluorescent dyes and peptides can lead to a change in fluorescence emission which could be either a shift or an increase/decrease in maximum emission.⁸⁹ Thioflavin T (ThT, benzothiazole dye, is a widely used fluorescent probe to identify and analyze β -sheet rich structures such as amyloid peptides.⁹⁰ When ThT is introduced into a β -sheet rich environment, it results in enhanced fluorescence and shift in emission spectrum from 510 nm (unbound state) to 480 nm (bound state with peptide fibrils). With the ThT assay, the importance of the initial concentration of peptides (at monomeric state) for fibrillation was studied and minimum concentration was found to be as 0.2 mM.⁹¹ Time and concentration dependency were also analyzed with oppositely charged amyloid-like peptides and threshold concentration for the aggregation was visualized using confocal microscopy.⁹² Congo Red, azo dye, is another dye used mainly for histological analysis for amyloid detection that gives apple-green birefringence under polarized light.⁹³ In aqueous solution, it gives maximum absorption at 490 nm; however, a strong shift from 490 nm to 540 nm occurred when bound to β -sheet rich structures due to specific orientation.⁹⁴ Furthermore, it is also possible to stain peptide gel and acquire polarized images to imply the presence of β -sheet structures within the system.⁹⁵ Although Congo Red and ThT are widely used for

amyloid-like aggregation and be responsive to β -sheet structures, other fluorogenic dyes such as Nile Red and pyrene are primarily used in amphiphilic molecules to determine critical aggregation concentration (CAC) and be independent of β -sheet rich structures. Similar to Amyloid- β peptide aggregation, amphiphilic molecules can also undergo aggregation (generally results in fibrillar or micellar structures) when it reaches a specific concentration characterized by sharp transitions in fluorescence intensities.⁹⁶ Pyrene, composed of four fused benzene ring and insoluble in water, show distinct solvent-dependent vibronic bands depending on the local hydrophobicity or polarity of the environment.⁹⁷ The measurements are based on the third and first vibronic band intensities (I₃/I₁ or I₁/I₃) and are generally observed at between 375 and 405 nm when excited with 340 nm.⁹⁸ An increase in the ratio of I₃/I₁ gives an information about the hydrophobicity of the microenvironment where pyrene is located at.⁹⁹ Below the CAC, the decreased pyrene I₃/I₁ ratio value corresponds to a polar environment, whereas increased I₃/I₁ indicated that pyrene was located more in a hydrophobic environment.¹⁰⁰ Since aggregation behavior depends on environmental factors such as temperature, salt concentration and pH; pyrene assay can easily be applied to understand how those factors affect the given systems. For example, the aggregation behavior of two amphiphilic peptides (palmitic acid conjugated IKPEAP and IKPEAPGE) were analyzed based on temperature and pH and found that increase pH resulted in increase in CAC, while temperature (20 and 70°C) did not have effect on it.¹⁰¹ Nile red, a heterotetracyclic compound and known as lipophilic stain, also depends highly on the polarity of the medium.¹⁰² It was shown that the fluorescence emission of Nile Red at 587 nm was upregulated around 50 times when it was exposed to a hydrophobic environment.¹⁰³

Furthermore, assembly of oppositely charged peptide structures (which is driven by π -, hydrophobic and electrostatic interactions) was also determined by Nile Red (Ex: 550 nm, Em:580-750) assay and found that individual counterparts have 10 times higher CAC values than co-assembled peptide structures.¹⁰⁴ Fluorescent techniques give relevant information and help to analyze and determine/eliminate the conditions (with a range of parameters for further deep analysis of peptide self-assembly with other techniques (i.e. spectroscopic analysis)). However, different experimental techniques are required for the conformational transition of peptide assembly, such as the identifying folding/unfolding states to characterize the thermal energy produced or consumed as a natural consequence of almost all physical, chemical, or biological process.

CHAPTER 2. PEPTIDE FRAMEWORK FOR SCREENING THE EFFECT OF AMINO ACIDS ON ASSEMBLY

This section is adapted from the following publication:

Hamsici, S., White, A. D., & Acar, H. (2022). Peptide framework for screening the effect of amino acids on assembly. *Science advances*, 8(3), eabj0305.

Discovery of peptide domains with unique intermolecular interactions is essential for engineering peptide-based materials. Rather than attempt a brute-force approach, we instead identify a new strategy for discovery and study of intermolecular interactions; ``co-assembly of oppositely charged peptide" (CoOP), a framework that `encourages' peptide assembly by mixing two oppositely charged hexapeptides. We used an integrated computational and experimental approach; probed the free energy of association and probability of amino acid contacts during co-assembly with atomic-resolution simulations and correlated them to the physical properties of the aggregates. In this study, CoOP is introduced with three examples: Dialanine, ditryptophan, and diisoleucine. Our results indicated that the opposite charges initiate the assembly, and the subsequent stability is enhanced by the presence of an undisturbed hydrophobic core. We showed that the CoOP represents a unique, simple, and elegant framework, can be used to identify the structure - property relations of self-assembling peptide-based materials.

2.1 INTRODUCTION

Self-assembling small peptides are attractive building blocks because they are relatively easy to synthesize and enable systematic study using experimental and computational analyses to associate peptide sequence (structure) with its properties and functionality, making them promising candidates to fabricate functional nanomaterials.¹⁰⁵ In particular, self-assembly into fibrillar peptide aggregates is abundant in nature and various synthetic technologies in biomedical research^{106–113} and materials science.^{14,114,115} The organization of peptide assemblies emerges from small changes in the amino acid sequence that provides non-covalent interactions, such as electrostatic forces, hydrogen bonds, hydrophobic effects, and aromatic stacking.^{116,117} Understanding the effects of these small changes is essential to identify the structure - property relation and create small peptides that do not simply mimic natural sequences but instead are rationally designed for the desired properties. Studies based on editing the peptide sequences of natural designs typically have an initial focus on a particular type of interactions for the property of interest, which may restrict the achievable materials properties.³⁵ Screening all possible amino acids to create a wider range of properties, on the other hand, may encounter vast design spaces even for small peptides and is therefore impractical for full experimental exploration. Additional co-assembly strategies are beneficial as they can provide wider optimization of nanomaterials for various applications, but such approaches risk expanding the already vast design space.^{43,105} As a result, there is a need for an approach that can bridge the combinatorial explosion of amino acid sequence space with the benefits of editing known sequences to map and search new peptides for new functionalities.

Minimalist peptide designs that incorporate rational modification to produce robust structures have attracted significant interest over the past two decades.³⁵ Diphenylalanine (FF), a motif found in amyloid- β peptides, plays an important role in fiber formation via τ - τ stacking.¹⁷ Peptides with an FF motif have spurred the investigation of hierarchical structures and have been used in synthetic materials for various applications from biomedical research to energy harvesting and conversion.^{114,118} Consequently, identification of 1D assembly driven by FF domain has well-established tools that provide standardization and comparison of the results.¹¹⁹

Non-covalent interactions (ranging from 1 to 5 kcal/mol)¹²⁰ are naturally weak and may not be sufficient for stable and highly ordered assemblies of minimalist peptide designs. To alleviate the low thermodynamic advantage for assembled structures, proximity (high concentration) in solution is required (kinetic threshold). Addition of hydrophobic groups may provide proximity via spontaneous aggregation in water to assist in assembly, but this approach can reduce or eliminate entirely the solubility of minimalist peptides, which can drastically reduce the utility of any potential application in aqueous environments.³⁵ Therefore, a key challenge to the use of traditional minimalist peptides is to address the kinetic threshold for the aggregation.

Here, we overcome the kinetic threshold with enhanced solubility in a hexapeptide, by combining charged and hydrophobic amino acids in a new design of Co-assembling Oppositely Charged Peptides (CoOP). Because of the relatively small number of interacting groups in a hexapeptide, the kinetic threshold is high. The oppositely charged system addresses this weakness in typical small peptide systems; charges not only assist with aqueous solubility, but also provide a relatively long-ranged attractive force to

encourage peptides to come together. This effect is analogous to increasing the concentration of peptides without such charged groups.

In this paper, we introduce the CoOP strategy and explore the effects of alanine (A), tryptophan (W), and isoleucine (I) (we will use the standard single-letter amino-acid codes throughout) in this framework. We integrate computational methods to analyze, rather than to predict, the peptide assembly mechanism; atomic-resolution simulations are used to probe the free energy of association and probability of amino acid contact during co-assembly. The effects of the substitution domain on the aggregation kinetics are investigated via pyrene, Congo red staining, and dynamic light scattering. We use FTIR and circular dichroism to understand the secondary structures of peptides for understanding assembly mechanism and identify the physical properties of the emergent materials via TEM, AFM, and rheology. We combine the results to understand the relation of peptide sequence, association of intermolecular interactions on assembly kinetics, and structural and mechanical properties of the end products. Here, CoOP is shown to provide a valuable molecular discovery tool that is simple, water soluble, and assembles into 1D structure with quantifiable properties for exploring intermolecular interactions and harnessing the rules for peptide assembly phenomena.

2.2 RESULTS

2.2.1 CO-ASSEMBLED PEPTIDE DESIGN AND VALIDATION WITH MOLECULAR DYNAMICS

We have designed a remarkably simple framework composed of soluble hexapeptides that assemble into 1D structures upon mixing via co-assembly of opposite charged peptides (CoOP) (Fig. 2.1). Hexapeptides are composed of three domains; charged,

diphenylalanine (FF), and substitution domain [XX]. The sequences of the co-assembling hexapeptide system is given by Table 2.1, and chemical structures are in Fig. 2.1B. Framework sequence kept constant to enable the accurate assessment of the effects of inserting a specific two-amino-acid group into the substitution domain, [XX]. As shown in Fig. 2.1B, the partners of CoOP system have complementary charged amino acids on both ends of the peptides: KFFXXK sequence is the positive partner (pos) and EFFXXE is the negative partner (neg).

Table 2. 1 Sequences of the CoOPs used in this study. Each CoOPs has negatively and positively charged counterparts.

Nomenclature	(-) charged peptide	(+) charged peptide
[AA]	Ac-EFFAAE-Am	Ac-KFFAAK-Am
[WW]	Ac-EFFWWE-Am	Ac-KFFWWK-Am
[II]	Ac-EFFIIE-Am	Ac-KFFIIK-Am

Charged amino acids on the peptide termini induce the initial aggregation, followed by subsequent hierarchical assembly of 1D structure enables screening interactions of substitution domain and applying established methods to compare their effects on the properties of the resulted network. By introducing charged amino acids at both termini of the peptides, we increase solubility and allow the creation of “electrostatic mirror partners” (i.e., peptides with opposite net charge) that enhance aggregation by boosting initial peptide contacts.¹²¹ We select E and K to provide negative and positive charges, respectively. Our choice is informed by three key observations: first, salt bridges between K and E are known to enhance oligomer stability in amyloid- β peptides;¹²² second, the interaction of R with E is stronger than with K in a very specific direction, providing

molecular orientation of binding partners, whereas K salt bridges are effectively isotropic;¹²³ finally, the additional methylene group of R can contribute non-specific interactions such as H-bonding with the backbone of the partner peptide.^{124,125} Acetylation on N-termini and amide group on C-termini restricts charged interactions to only the amino acid side chains.

The substitution domain ([XX]) in the CoOP system in this paper is designed to be small but display measurable effects to demonstrate the capabilities of the strategy. We studied dialanine ([AA]), ditryptophan ([WW]), and diisoleucine ([II]), as shown in Fig. 2.1B, each having a different hydrophobicity index ($I > W > A$) due to the importance of this parameter for peptide aggregation.^{126,127} Hydrophobicity index is related to solvent accessible surface area (ASA), which defines as the exposed surface area of an amino acid to solvent.¹²⁸ A comparison of the substituted residues based on the ratio of hydrophobic and hydrophilic ASA (ASA ratio) is $I (3.9) > W (2.3) > A (1.5)$.¹²⁹ Furthermore, the β -sheet propensities of these amino acids that are calculated based on their frequencies of existence in a β -sheet region of analyzed proteins by Chau-Fassman follow a similar trend; $I(f:0.274) > W(f:0.203) > A(f:0.167)$.¹³⁰

The assembly pathway and peptide-peptide orientation are defined by the basic molecular framework of CoOP (i.e., the FF domain and terminal charges) while the intermolecular interactions provided by the substitution domain influence the assembly kinetics and mechanism, as well as the physical properties of the hierarchical assembly of the fibrillar structure and its resultant network. As a result, this CoOP system is designed as a tool to screen different canonical and non-canonical amino acids to identify

their effects on intermolecular interactions and to correlate them with the initial interactions and properties of the final hydrogel network.

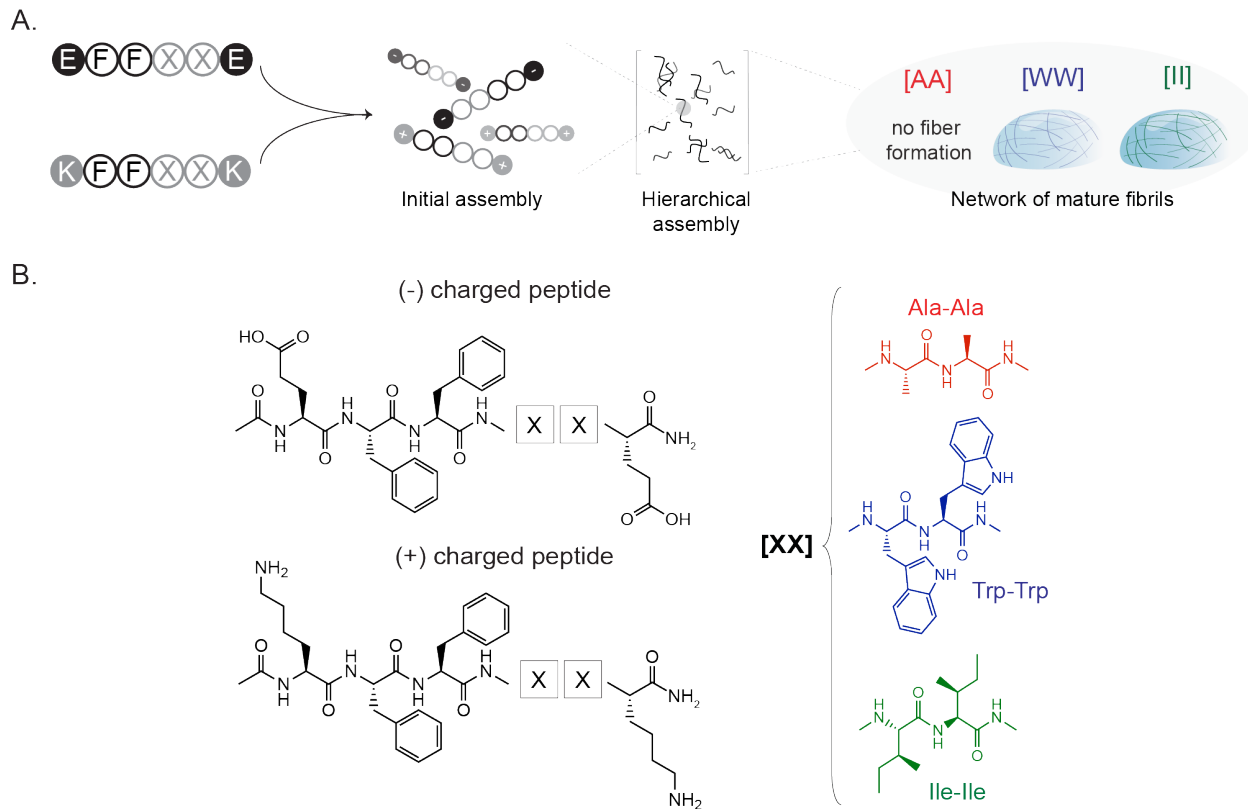


Figure 2. 1 CoOP design composed of oppositely charged hexapeptide units which represent the minimalistic assembly template. Schematic description of peptide co-assembly triggered by oppositely charged hexapeptides (A). Chemical representation of hexapeptides (B). E and K residues at both ends provided electrostatic interactions, FF at the core contributed self-assembly with π -stacking and replacing [XX] with either dialanine, ditryptophan or diisoleucine to enable tunable hydrophobic interactions.

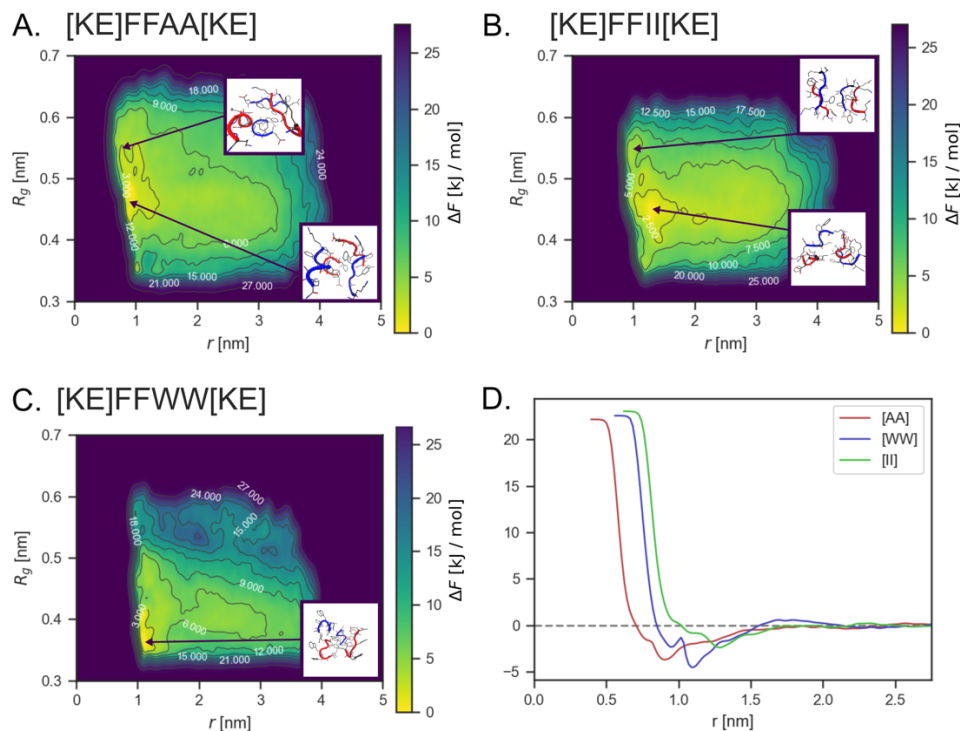


Figure 2. 2 Free energy surfaces of three co-assembly systems from a metadynamics calculation. r is average distance between all centers of mass and R_g is the average radii of gyration (both only consider backbone atoms). Panels A-C show free energy as computed via the metadynamics bias. Panel D shows the integrated free energy surface along the average distance. This plot does not predict the occurrence of self-assembly but is instead a measure of solvated peptide aggregation.

First, we validated the design via molecular dynamics simulations (MD). All-atom MD was used to access microscopic details that are otherwise difficult to attain in experimental techniques. Specifically, we sought information regarding the initial contact and interactions between amino acid side chains during assembly to assess our design rationale instead of prediction of entire process. We do not intend the molecular simulations to provide a fully predictive view of the entire process of assembly as the time and length-scales accessible to molecular simulations cannot adequately reproduce

experimental systems. Nonetheless, such techniques can help to examine reliability of our initial assumptions about the assembly process and measure free energies of pre-aggregated peptides.

Enhanced sampling or additional phenomenological modeling must be used to connect the relatively short timescales accessible using MD to the co-assembly experiments. For example, Amirkulava et al.¹³¹ relied on biasing methods to induce a small four peptide system to aggregate into structures consistent with experimental NMR measurements. Thurston et al.¹³² used Markov state models from all-atom simulations to model the self-assembly of a larger peptide system. Guo et al.¹³³ used enhanced sampling methods to understand the dimerization process that nucleates fibrilization in A β . Building on this past work, we use enhanced sampling of all-atom simulations to understand the free energy of contacts and initial aggregates of the co-assembly process. Then, we performed unbiased MD to understand the timescales of the peptide interactions. The minimum number of peptides to cover all possible co-assembly interactions is four, and so all MD contained four peptides (two positives, two negatives). To check if our conclusions hold to larger systems, we performed unbiased MD of the slowest co-assembling peptide system ([WW]) with 16 peptides for 392 ns (Fig 2.3).

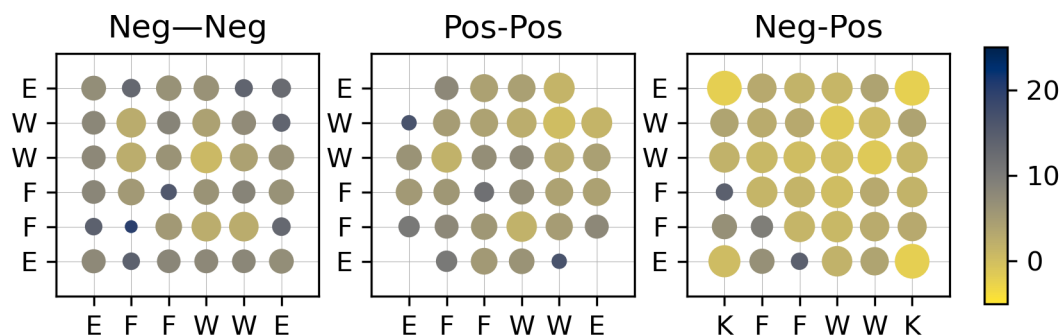


Figure 2. 3 Free energy of intra- and inter-chain contact between amino acids in the WW sequence. Contact is defined as there being a pair of two heavy atoms in an amino acid within 3.5 \AA . These are computed from a single 392 ns simulation via $F = -kT \ln P(c)$. No enhanced sampling was used, so should not be numerically comparable with main text due to inefficient sampling.

Free energy surfaces from 500 ns well-tempered metadynamics simulations of the four peptide co-assembling systems are shown in Fig. 2.4. The collective variables of these free energy surfaces are the average peptide-peptide distance and average intra-chain radius of gyration, which correspond to how close the peptides are and how compact they are, respectively. We observed that the order of distances among the pairs in their lowest energy levels Fig. 2.2D are correlated to the order of their ASA ratios and β -sheet propensity constants (Table 2.2) Hexapeptides with [AA] in the substitution domain showed a close-packed low free energy aggregate state with the least compact peptide structure among the pairs we studied ($R_g \sim 0.48 \text{ nm}$, Fig. 2.2A). The distance between [WW] was greater than that of [AA] in their lowest energy levels, but the [WW] showed the most compact structures ($R_g \sim 0.35 - 0.4 \text{ nm}$, Fig. 2.2B) and D). In [WW], we observed two distinct interactions in the lowest level; cation- π and π - π stacking, which leads to two separate local minima (Fig 2.2D). However, the CooP system with [II] in the substitution domain showed the greatest separation between peptides in their lowest energy levels,

while the side chains were packed closer (as indicated by $R_g \sim 0.43$ nm, see Fig. 2.2B and D).

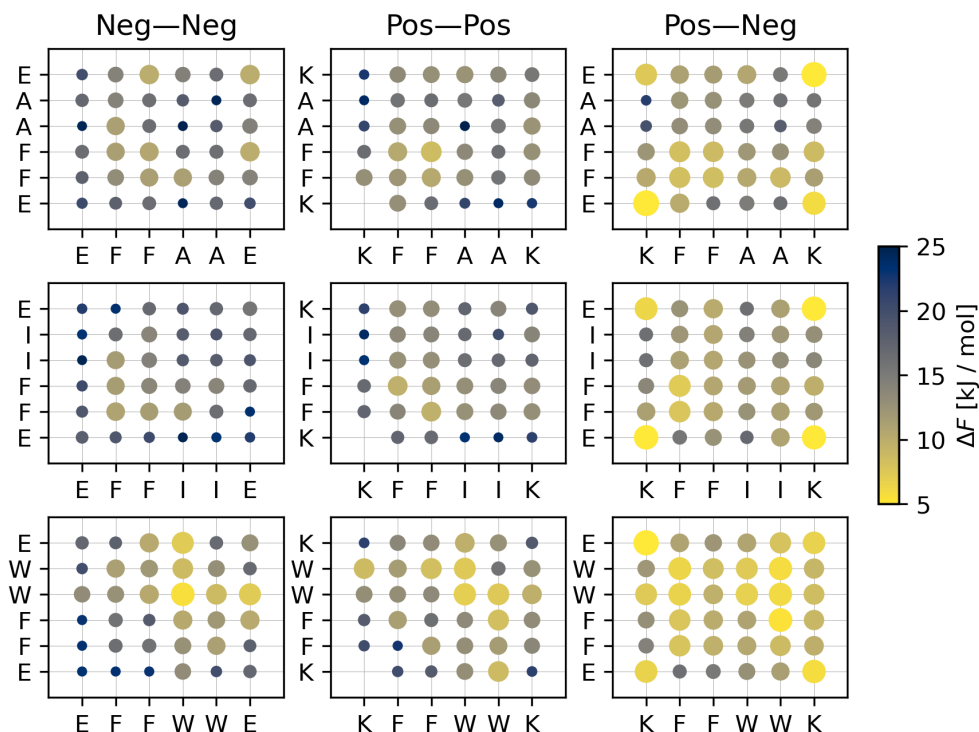


Figure 2. 4 Free energy of intra- and inter-chain contact between amino acids. Contact is defined as there is a pair of two side-chain heavy atoms in an amino acid within 3.5 \AA . These are computed via reweighting the metadynamics simulations. (Bigger size of circles and lighter color defines lower free energy, higher probability of contact).

Fig 2.4 shows the free energy of side-chain contact for peptide pairs between hexapeptides of both same and opposite charges (with contacts defined as a distance $\leq 3.5 \text{ \AA}$). The reference state for these free energies is unbound, resulting in all positive free energies because there is not a single favored conformation for the hexapeptide

aggregates. Peptide aggregation is still favored, as seen from Fig. 2.2D, but no single side-chain contact is found in all aggregate conformations.

Table 2. 2 Physical properties of CoOPs. The overall characterization of substitution domains and CAC of CoOP pairs. N/A: not available, Pho: hydrophobic, and Phi: hydrophilic

Substitution domain	Total ASA	Pho ASA	Phi ASA	Ratio (Pho/Phi)	Side-chain pho index	CAC (μM)	β -sheet frequency
A-A	111	66	45	1.5	41	N/A	0.167
W-W	249	174	76	2.3	97	79.4	0.203
I-I	173	137	35	3.9	99	24.5	0.274

The formation of salt bridges in [AA] is indicated by the favorable free energy for interactions of opposite charges (Fig. 2.4). Moreover, π - π stacking between F-F also appears to form. However, the hydrophobic core in the region between interacting hexapeptides did not form because of lack of A-A side chain interactions. The A-A interactions are significantly weaker than the I-I ($p < 10^{-5}$) and W-W interactions ($p < 10^{-10}$) showing indeed that the A-A side-chain interactions contribute little to forming an aggregate hydrophobic core. Additionally, as shown in Table 2.2, the order of β -sheet propensity of these amino acids has a similar trend, which might be decisive in the ordered assembly process after initial aggregation. The [AA] system thus serves as a good control sequence, showing the role of the salt bridge and F-F interactions alone.

Unlike [II], [WW] has relatively favorable neg-neg and pos-pos interactions that are dominated by the interactions of W side chains. The pos-neg interactions involve salt bridges, cation- π , and aromatic W-F interactions. It is important to note that the charged

side-chains are also interacting with the core region of the [WW] in all alignments, disrupting the core hydrophobicity; for example, K forms interactions with aromatic groups (Fig. 2D). The [WW] contact map is qualitatively consistent with the 16-chain system, validating the assumption that the enhanced sampling on four chains is a reasonable approximation for larger systems. To understand the probability of first contacting residues in peptide chains, we ran 40 unbiased MD simulations to assess assembly kinetics, with each simulation terminating once all four chains were aggregating. Fig. 2.5 shows the first contact(s) recorded for simulations that resulted in four chains aggregating. These are sampled at a time resolution of 2 picoseconds.

Overall, the [II] and [AA] systems seem to start aggregation frequently with salt bridging. We found the W side chain to be a promiscuous group in the [WW] system, interacting with all residues in the first contacts. These results show that aggregation typically proceeds from pos-neg contact, and this contact can nucleate stable assemblies via either hydrophobic interactions or salt bridging. Such heterogeneous interactions create heterogeneous hierarchical assemblies, and so, fibrillar structures, as can be seen in TEM of [WW]. Fig. 2.6 shows the secondary structure of the three systems at initial contact and gives additional evidence of the heterogeneous nature of the [WW] system. Specifically, the negative chains are helical and the positive chains β -sheet like.

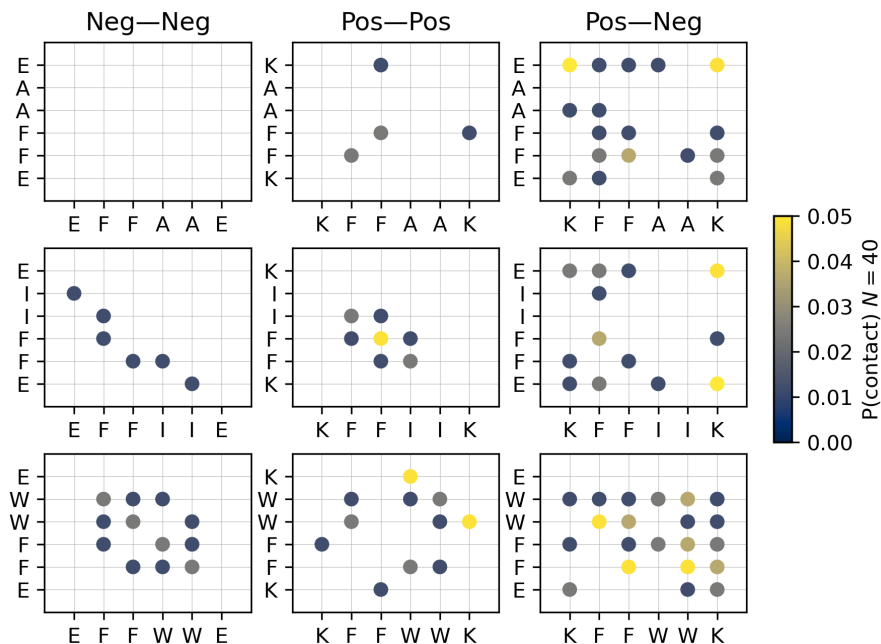


Figure 2. 5 Probability of first contacting residues from 40 unbiased molecular dynamics simulations. Contact is defined as there being a pair of two side-chain heavy atoms in an amino acids within 3.5 \AA . Simulations ended at a four-chain aggregate and began with the chains at least 2.5 nm apart. Working from end, this plot shows the minimum non-zero contact maps averaged across the 40 simulations. (Lighter color represent more contact).

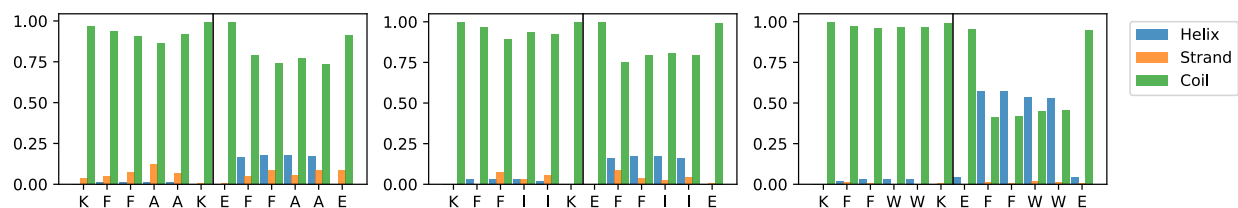


Figure 2. 6 Secondary structure of peptides at initial contact. Coil is random coil, Strand includes beta-sheet forming dihedral angles. Reweighted as described in maintext.

Perhaps the closest co-assembly modeling work to that described here is the coarse-grained molecular dynamics simulations of conjugate acid/base co-assembly of CATCH peptides.¹³⁴ Shao et al. studied a much larger system and found that co-assembly allows pos-pos and neg-neg pairs as fibers assemble. Regarding the amino acid interactions that drive co-assembly, Frederix et al.³⁵ surveyed coarse grained models of tripeptides

and found the FF motif was a consistently strong influence, as expected from its role in Amyloid β formation.^{30,135} The same group also showed that K can be a good choice for a positive amino acid in electrostatically-influenced assembly because of its stronger cation- π interactions relative to R.

2.2.2 CO-ASSEMBLED PEPTIDE CHARACTERIZATION

Upon validation of the design rationale of the CoOP system, we characterized the assembly kinetics and mechanism of the studied pairs experimentally; these aspects are dependent on the substitution domain.

2.2.2.1 CO-ASSEMBLY OF PEPTIDES INTO 1D STRUCTURES

The CoOP framework is designed to form 1D aggregations. At pH 7 all peptides were soluble in water and displayed the expected charges (pKa of (-COO⁻) of E is 4.25 and (-NH⁺ of K is 10.53). When mixed with equal concentrations and volume, the total charge of the aggregate becomes neutral (Fig. 2.7). Upon simple mixing at room temperature by pipetting, [WW] and [II] rapidly assembled into 1D structures at a monomer concentration of 10mM (Fig, 2.8A) (weight% [AA]= 0.75w%, [WW]= 0.9w%, and [II]= 0.8w%) without temperature increase, sonication and pH adjustment. The diameter of the formed 1D nanostructures was measured at around 5-10 nm for [II] and [WW] (Fig. 2.8 and 2.9B). However, for the [AA] (featuring the narrowest hydrophobic ASA and the lowest β -sheet frequency) no organized structure formed at a concentration of 0.75 w/v% which is lower than previously studied (2w/v %).¹³⁶ These results indicate CoOP meets the three goals of our design rationale: a simple, water soluble hexapeptide system that assembles into 1D structures when mixed.

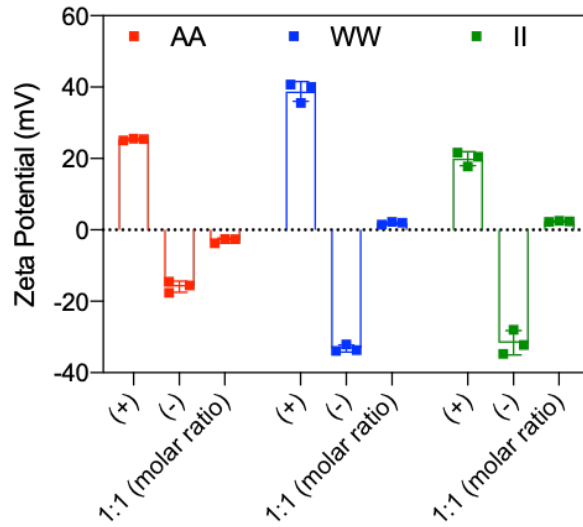


Figure 2. 7 Zeta potential measurements. Individual positively and negatively charged peptides and 1:1 (molar ratio) mixed forms.

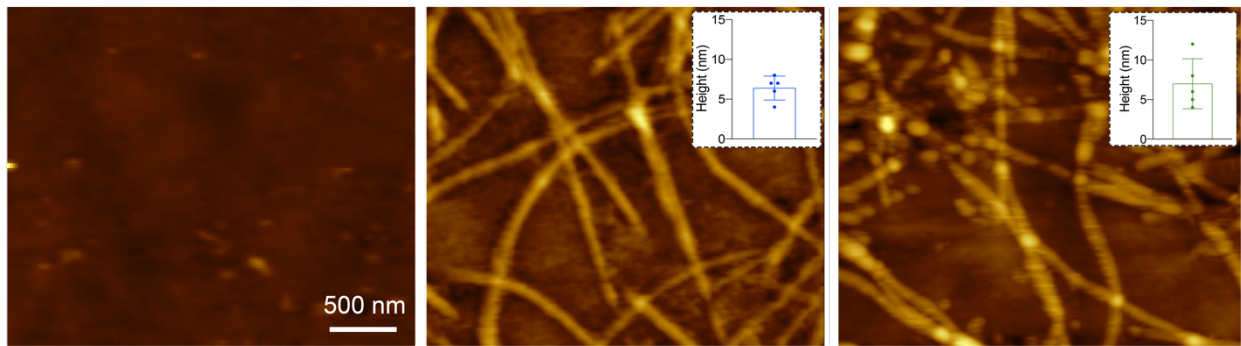


Figure 2. 8 Morphological analysis of peptide structures. AFM images of CoOPs. Diameter analysis of [AA], [WW] and [II].

2.2.2.2 CHARACTERIZATION OF ASSEMBLY KINETICS AND MECHANISM

The FF domain of the CoOP system provides an amyloid-like 1D assembly that has well-established fluorescent-based analyses methods to compare the assembly kinetics of the system, which is dependent on the substitution domain.

Critical aggregation concentration (CAC, the minimal concentration required for the onset of aggregation) was analyzed using the hydrophobic probe pyrene (solubility in water: 2-3 μM). Pyrene preferentially aggregates in the interior hydrophobic regions of the assembled structures.¹³⁷ An increase in the ratio of fluorescence intensities of the third and first vibronic peaks of pyrene, I_3/I_1 , reveals the hydrophobicity of the local environment; the increased polarity of the local environment reduces the I_3/I_1 ratio. At the CAC, pyrene moves into the hydrophobic inner core and sequesters within the FF domain with a requisite increase in I_3/I_1 ratio.¹³⁸ Pyrene assay for our CoOP system showed an increase of I_3/I_1 fluorescent intensity ratio for [II] and [WW], indicating 1D structure formation, while no increase for [AA] indicates no assembly at this concentration. Measured I_3/I_1 values were plotted against log values of CoOP monomer concentrations and sigmoidal hyperbola of the graphs indicates CAC values for [II] and [WW] as 24.50 μM (0.002 %w) and 79.4 μM (0.007 %w), respectively (Fig. 2.9C).

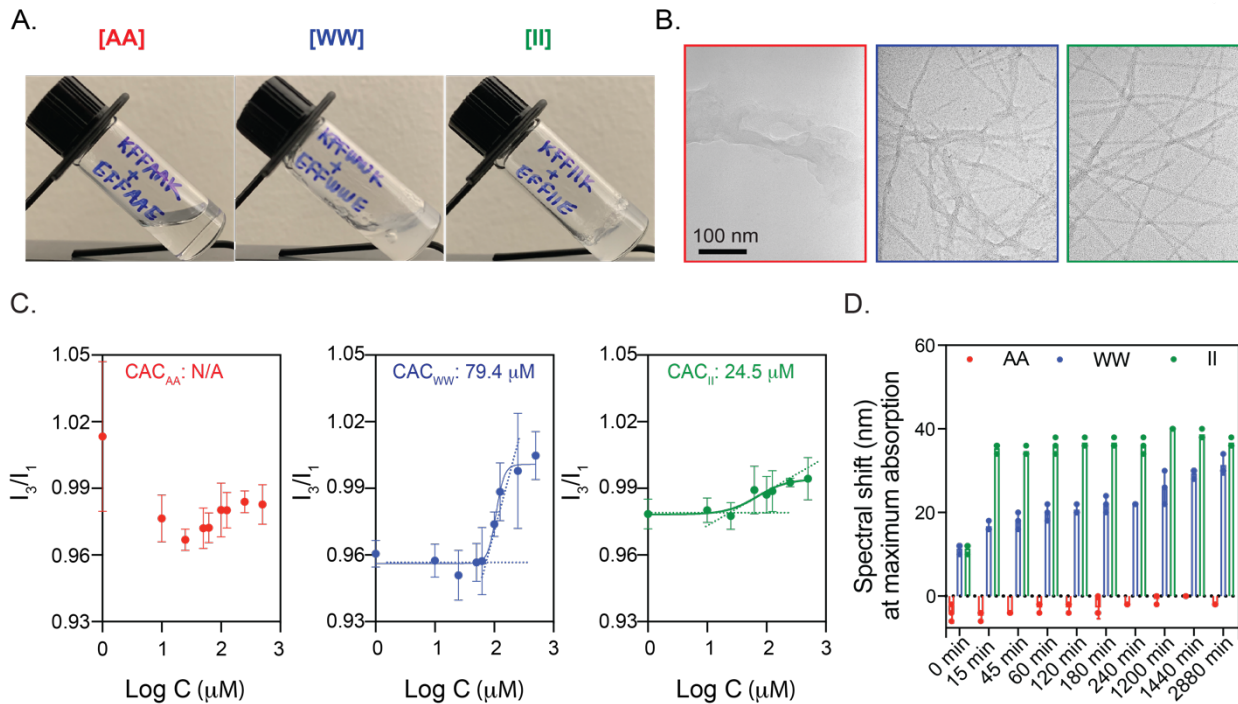


Figure 2.9 Hydrogel formation and 1D nanofibrillar assembly kinetics. Upon mixing two oppositely charged peptides, [II] and [WW] formed gels (A) consisting of nanofibers (B) while [AA] did not form any organized structure (A,B). Molecular co-assembly of the peptides was characterized by CAC determination (C). Characterization of amyloid-like aggregation mechanism probed by congo red assay for two days (D)

Congo red is an azo dye with a phenyl group, used for characterization of amyloid-like fibrillar assembly which requires specific orientations of FF domain derived β -sheet rich structures.⁹⁴ Congo red molecules participate in the fiber assembly process via H-bonding and π -stacking.¹³⁹ Such arrangement in the fibril assembly causes red shift in Congo red absorption from 498 nm. We observed a red shift in our Congo red analyses for [II] and [WW] (from 498 nm to 540 nm), but no change was observed for [AA] (Fig. 2.9D). The red shift for [II] was observed ~ 15 min after mixing and remained constant for 48 h. By contrast, the red shift of [WW] appeared 20 h after incubation. This indicates that hierarchical assembly into fibrillar structure continues after the initial interactions.

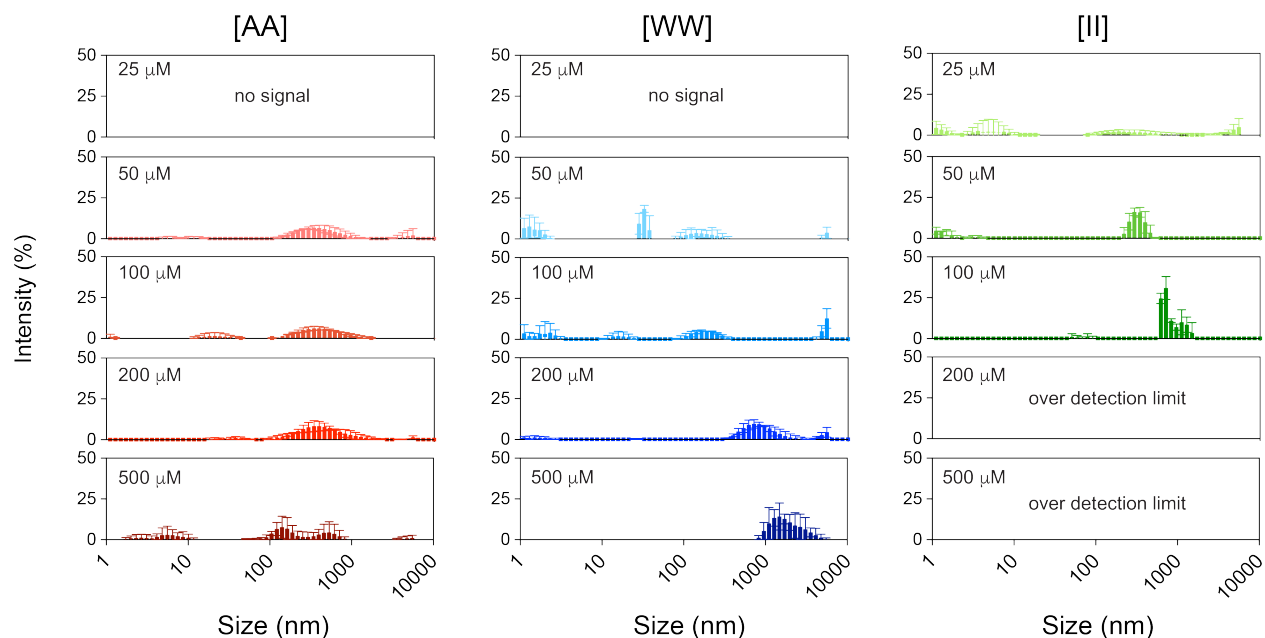


Figure 2. 10 Determination of aggregation concentration of CoOPs. Dynamic light scattering (DLS) measurements were performed by co-assembled peptides with immediate incubation.

Furthermore, dynamic light scattering (DLS) was performed for identification of the concentration when aggregates started to form, instead of measuring the size of the aggregates. When mixed, [AA] and [WW] did not show any aggregates at 25 μM , while the signals of scattered light was observed in [II] in this concentration, which is correlated to the measured CAC of [II], 24.5 μM . The intensity of the scattered light and corresponding aggregate sizes did not increase with increasing concentration of [AA] as expected, because no aggregation is observed for [AA] in these concentrations. [WW] system aggregations showed similar results after 50 μM , due to CAC of [WW] being measured as 79.4 μM . The intensity of the scattered light and its corresponding sizes increased with increasing concentrations for [WW], but no saturation is observed. The intensity of the scattered light increased for larger aggregate sizes for [II] with increasing

concentration, and over saturated above 200 μM (i.e., beyond the measurement limits)
 (Fig. 2.10)

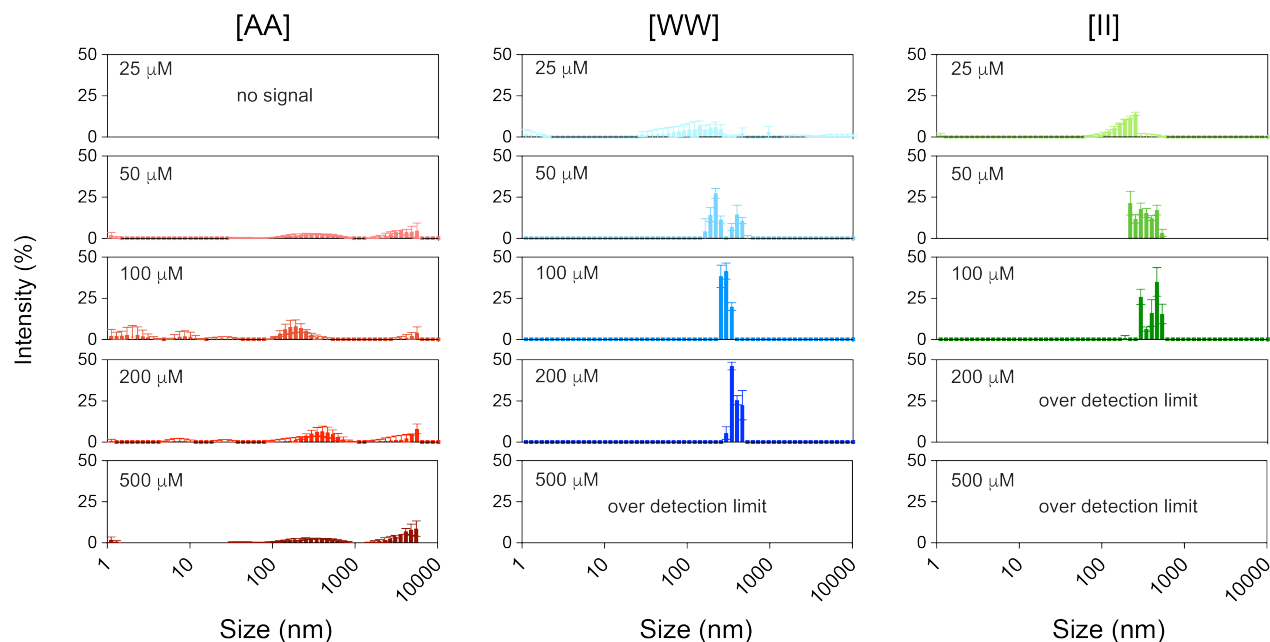


Figure 2. 11 DLS measurements of CoOPs. DLS measurements were performed by co-assembled peptides with overnight incubation.

When the system was incubated overnight, the maturation of the fibrillar structures into network formations was enhanced, and likewise the intensity of the scattered light in DLS (Fig 2.11). The aggregates become larger for [AA] after 200 μM , which might indicate some network formation. Similarly [WW] formed larger aggregates, likely with more uniform size as the intensity of the light increased in a small range of sizes and oversaturated at 500 μM . The saturation concentration is observed at 200 μM for overnight incubated [II] and the intensity of the scattered light increased in a smaller range for low concentrations.

As expected, the individual peptides alone did not show a significant aggregation at 500 μM , even after overnight incubation (Fig. 2.12). A slight intensity and size changes were

observed especially for positively charged groups, in agreement with MD simulation results that indicate the probability of contact points of positively charged peptides were higher than their negatively charged counterparts; however, the intensities were still insufficient to observe a trend with pyrene measurements, and thus the CAC could not be quantified.

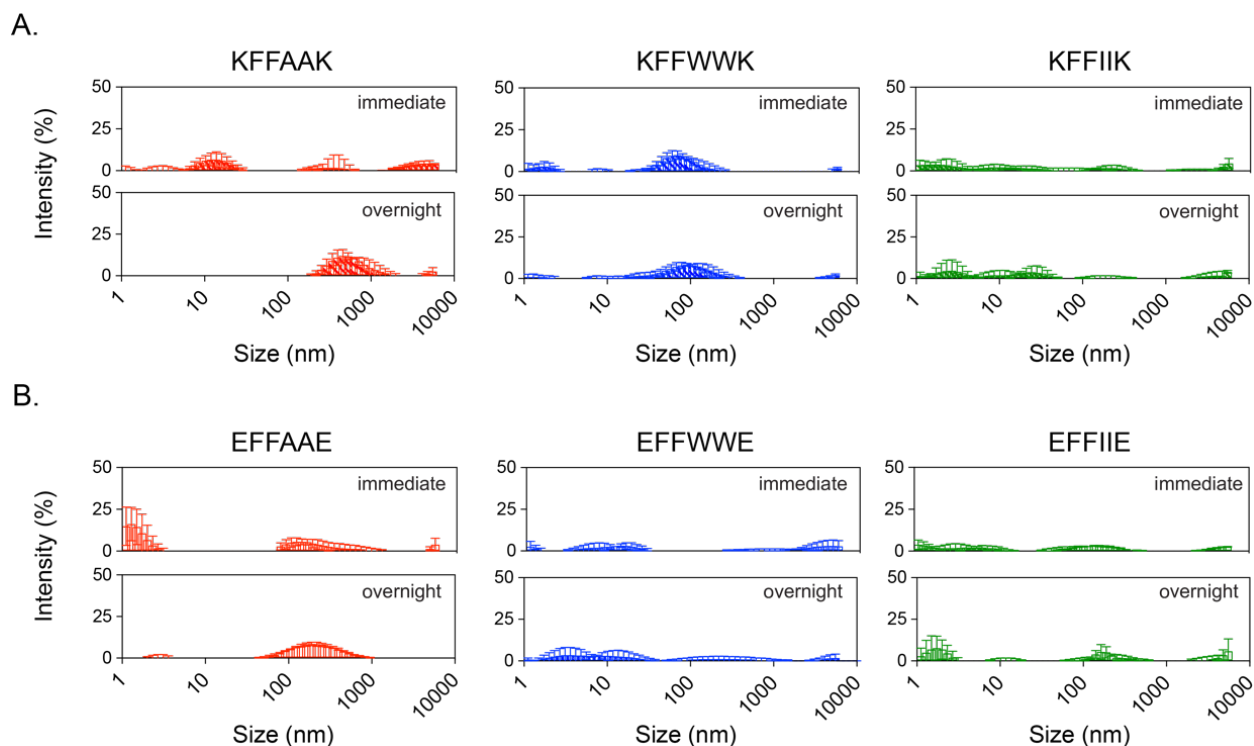


Figure 2. 12 DLS measurements of single peptides. DLS measurements were performed with freshly prepared and overnight incubated samples for both positively (A) and negatively (B) charged peptides at 500 μ M.

2.2.2.3 SECONDARY STRUCTURE ANALYSIS OF 1D STRUCTURES

Directed assembly of CoOP provides analyses of the effect of the substitution domain on the assembly mechanism. Upon initial aggregation, conformational changes of the amino acids side chains create the secondary structures and maturation of the fibrillar

assemblies. We analyzed the secondary structures of these systems with FTIR spectroscopy and circular dichroism (CD) under different concentrations.

Amide I and II are two major bands of FTIR analysis for peptide aggregations as they indicate the conformation of individual peptides. The most sensitive region with regards to a secondary structure is amide I (1600-1700 cm^{-1} as a result of carbonyl ($-\text{C}=\text{O}$) stretching of peptide bonds in backbone.¹⁴⁰ Strong amide I absorption between 1650-1655 cm^{-1} is attributed to α -helical structures, while β -sheet structures show a strong absorption band between 1612 and 1640 cm^{-1} .¹⁴¹ Amide II results from ($-\text{N}-\text{H}$) bending and ($-\text{C}-\text{N}-$) stretching (strong band at 1540-1550 cm^{-1} with a weaker shoulder at 1510-1525 cm^{-1}). FTIR spectrum of [AA] pairs showed a similar trend as in the pyrene and Congo red assays, with no apparent organized assembly at this concentration. The observed broad peak at 1647 cm^{-1} at different [AA] pair concentrations indicate random coil or disorganized structure (Fig. 2.13A). The positive and negative counterparts of [AA] pairs also showed a similar trend (Fig. 2.14) The intensity of the Amide I region at 1625 cm^{-1} was observed in [WW] pairs, but this signal was weaker compared to [II] pairs (Fig. 2.13A, blue). No Amide I peak is observed at 50 μM [WW], which is below the CAC (79.4 μM).

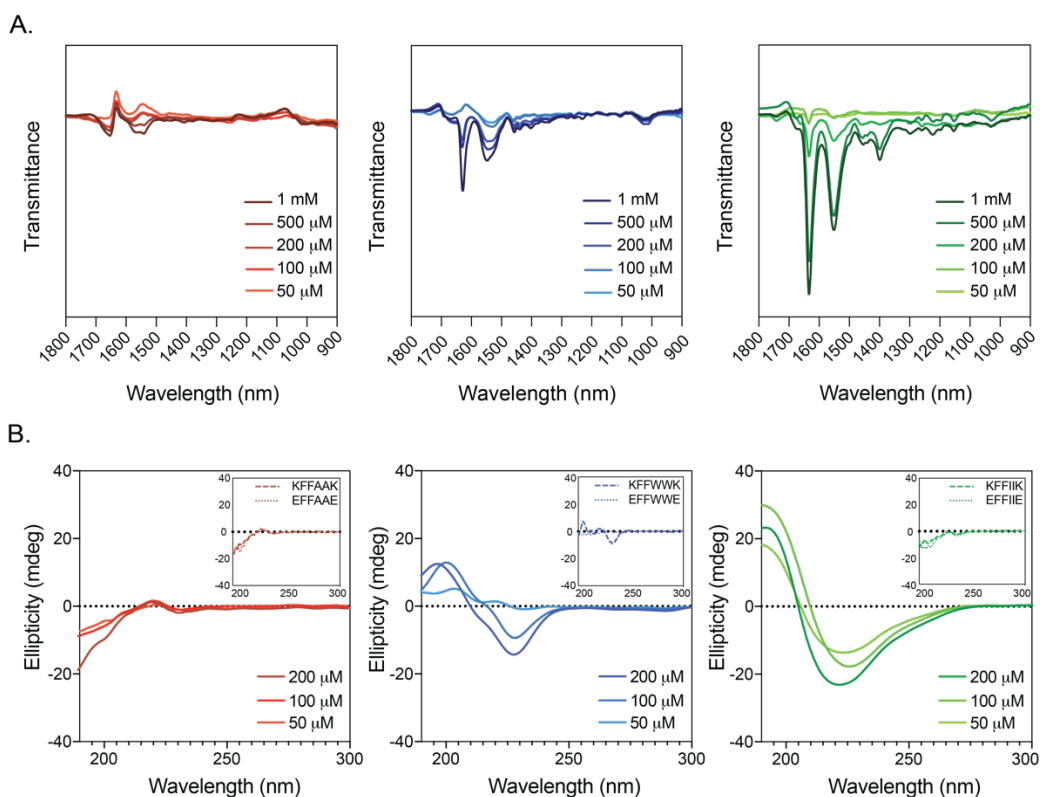


Figure 2.13 Structural determination of CoOPs. Secondary structure analysis of CoOPs and the individual counterparts in water with different concentrations by using FTIR and CD measurements (A,B)

The strong band for Amide I regions (at 1627 cm^{-1}) of [II] pair FTIR spectrum corresponds to highly ordered peptide assembly (Fig. 2.13A, green). The next band, occurring at 1545 cm^{-1} , corresponds to Amide II regions (N–H bending and C–N stretching, $1450\text{--}1550\text{ cm}^{-1}$) which are hardly affected by side-chain vibrations.¹⁴² While 1 mM [II] showed the strongest intensity in Amide I and II regions, the peaks were observable even at $50\text{ }\mu\text{M}$ (CAC [II] is $24.50\text{ }\mu\text{M}$), indicating that β -sheet structures form at these low concentrations. In addition, individual counterparts of [II] (KFFIIK and EFFIIE) did not show peaks for any concentration studied, even at 1 mM concentration (Fig 2.14). This suggests that the highly hydrophobic core of this peptide sequence was insufficient to initiate aggregation.

Circular Dichroism (CD) provides information regarding the secondary structure of the peptide aggregates. CD spectra for different concentrations of [AA] showed negative peaks at 190-200 nm and weak broad shoulders around 217-220 nm, which typically indicates unordered or random coil peptide structures (Fig 2.13B), red).¹⁴³ Individual members of [AA] pairs also showed the same trend, indicating no observable ordered structure for these peptides.

Peptides with β -sheet conformation typically show broad positive and negative peaks at 195 and around 216-218 nm, respectively.¹⁰⁵ [WW] showed a red-shift compared to standard β -sheet peaks; a negative peak at 228 nm and a positive peak at 197 nm were observed for 200 μ M concentration, with further red-shift observed towards 204 nm as concentration decreases. The resultant shift in CD spectra corresponds to twisted and distorted arrangements, which are known to weaken the intermolecular forces because of increased distances for H-bonding.¹⁴⁴ The observation of weakened structure in CD for [WW] is correlated to their FTIR results. The individual members of the [WW] pair showed opposite trends; while EFFWWE did not show any peak related to structured organization, KFFWWK showed similar two peaks at 195 (maximum) and 226 nm (minimum) as in the [WW] pair. The stacking of KFFWWK was also shown by side chains residues with a high probability of contact in Fig. 2.4. The stacking of aromatic rings of W shows a negative CD band around 227 nm.¹⁴⁵ Among the CoOPs in this study, [II] showed the highest positive and negative peaks at 192 and 214 nm with a slight blue shift (2 nm), with all concentrations indicating β -sheet rich structure (Fig. 2.13B, green).¹⁰⁵ As the peptide concentration decreased, slight intensity differences and red shift were observed, indicating the expected weakening of β -sheet content with decreasing concentration.¹⁴⁶

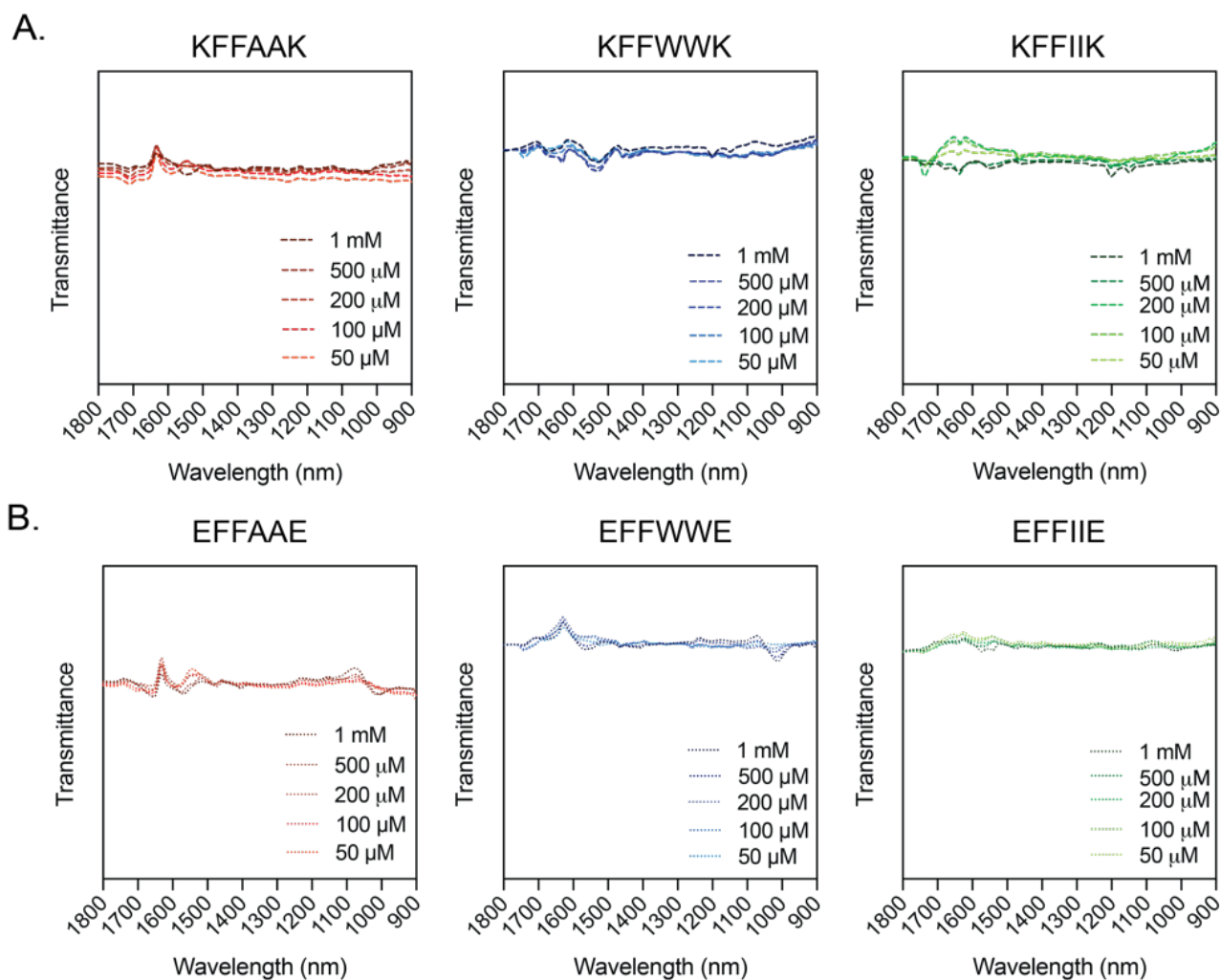


Figure 2. 14 Secondary structure analysis CoOPs. Positively (A) and negatively charged (B) individual peptides in water by using FTIR.

2.2.3 MECHANICAL PROPERTIES OF CO-ASSEMBLED PEPTIDES

The network of 1D structures of CoOP assemblies encapsulate solvent and forms hydrogel at the macro level. The time-dependent mechanical properties of the hydrogels can be correlated to the assembly kinetics and mechanism for each substitution domain. Small amplitude oscillatory shear (SAOS) rheology measurements enable identification the shear storage modulus (G'), loss modulus (G'') and loss factor ($\tan \delta$), which are all critical hydrogel properties monitored as a function of time, frequency, and applied strain.

Peptide-based hydrogels show viscoelastic behaviors. Therefore, we initially identified the linear viscoelastic regime (LVR) for all CoOPs (all 10 mM in water), where the moduli are independent of applied shear strain.

We identified the LVR through a strain sweep for two different time points after mixing the oppositely charged peptides: immediate (Fig. 2.15) and overnight (20h) (Fig. 2.16) incubation.

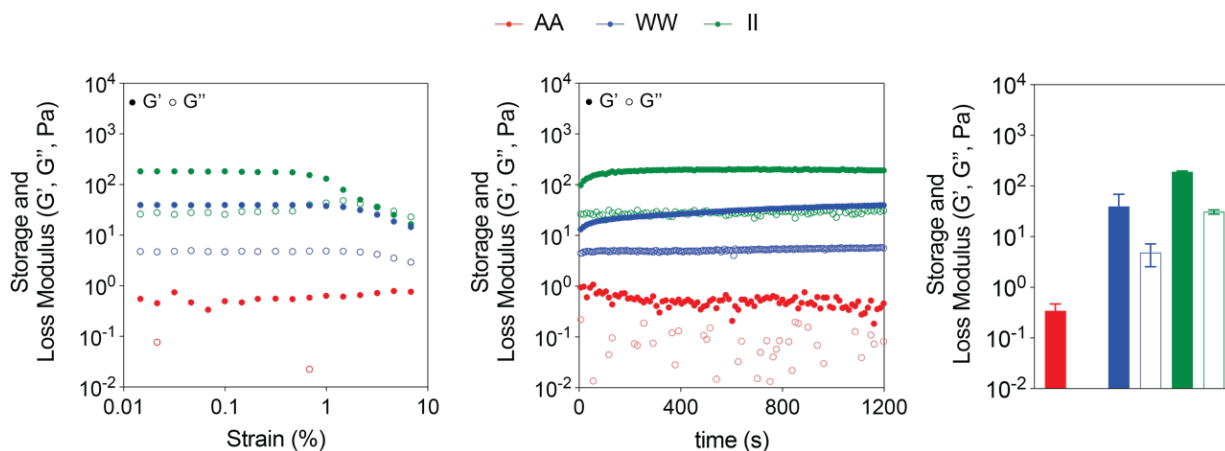


Figure 2. 15 Mechanical characterization of CoOPs. **Time sweep and strain sweep tests of [AA], [WW] and [II] for immediate analysis.**

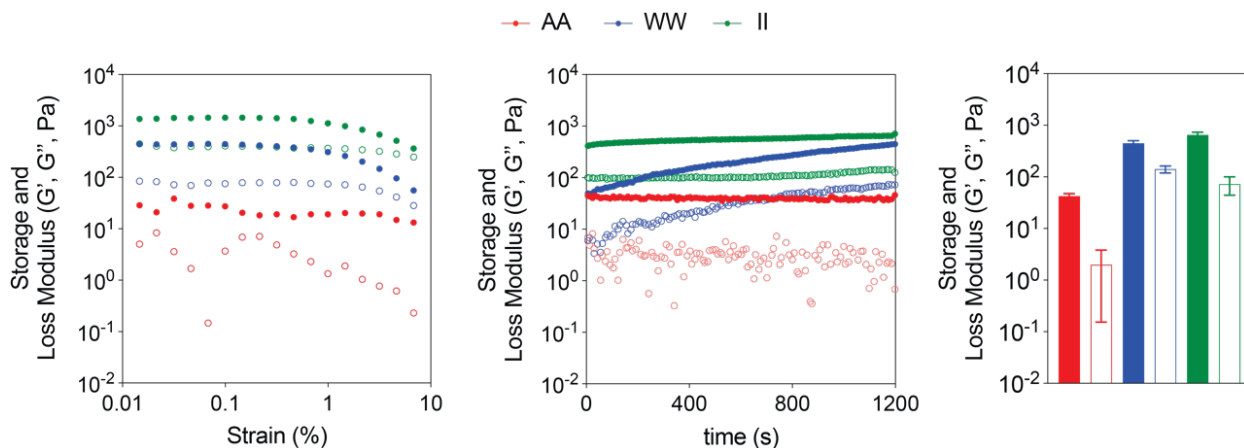


Figure 2. 16 Mechanical characterization of CoOPs. Time sweep and strain sweep tests of [AA], [WW] and [II] for overnight characterization.

For [II] and [WW], LVR was observed at up to 1% strain, the hydrogel responses (G' and G'') showed independent magnitudes to the changing strain; hydrogel structure maintained intact.

After finding the linear region, time sweep scans were performed at 0.1% strain for 20 min, again at immediate and overnight (20h) incubation. All peptide groups except [AA] achieved linear regime and showed hydrogel properties ($G' > G''$) in 20 min (Fig. 2.15). We then analyzed the gelation time where G' and G'' begin to show linear values as strain is applied in the LVR. Upon mixing negative and positive counterparts of the CoOP pairs, an immediate increase in G' for [WW] and [II] was observed. We calculated the gelation time by non-linear fitting of G' data to one-phase association as shown in Fig. 2.16. [II] plateaued only 12 min after mixing according to the fitted data, while [WW] did not plateau during the time of the measurement. The gelation time of [II] is correlated to the kinetics information gathered from Congo red assay, where [II] showed the appropriate intensity in 15 min. [WW] showed continuous assembly over 24h in Congo red, also indicated by rheology as G' did not plateau in 20 min. $G'[\text{II}]$ was estimated as 192 ± 7.3 Pa, nearly three times higher than [WW] (44.5 ± 22) in measurements performed immediately upon mixing, and also showed faster gelation. These results indicate stronger and faster aggregation, in agreement with the previous characterization of these systems.

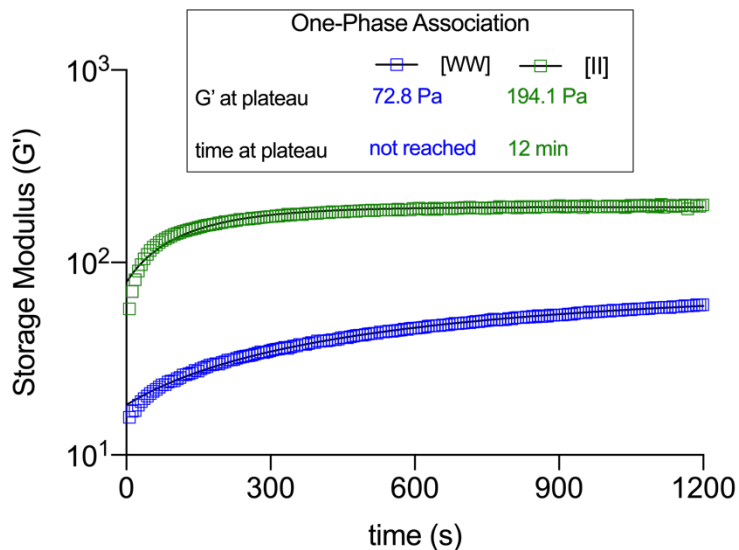


Figure 2. 17 Storage modulus of [WW] and [II]. One phase association of storage modulus of [WW] and [II] during 20 min.

Mechanical properties and time sweep analysis showed that while [II] showed the fastest and strongest gelation behavior, [AA] was found to be the slowest and weakest. These results were also correlated with a Congo Red assay, which showed no assembly for [AA], ongoing assembly for [WW] and immediate assembly for [II].

Co-assembly was still ongoing for at least [WW], and thus we measured the mechanical properties of the CoOPs after incubation at room temperature for an overnight interval (20 h, Fig. 2.16). The strain sweep analyses showed no significant change after overnight incubation for assembly of [II] and [WW]. The increased G' value of [AA] indicates some degree of the assembly after 20 h of incubation. The time sweep measurements revealed more significant differences of G' and G'' values for all the CoOPs at 0.1% strain. G' of [II] increased approximately 3.5X (from 192 ± 7.3 Pa to 675 ± 55 Pa), indicating a higher degree of assembly after 20 h. The values for [WW] were more than 8X (from 44.5 ± 22 Pa to 453 ± 47.5 Pa). Moreover, [AA] also showed hydrogel properties after overnight assembly

(42.5 ± 5.2 Pa). It is important to note that [WW] showed a steep increase of G' and G'' overtime for time sweep analysis after overnight incubation, while the measurements were still in the LVR according to the previous strain sweep test. The reason for this slope might be the orientation of the 1D structures. The immediate measurements were performed directly after the addition of the first negative and then positive counterpart of each pair. However, for overnight incubation at room temperature, the pairs were mixed in an Eppendorf tube. The hydrogels were placed onto the rheology plate with a pipette, which might produce shear thinning of the hydrogel.¹⁴⁷ A similar increase in G' was also observed for [II], but was insignificant compared to [WW] and G' values for the samples plateaued after a short time. In the case of [AA], the G' value reduced throughout the measurement, which might be due to the loss of weak interactions in [AA].

2.3 DISCUSSION

In this study, we introduce CoOPs as a unique and simple molecular discovery tool to identify the effects of intermolecular interactions on the assembly mechanism and mechanical properties of end products. By changing only two amino acids in the appropriate substitution domain of hexapeptides (AA, WW, and II) (Fig 2.1), we show dramatic differences in peptide assembly kinetics, secondary structure, and mechanical properties. The design of this simple molecular framework drives the assembly along a certain pathway, into a 1D structure, to assess, quantify, and compare the effects of different interactions by simple substitutions. There are three important properties of this framework provide quantification: simplicity, assembly into 1D systems, and water solubility.

The analysis of free energy levels through molecular dynamics revealed that charged amino acids in this framework enhance the initial peptide aggregation; however, further assembly and stability are derived from interactions among the amino acid side chains in the core of the framework. Among the CoOPs we studied, [AA] side chains do not form a tight solvent-free core in the lowest free energy state (Fig. 2.2A). This is likely due to the size mismatch of sidechains preventing a compact packing of peptides. A similar side-chain size mismatch was shown previously where co-assembled monomer F and A amino acids phase-separated due to their different intermolecular packing distances.¹⁴⁸ However, [II] side chains were found to be packed closer in their lowest energy levels (Fig. 2.2B). This indicates that, at this distance, the sidechains of [II] are strongly interacting. Previously, co-assembly of I and F amino acids led to merged structures due to their similar hydrophobicity and side-chain lengths.¹⁴⁸ Observation of two local minima of distance between [WW] in Fig. 2.2 corresponds to cation-p interactions formed at $r \sim 6\text{Å}$,¹⁴⁹ and $\pi-\pi$ stacking at $r \sim 3.92\text{Å}$.¹⁵⁰ Furthermore, [WW] showed a slight local peak in the free energy profile at $r \sim 1\text{ nm}$ that may be due to orientation in $\pi-\pi$ stacking. To make the system energetically favorable, the preferred interaction between aromatic rings should be either face-to-face or edge-to-face;¹⁵¹ however, if two aromatic rings are different (a heteroaromatic system), the phenol group in the F side-chain may interact with the face of a W side-chain perpendicularly. Such an arrangement could disrupt the system and lead to a decrease in $\pi-\pi$ stacking.

Further analysis of free energy levels was conducted by considering the side chains of individual hexapeptides and co-assembled forms (Fig. 2.4). For all hexapeptide pairs of the same charge (i.e., either pos-pos or neg-neg) the net charges repel, resulting in higher

free energy values. Such repulsion among similar charges correlates with the design rationale for the CoOP system by enhancing the solubility. However, as seen in Fig. 2.4, even for hexapeptides with the same net charge the F-F interactions are more favorable - indicating that the addition of more F side chains to the peptides might eventually overcome electrostatic repulsion (a phenomena known as "molecular frustration").¹⁵² Importantly, the same-charged CoOP system using [WW] showed markedly less favorable F-F interactions than indicated by the [AA] and [II] systems; instead the interactions between W-W and K-W appeared more favorable. Since there is no salt bridge formation in the same charged groups, this suggests that F-F did not reach the required distance or orientation to provide the low energy levels seen in other systems. For all groups, the presence of salt bridges appeared to support F-F interactions in co-assembled form as indicated by consistently low energy levels for these interactions compared [AA] and [II]. All these observations show the importance of salt bridges in the CoOP system.

The probability of first contacting side-chain residue analysis via MD as shown in Fig. 2.5 is particularly important as it shows the role of salt chains. In [II] and [AA] systems, the charged residues form the initial interactions. Because of favorable cation- π interactions between the (-NH₃⁺) of K and high electron density aromatic ring of W,^{145,149} the effect of salt bridges is hindered in the [WW] system. In addition, the K sidechain produces a relatively weak repulsion compared to E side-chain, even when present at both ends of a peptide,¹⁵³ which might also enhance the involvement of K in cation- π interactions. This involvement may reduce salt bridge formation by moderating the interactions between K and E, causing the final co-assembled structure to be more amorphous. Previously,

hydrophobic core regions were found to dominate for a "reverse assembly" process and salt bridges were the first to break, indicating that salt bridges are likely not essential for stability after co-assembly. Here we find that electrostatic interactions / salt bridges are important to initiate aggregation in the co-assembly of these peptides, but the subsequent assembly and stability are derived from the amino acids in the core of the hexapeptide. As a result, the computational analyses of the free energy levels revealed that the interactions among [AA] are the least favorable compared to [WW] and [II] systems. The ASA trend and β -sheet propensity of chosen amino acids defined the favorability of their CoOP systems, while the initial interactions are likely to happen between the electrostatic groups. The distance between the peptides is inversely correlated to their ASA, the higher the hydrophobicity of the substitution domain amino acid, the longer the distance between the peptides.

The CAC values followed the trend of the distance between the peptides measured in the simulations (Table 2.2). The closer proximity of the peptides for the formation of interactions require higher concentrations, while interactions that act over even longer distances are more favorable (as in [II] system). Therefore, the most favorable [II] system showed the lowest CAC, while the least favorable [AA] interactions did not show CAC at the concentrations studied (Fig. 2.9). As shown in simulations, [AA] requires the closest proximity for the full interactions, which requires higher concentration, the CAC was not observed above 1 mM working conditions. Similarly, the simulations showed [WW] peptides in closer proximity than [II] peptides, as correlated to the narrower hydrophobic ASA of [WW] domain, which resulted in higher CAC concentration than [II]. The kinetics of the assembly of these systems are also relevant to the distance between the interacting

peptides, which makes them also more favorable in terms of the free energy differences of the assembled systems. Inevitably, [II] assembles more rapidly than [WW], while [AA] does not assemble into hierarchical order at comparable timescales. Importantly, the simulation results indicate that interactions between the [AA] peptides might lead to short and instantaneous oligomers instead of large order assemblies without stable β -sheet structure. Furthermore, above the CAC, [II] gave the strongest intensity at 50 and 100 mM within the peptide groups in immediate DLS analysis (Fig. 2.10). Incubation for overnight (Fig. 2.11) did not change in intensity levels for 50 and 100 mM since the co-assembly of [II] was the highest among other peptide groups and [II] reached the stable state within 15 min as we observed with Congo red assay Fig. 2.9D). However, [WW] reached the stable state at 20 h (Congo red assay) and therefore we saw a dramatic increase in DLS measurement of aggregation for overnight incubation (Fig. 2.11). The results of experimental kinetics measurement are found to correlate to the distances between interacting peptides and the thermodynamic free energy measurements, and thus, the experimental and computational analyses are integrated to explain the complex assembly kinetics, demonstrating the advantage of the CoOP system's simple design.

Upon assembly, the [II] system showed ordered β -sheet structures despite the longest distances between the interaction of KFFIIK and EFFIIE (Fig. 2.13B, green). It can be speculated that the distance between [II] peptides in their lowest energy level might be appropriate for salt bridge formation between K and E, and further favorable conformation of the hydrophobic I side chains. This also suggests that despite the slightly lower free energies and the shorter distance between [AA] and [WW] peptides, they do not form

organized assemblies as [II] does at this low concentration. However, more studies are necessary to add further support for this speculation.

Finally, the connection between the mechanical properties of the assembled end products and the results of the MD analyses is identified with the CoOP system. Analyses were performed immediately upon mixing the peptides to show the effects of the initial interactions over mechanical properties, which was also studied in MD simulations. The trend of the mechanical properties measured in the experiment was similar to the MD results, and to previous characterizations: [II] showed the fastest assembly and highest storage modulus upon mixing, followed by [WW], while [AA] did not show a hydrogel formation at this concentration. Overnight incubation increased the mechanical properties of all systems, including [AA], which shows the systems were dynamic and assembly continued, but the amplitude of change was still lowest for [II] system, showing that the conformation of the peptides in this system occurs fastest. The MD simulations indicate that the initial interactions (electrostatic, in these examples) are necessary for aggregation. The assembly into fibrillar structures requires conformational changes of the side-chains of the amino acids in the core, as well as hierarchical assembly of the fibrils. All of these assemblies are time-dependent and affect the length of the fibrils and their entanglement, and thus the mechanical properties of the overall structure. The enhanced mechanical properties of the network after overnight incubation at room temperature indicates time-dependent enhancement of the fibrillar and network structure, and thus the thermodynamic influences on this self-assembly (Fig. 2.15 and Fig. 2.16). As such, the time has a strong effect on fibrillar maturation (Fig. 2.10 and Fig 2.11).

The hydrophobic ASA is directly affecting the interactions between the peptides (the lowest free energy and assembly kinetics), structural organizations (ordered β -sheet), as well as mechanical properties. Moreover, these results are highlighting the importance of salt bridges on stability in mechanical properties; [II] has the opposite charges around the hydrophobic core, the charges are interacting with each other rather than the hydrophobic core amino acids. In the [WW] case, charges are also interacting with the core, disrupting the hydrophobic core and make [WW] harder to be stabilized and change the mechanical properties the most significant way. This effect can also be seen in individual DLS measurements (Fig. 2.12). In immediate analysis, KFFWWK was the only group that resulted in the highest aggregation level. Furthermore, TEM and AFM images of [WW] showed more heterogenous fibrillar structures. Therefore, an undisrupted hydrophobic core was shown to be an important parameter for establishing the assembly in CoOP, while charges around the hydrophobic region enhance the stability.

2.4 CONCLUSIONS

In this study, we introduced a new approach to analyze the intermolecular interactions by combining computational simulations and experimental methods. We leverage MD to reveal information on the initial interactions between peptide sidechains at a molecular level to confirm our design principles, rather than "predicting" the entire assembly process. Without appropriate sampling, the full time-and length-scale of the molecular simulations cannot fully reproduce the experimental systems. The rapid assembly process of CoOP systems is a problem for practical experimental sampling, but analysis of the initial interactions via MD confirmed our design rationale for the addition of charged

peptides on both sides. Moreover, this approach enables the discovery of new peptide sequences and functionalities by combining both screening and editing of various amino acids with MD and experimental techniques. The strategy we describe here provides screening of both natural and non-canonical amino acids in a special substitution domain of the predetermined assembly framework, with the kinetics and assembly mechanism dependent on the substitution domain.

Applications of peptide-based nanostructures are growing, and it is, therefore, valuable to combine experimental, theoretical, and computational methods to explore and define structure-property relationships.¹⁵⁴ A fundamental understanding of intermolecular interactions is the key to engineer complex soft materials that translate effectively from laboratory conditions into everyday life.¹¹⁸ A simple, carefully designed peptide platform that can deconvolute the otherwise complicated influence of non-covalent interactions on bulk material properties will therefore provide an important tool for molecular engineering. In this regard, the CoOP system is a minimalist approach (experimentally and computationally) for peptide assembly studies. CoOP provides a flexible and robust platform to study and compare the effects of intermolecular interactions and correlates the computational thermodynamic and experimental kinetic analyses to mechanical properties. Therefore, our results can provide the foundation for engineering peptides to produce soft materials with desired and predictable properties. CoOP thus has the potential to pave the way for a materials genome atlas for peptide-based materials.¹⁵⁴

2.5 MATERIALS AND METHODS

Materials. Congo red dye and pyrene were purchased from Sigma-Aldrich. Deionized water (resistance of 18.2 M Ω .cm) was used during the experiments. Peptides were purchased from Biomatik (Biomatik Corporation, Canada) with higher than 95% purity.

Critical Aggregation Concentration (CAC) determination. CAC of peptides were examined using pyrene based on previously published procedures with slight modifications.¹⁵⁵ Aliquots of pyrene solutions (225 mM in acetone, 4 mL) were added to positively charged peptide (500, 250, 125, 62.5, 31.25, 15.6, 7.81, 3.9 mM) before the addition of negatively charged peptide (500, 250, 125, 62.5, 31.25, 15.6, 7.81, 3.9 mM). The final pyrene concentration in the system was 4.5 mM in micro-plates. Solutions were left for 30 min to reach equilibrium. Excitation was carried out at 334 nm, and emission spectra were recorded ranging from 360 to 600 nm with a microplate reader (BioTek Neo2SM). Both excitation and emission bandwidths were 9 nm. From the pyrene emission spectra, the fluorescence intensity ratio of the vibronic bands (I₃₉₇/I₃₈₀) was plotted against the logarithm of the concentration of the self-assembled peptides. Fitting of the data set was performed with a model of four-parameter logistic curve by using GraphPad Prism 9.0.0. Then CAC value was calculated from the intersection of the tangents.

Congo Red Assay. Congo red assay is used for amyloid fibril detection. In the presence of high β -sheet organization, Congo red lies parallel to the fibril axis and induces a red shift in the absorption maximum (498 nm). Congo red dye was dissolved in water to a final concentration of 500 mM. For sample preparation, stock peptides in water (10 mM)

diluted to 1 mM in water. Then 1 mM of negative peptide (50 mL) added to 96 black well plate, then 1 mM of positively charged peptide (50 mL) added to the same place. 2 mL of 500 mM Congo red is immediately added to the solution and read at microplate reader (Bio-Tek Neo2SM) at room temperature, spectral scanning for absorbance was adjusted between 400- 600 nm. The control group of only Congo red dye in water was also prepared with a final concentration of 10 mM. The analysis was performed for 2 days with 10 time points. Spectral shift was calculated based on Congo red only absorption maximum.

DLS measurements. Hydrodynamic size and zeta potential of single and mixed peptides were measured by dynamic light scattering (DLS). A The ZetaSizer Nano ZS (Malvern, UK) instrument with detector angle of 173° was used for analysis. Clear disposable cell cuvettes first washed three times with 0.22 μm filtered deionized water (resistance of 18.2 $\text{M}\Omega\cdot\text{cm}$). Before measurements, peptide solutions in PBS were also filtered with 0.22 μm filter to avoid any dust that can alter the measurements. For individual peptides, 500 mM (500 mL) positively and negatively charged peptides were used. For mixed peptides, equimolar (500, 200, 100, 50 and 25 mM with 200) of positively (250 mL) and negatively (250 mL) charged peptides were mixed. The analysis was performed with 3 scans and 21 measurements in each scan.

Rheology Measurements. Rheology measurements of 10 mM samples at pH 7 were performed to understand the mechanical properties of the resulting gels. At rheometer stage first negatively charged and then positively charged peptide was added then immediate analysis was performed. For overnight analysis, 10 mM equal volumes (200 mL each) of oppositely charged peptides were mixed in Eppendorf tubes and incubated

at room temperature overnight (21 h). Total volume of samples was 200 mL (100 mL positively charged, 100 mL negatively charged peptide). A Discovery Hybrid Rheometer-2 (TA Instruments, New Castle, DE) equipped with parallel 20-mm plate was used for the analysis. Measuring distance was determined as 0.5 mm. Time sweep tests of each sample were carried out for 20 min. Angular frequency and strain magnitudes were determined as $\omega = 10$ rad/s and $\gamma = 0.1\%$, respectively. To determine linear viscoelastic region (LVE), amplitude sweep tests of 10 mM samples at pH 7 were performed in the same configuration and concentration. Strain value logarithmically increased from 0.1 to 10%, total of 17 value was measured. Angular frequency was kept as constant at $\omega = 10$ rad/s.

FTIR and CD measurements. Peptides with different concentrations (1000, 500, 200, 100 and 50 mM) were prepared in water and analysis was performed immediately. For [AA], [WW] and [II] groups, equal volumes of charged peptides were mixed (as a total of 20 mL) and put directly into FTIR stage. Analysis was performed with Bruker Tensor II with BioATR II unit. For background spectrum, water was measured first then peptides in water subtracted automatically in the device. Analysis was performed between 1800 and 900 cm^{-1} with 4 cm^{-1} resolution and 60 scans. For CD measurements, analysis was performed in water with a concentration of 200, 100 and 50 μM for co-assembled peptides and 200 mM for individual peptides with a volume of 1 mL. Jasco J-715 was used to collect spectra from 190 to 400 nm with 0.1 nm data pitch and bandwidth arranged as 1.0 nm.

AFM measurements. Peptide samples were prepared by dilution of 10 mM of co-assembled samples to 0.2 mM with water. Then, 20 mL of diluted peptide samples were

dropped onto silicon wafer and dried at room temperature. Topographic imaging was performed in contact mode using an Asylum Research MFP-3D AFM with an Asylum Research cantilever probe (Model: TR400PB, Lot number: 3733FB). Scanning frequency was 2 kHz and data points were taken in a 128x128 grid over 3x3 mm² area.

Molecular Dynamics. Molecular dynamics calculations used Gromacs 2020.03 as driven by GromacsWrapper. The CHARMM27 forcefield was used for modeling the peptides because it has good parameters for acetylated and amidated N/C termini. A time step of 2 fs was used to integrate the forces and simulations were performed in the NVT ensemble using the Canonical Sampling through Velocity Rescaling (CSVR) thermostat. Long-range electrostatic forces were calculated with the particle mesh Ewald method. Shifted Van der Waals and short-range electrostatics were used with a cutoff distance of 1 nm. Hydrogen containing covalent bonds were constrained using the LINear Constraint Solver (LINCS) algorithm. Initial structures of peptides were generated with PeptideBuilder and Packmol was used to pack together multiple peptide chains into a single coordinates file under the constraint that peptides were at least 2.5 nm apart. Water and NaCl counter-ions were added to reach a peptide concentration of 25 mg/mL and a salt concentration of 10 mM. Although the concentration is relatively high, aggregation thermodynamics are relatively independent of box size. The PLUMED2 package was used to calculate radii of gyration, center of mass distances, and perform metadynamics enhanced sampling. MDTraj was used to compute contact maps, which were reweighed to account for the metadynamics bias. All systems were energy minimized. Metadynamics simulations were additionally equilibrated for 2 ns in the Berendsen isotropic NPT ensemble. Unbiased simulation used for kinetics analysis were run until all four peptide

chains had a center of mass distance of less than 1.25 nm among their closest neighbor (~5-50 ns). Metadynamics simulations were run for 500 ns. The 16 peptide chain WW simulations were run for 392 ns. Metadynamics simulations were biased with the enhanced sampling well-tempered metadynamics method with a bias factor of 5, pace of 1 ns, and a hill height of 5 kJ/mol. The biased collective variables are average center of mass distances between chains ($s=0.05$ nm) and average radius of gyration of the chains ($s=0.01$ nm) with only backbone atoms considered.

CHAPTER 3. CONTROLLABLE MEMBRANE DAMAGE BY TUNABLE AGGREGATION

This section is adapted from the following publications:

From: Hamsici[#], S., Gunay, G.[#], & Acar, H. (2022). Controllable membrane damage by tunable aggregation of PAIIR with albumin. *AIChE Journal*, e17893 [#]Contributed equally

Gunay, G., Hamsici, S., Lang, G. A., Lang, M. L., Kovats, S., & Acar, H. (2022). Peptide Aggregation Induced Immunogenic Rupture (PAIIR). *Advanced Science*, 9(21), 2105868.

Aggregation of otherwise soluble proteins into amyloid structures is a hallmark of many disorders, such as Alzheimer's and Parkinson's diseases. There is increasing evidence and acceptance that instead of ordered amyloid assemblies, the misfolded oligomer aggregations are the main toxic structures. However, there is no tool to be used to study the mechanism and kinetics of aggregation, differentiation of ordered structures from misfolded oligomers, and correlate it to the toxicity of the amyloid structures. Thus, their exact roles in the pathological process remain to be elucidated. This study shows the use of an engineered co-assembling oppositely charged amyloid-like peptide pair ([II]) to establish a correlation between its aggregation process and toxicity. The toxicity mechanism of [II] is through damage on cell membrane and stress as shown with YAP and eIF2 α biomarkers, as in the amyloid protein-initiated diseases. Albumin is used to control over the aggregation mechanism of [II], and so toxicity. This study represents a molecular engineering strategy to study the aggregation process of amyloid-like structures in diseases. Understanding the nature of protein aggregation through

engineered peptides can facilitate new designs and impact the future drug development applications.

3.1 INTRODUCTION

Wide range of proteins aggregate into amyloids, cross β -sheet fibrillar structures, that are linked to numerous diseases, such as Alzheimer and Parkinson. Although for many decades the accumulation of amyloids plaques were associated to the pathology of the diseases, increasing evidence suggests that the misfolded protein aggregates, globular structures, that are soluble and form in the process of fibrillization, are the main cause of the toxicity.^{156–159} A part of their toxicity process occur through the interactions of oligomers of amyloid- β or α -synuclein with the lipid membranes of cells, which initiates a damage.^{62,160} The membrane damage often induces immunogenic cell death and inflammation.^{161–163} The aggregation and oligomer formation process is complex because of the convoluted conditions in the body. The dynamic conditions create transient heterogeneous misfolding of oligomers and makes the molecular level of understanding, quantifying, and correlating the aggregation mechanism and toxicity challenging, and thus the development of drug targets.^{159,164} Therefore, a minimalist and simplified synthetic model that mimic the structure, aggregation, and function of amyloids can serve as a powerful tool for studying their aggregation mechanism.

The molecular events that occur during the formation of small aggregations of proteins and peptides (lag phase) are in a complex environment. Studies with the extracted proteins in an isolated system may not provide an adequate understanding of the pathophysiology of the disease. Yet, studies in biological fluids create huge complexity.

Indeed, the amyloidogenic proteins' kinetics and free energy landscape in the initial aggregation phase are largely unknown and have been studied with variations of new experimental and computational approaches.^{133,165–167} A combination of these methodologies establishes strategies for a more accurate understanding of the aggregation process. Such a combination can be possible with molecular tools that have similar behaviors and biological functions in experimental conditions as amyloid-like proteins and are simple enough for computational simulations.¹⁶⁸

Co-assembly of oppositely charged peptides (CoOP) is a minimalist strategy allows the study the role of intermolecular interactions in peptide aggregation.¹⁶⁸ CoOPs are designed to assemble into amyloid fibrils. Among the studied peptide sequences, the oppositely charged pair, KFFIIK and EFFIIE (the pair will be shown as [II] in the rest of the paper), showed the highest order of amyloid- β assembly. On the cell membrane, [II] peptide-aggregation induces immunogenic rupture (PAIRR) that initiates immunogenic cell death (ICD) and release of damage associated molecular patterns (DAMPs) as an immunostimulatory tool.¹⁶⁹ PAIRR induces secondary pyroptosis, an immunogenic programmed cell death and a common feature of amyloid inducing cell death as in Alzheimer and Parkinson.^{170,171} PAIRR is a simplified peptide-based tool, designed to mimic the function, instead of the sequence of a protein; thus there is no natural ortholog of [II].

Albumin is abundant in the human body, it is flexible, and mostly hydrophobic, and thus, have high non-specific binding capacity.¹⁷² It is known that albumin impedes the fibrillization of amyloids and increases the soluble misfolded oligomers that have higher toxicity than amyloid fibrils.^{173–175} Akin to amyloid, co-aggregation with albumin creates

soluble oligomeric form of [II] that is more toxic than its fibril form. In this study, we show the control over the aggregation kinetics and mechanism of [II] via albumin. The simplicity of [II] as an engineered tool allowed the detailed characterization of aggregates and their interactions with the lipid membranes that we showed with liposomes and fluorescent tagged peptides. We showed that the soluble form of peptides misfolded with albumin can integrate into the lipid membrane, while the ordered fibril structures do not interact with the liposomes. We studied the kinetics of the aggregations with spectroscopic methods with fluorescent probes. The morphology of globular aggregates to ordered fibrillar structures were analyzed by dynamic light scattering (DLS) and atomic force microscopy (AFM). In parallel with membrane localization, cellular cytotoxicity followed the similar trend. While fibrillar form of [II] did not cause any membrane damage and cellular cytotoxicity by delaying the peptide ordered fibrillization via albumin or by simply introducing the counterpart peptides in different time point, which allowed enough time for membrane localization to the soluble peptides. Lastly, the mechanism of cell death was correlated to the mechanical cell stress, identified through the phosphorylation of yes-associated protein (YAP) and eukaryotic initiation factor 2 alpha (eIF2 α) and found that the cell stress markers like amyloid-b induced cytotoxicity. Importantly, we identified these stress markers in the cells treated with misfolded oligomers, not with ordered amyloid fibrillar form of [II]. Overall, [II] presents a simplistic tool to study the effects of physical and biological processes to understand aggregation process and function of amyloid like pathological proteins.

3.2 RESULTS AND DISCUSSION

3.2.1 PEPTIDE DESIGN AND AGGREGATION ANALYSIS

Engineering the fine-tuned cellular aggregation of peptides requires well-characterized intermolecular interactions^{106,116}. Understanding these interactions allows the rational design of peptides to encompass desired properties, such as aggregation on the cell that induces stress for inducing ICD and cell membrane rupturing for DAMP release. We utilized the CoOP strategy to design peptides with strong enough affinity to aggregate in the cellular environment. The local charges in this design promote electrostatic interactions between two oppositely charged amino acids; the anionic carboxylate of Glutamic acid (E) and the cationic ammonium from Lysine (K) (Fig 3.1) The deliberately short, charged design enables the internalization of CoOP-based peptides into cells¹⁷⁶. Design studies on multidomain peptides revealed the importance of hydrophobic amino acid localization in the core of the structures¹⁷⁷. In particular, the interplay between the backbone hydrogen bonding and hydrophobic interactions among amino acid side-chains is crucial to the formation of fibrillar structures¹²⁷. Therefore, to change the aggregation kinetics, we studied the hydrophobic amino acids in the substitution domain ("[XX]"), with increasing hydrophobicity indices; [AA] < [VV] < [WW] < [LL] < [II] (Fig. 3.1). LC and MS results were shown in Fig. 3.2.

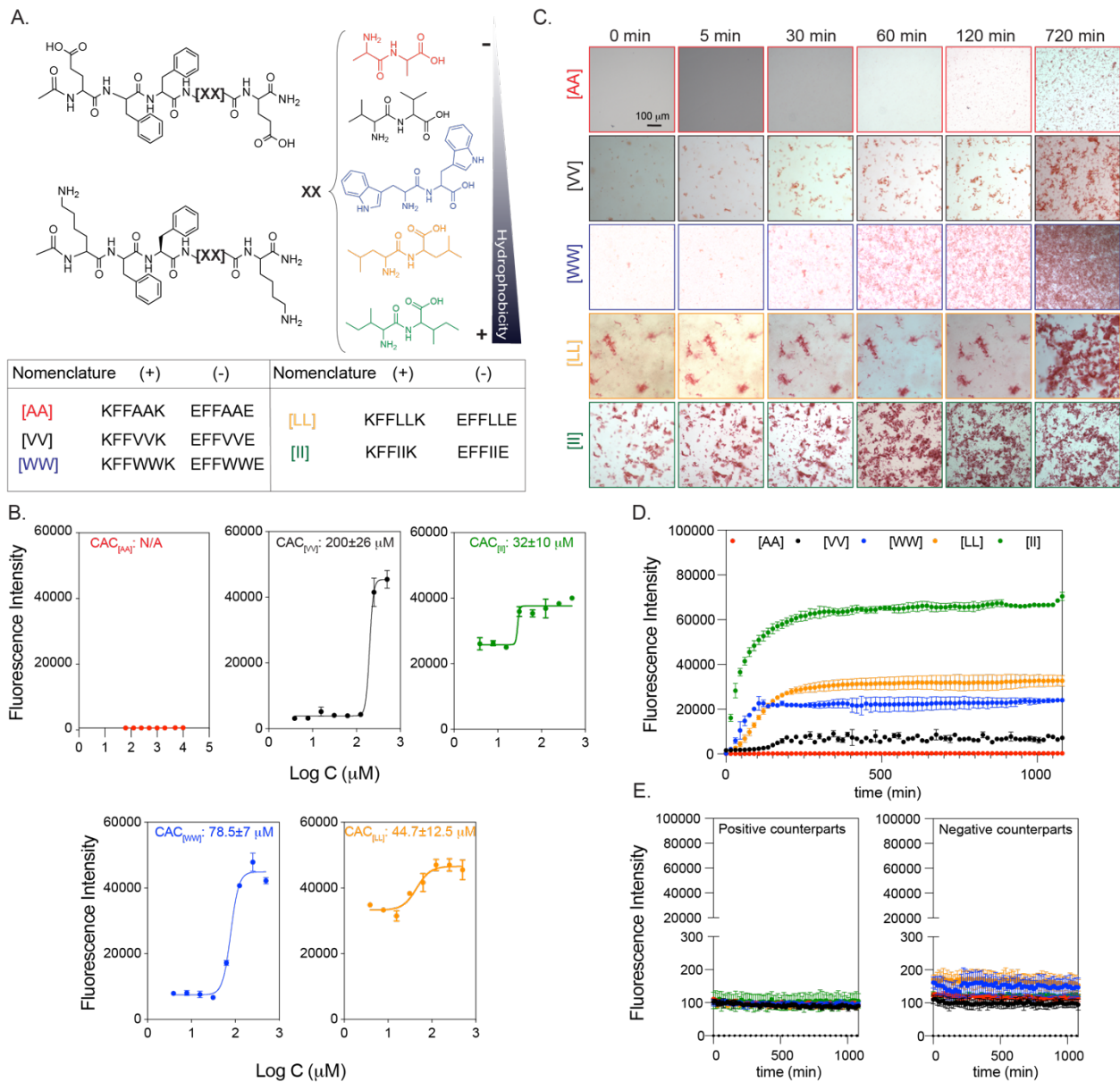


Figure 3. 1 Peptide groups and aggregation kinetics. (A) CoOP groups and individual counterparts were used in this study. (B) CAC of co-assembled peptides with DPH. (C) Macroscopic CoOP aggregates incubated with Congo Red. (D) Determination of aggregation kinetics of CoOPs and (E) individual counterparts by ThT assay. Data are representative of three experiments.

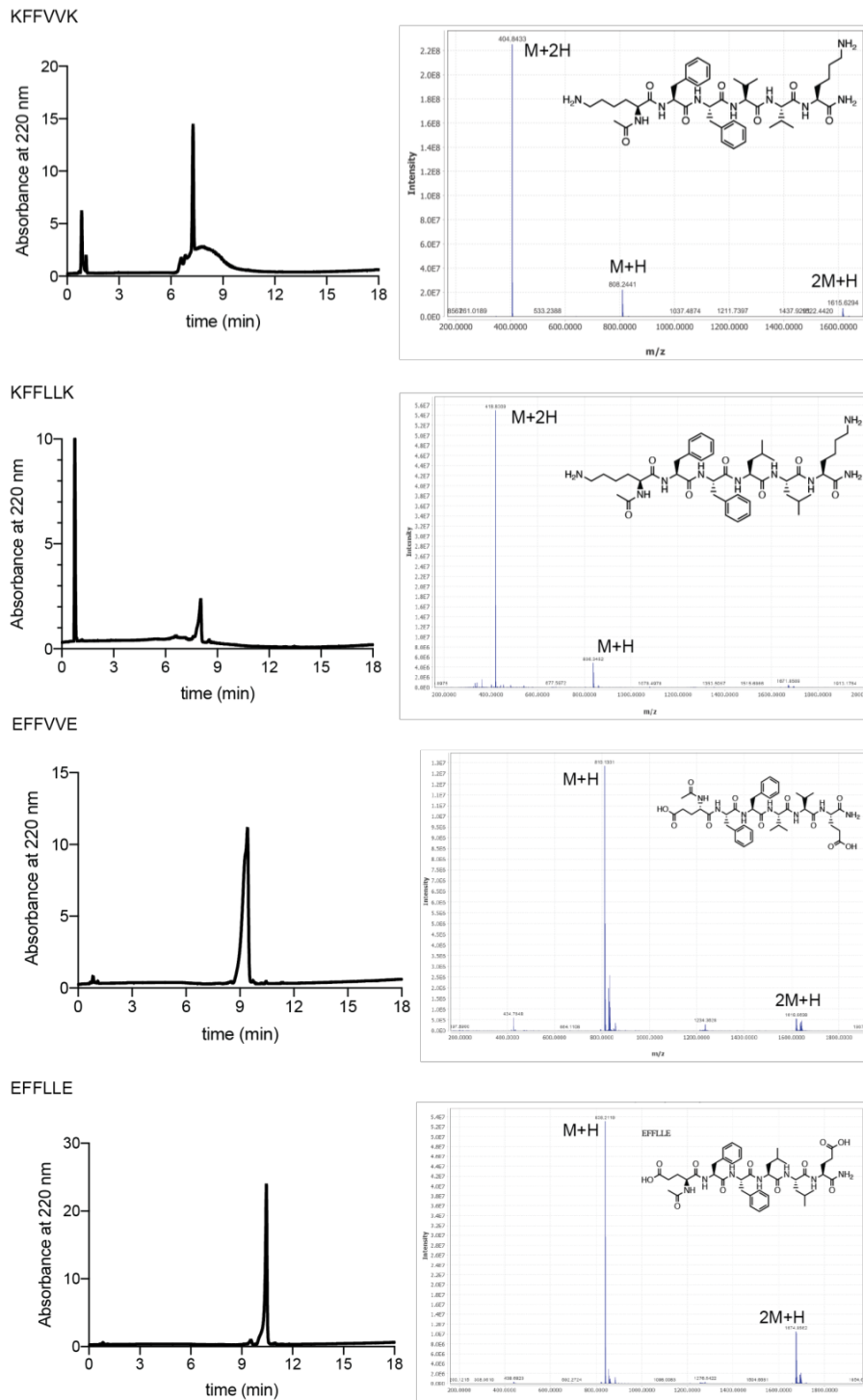


Figure 3. 2. LC and MS analysis of [LL] and [VV] peptides. The exact molecular weight of KFFVVK: 765.49, KFFLLK:793.52 , EFFVVE: 809.4 and EFFLLE: 837.43 m/z.

Characterization assays were performed in 1XPBS to mimic the salt concentration in the physiological conditions. The critical aggregation concentrations (CAC), i.e., the minimum concentration needed for co-assembly of the peptides, are measured with DPH ((1,6-diphenyl-1,3,5-hexatriene)), which becomes fluorescent when located in aggregates with hydrophobic cores¹⁷⁸. The CAC values of [VV]= 200 ± 26 mM [WW]= 78.5 ± 7 mM [LL]= 44.7 ± 12.5 mM and [II]= 32 ± 10 mM followed the same trend as the hydrophobicity of the amino acids at their core. (Fig 3.1B) The identified CAC values were correlated to our previous study¹⁶⁸. No fluorescence was observed for [AA] even at 10 mM indicating no aggregation; therefore, this situation represents an excellent control for studying the effects of peptide aggregation, as the same concentration of peptides with similar sequences and charges will remain free components in solution.

The aggregation kinetics of the peptide pairs were measured with Congo Red and Thioflavin T (ThT) assays. Congo Red staining has been used to identify amyloid fibrils in vitro and tissue sections, emitting red light due to the binding of β -sheet rich domains, leading to a redshift in its absorbance peak from 490 to 512 nm¹⁷⁹. We monitored the fluorescence of Congo red for 720 min (12 h) (Fig 3.1C) at 0.5 mM peptide concentration. [AA] precipitation appeared after 720 min; these are not likely to be ordered aggregates with hydrophobic cores because no DPH fluorescence was observed at this concentration. [II] aggregated instantaneously (0 min), while [LL] aggregates were deposited initially and became stable until 720 min. [WW] and [VV] did not show any initial aggregates but deposited after 30 min and 120 min, respectively. Despite the ease of visualization with red light, Congo Red is not as sensitive as ThT in understanding ordered structures since fluorescence methods (rather than absorption) are preferred for high-

sensitivity detection¹⁸⁰. Therefore, we use Congo Red as a visualization method, with ThT used for quantitative temporal measurements of oppositely charged pairs and each counterpart individually for 1200 min (20 h). To determine the time needed for equilibrium assembly of CoOPs, we applied curve fitting to the ThT analysis (Fig 3.1D). [AA] did not assemble and thus did not show any fluorescence in ThT. For the remaining peptide pairs, the time to reach equilibrium assembly was calculated as [VV] (660 min) > [WW] (675 min) > [LL] (630 min) > [II] (510 min). Individual counterparts did not produce any fluorescence signal (Fig 3.1E). We observed that the like-charged groups alone did not aggregate, highlighting the importance of electrostatic attractions in the aggregation process (Fig 3.1D). Among the studied peptides, [II] showed the fastest aggregation and the highest fluorescence intensity, indicating that [II] has the highest affinity to each other, and these peptides are stacked in a more well-ordered structure than the other CoOPs. The TEM images of the aggregates showed one-dimensional structures (Fig 3.3). The use of the FF group in the CoOP sequence was for enhancing the one-dimensional aggregation; thus, the observed structures were expected. These results indicate that control over peptide aggregation is achieved by changing the hydrophobicity of amino acids in the substitution domain.

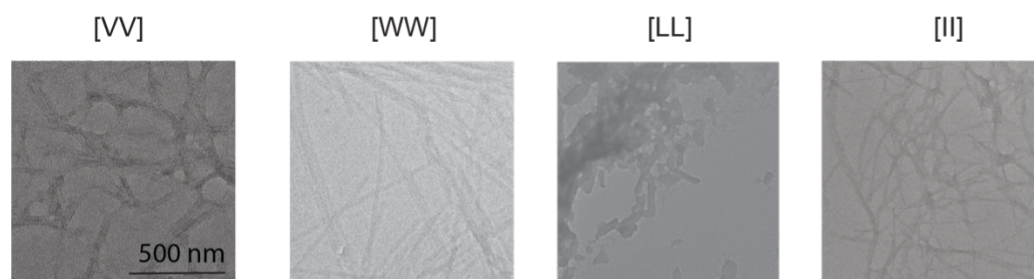


Figure 3. 3 Morphological analysis of peptide structures. TEM images of [VV], [WW], [LL] and [II] peptides. Scale bar: 500 nm.

3.2.2 CELL VIABILITY ANALYSIS

We used the human ovarian cancer cell line OVCAR-8 as our initial model to identify the effect of the peptides on cells. All cell culture experiments were performed in an RPMI cell culture medium with 10% FBS. At 0.5 mM (i.e., above the overall CAC), the individual peptides mixed on the cells by promptly adding the first negative, then positive counterparts. The viability of the cells was measured for 6h through live-dead imaging (Fig 3.4A) Among the peptide groups studied, [AA], [VV], and [LL] did not affect cell viability in the measured time frame (Fig 3.4A). Only [WW] and [II] caused cell death compared to the control group. Because the peptides, if aggregate, form one-dimensional structures, the shape of the aggregates is not likely to be effective on the action of the peptides. [II] has the lowest CAC and highest ordered aggregation (Fig 3.2B, C, D). Additionally, the equilibrium time of [II] aggregations was the shortest among the tried groups. These all indicate that [II] peptides have the highest affinity to each other, which creates aggregations strong and fast enough to induce cell death.

To understand the effect of peptide aggregates versus peptides alone on the cell death identified with [WW] and [II], we performed a live/dead assay with individual peptides at 0.5 mM after 6h (Fig 3.4A). Despite the dramatic cell death observed with the [II] mixture at this concentration, the individual [II] peptides did not induce cell death. Similarly, the negative [WW] (EFFWWE) peptide alone did not show any cell death, yet the positive [WW] (KFFWWK) peptide induced the cell death (as indicated by red-stained cells). Positive charged peptides containing W are promiscuous residues for membrane damaging peptides, possibly because of W's "anchoring" role; W is abundant in membrane proteins, particularly near the lipid-water interface^{181,182}. Furthermore, as

analyzed by zeta-potential, individual peptides showed the expected overall charges at pH 7.0 ((pKa of (-COO⁻) of E is 4.25 and (-NH³⁺) of K is 10.53) (Fig 3.4B, inset). In an aqueous solution, the [II] aggregates acquire a neutral charge in 5 min, while [WW] showed a slight positive charge after 30 min, possibly due to incomplete assembly (Fig 3.4B).

Given the effects of individual [II] and [WW] on cell viability, we examined the order of addition of the peptide counterparts; first positive and then negative peptide, and vice versa (Fig 3.4C). The addition of KFFWWK first induced significantly higher cell death (****p<0.0001) compared to the initial addition of negative peptide, indicating that the cell death is due to the positive charge of KFFWWK (Fig 3.4D). Yet, any order change did not affect the membrane damage activity levels for [II] (Fig 3.4E). Moreover, mixing the peptides for 30 min or 24h before addition to the cells completely abolished the effect of [WW] (Fig 3.4D), indicating that the initial membrane damage was due to the positive charge of KFFWWK which was neutralized upon mixing and aggregation with its counterpart. Nevertheless, the pre-mixing did not alter the effect of [II] under these conditions (Fig 3.4E), highlighting that [II] is the only peptide pair among those studied that induces cell death through the aggregation of its charged counterparts. Although these charges help peptides find each other even in low concentrations, the electrostatic interactions do not contribute to the stability or thermodynamic assembly of the peptides, which happens only through the hydrophobic amino acids in the core of the sequence¹⁶⁸. Our results show that increasing the hydrophobicity of the amino acid decreases the aggregation time, which has a direct effect on cell membrane damage. Isoleucine is the most hydrophobic canonical amino acid, and [II] peptides have the highest affinity among

the studied pairs and showed the lowest CAC in the shortest aggregation equilibrium time. The affinity among [II] creates strong aggregates to induce cell cytotoxicity.

3.2.3 CELL MEMBRANE RUPTURE THROUGH PEPTIDE AGGREGATION

The aggregation-induced membrane damage activity was only observed with [II]; we analyzed how it induces cell death. We used propidium iodide (PI) to understand cell membrane damage, a dye that does not permeate intact cell membranes¹⁸³. Fig. 3.5A shows cells treated with three concentrations of [II]: 0.25 mM 0.5 mM and 1 mM for 1, 6, and 24h. Increasing the concentration to 1 mM resulted in faster membrane damage, while decreasing the concentration to 0.25 mM (although still higher than the [II] CAC of 38 μ M did not have sufficient aggregation to trigger membrane damage in this time frame. The time and concentration dependence membrane damage activity of [II] is likely to result from faster aggregation in higher concentrations. These results show that [II] induced cell death can be controlled through time and concentration.

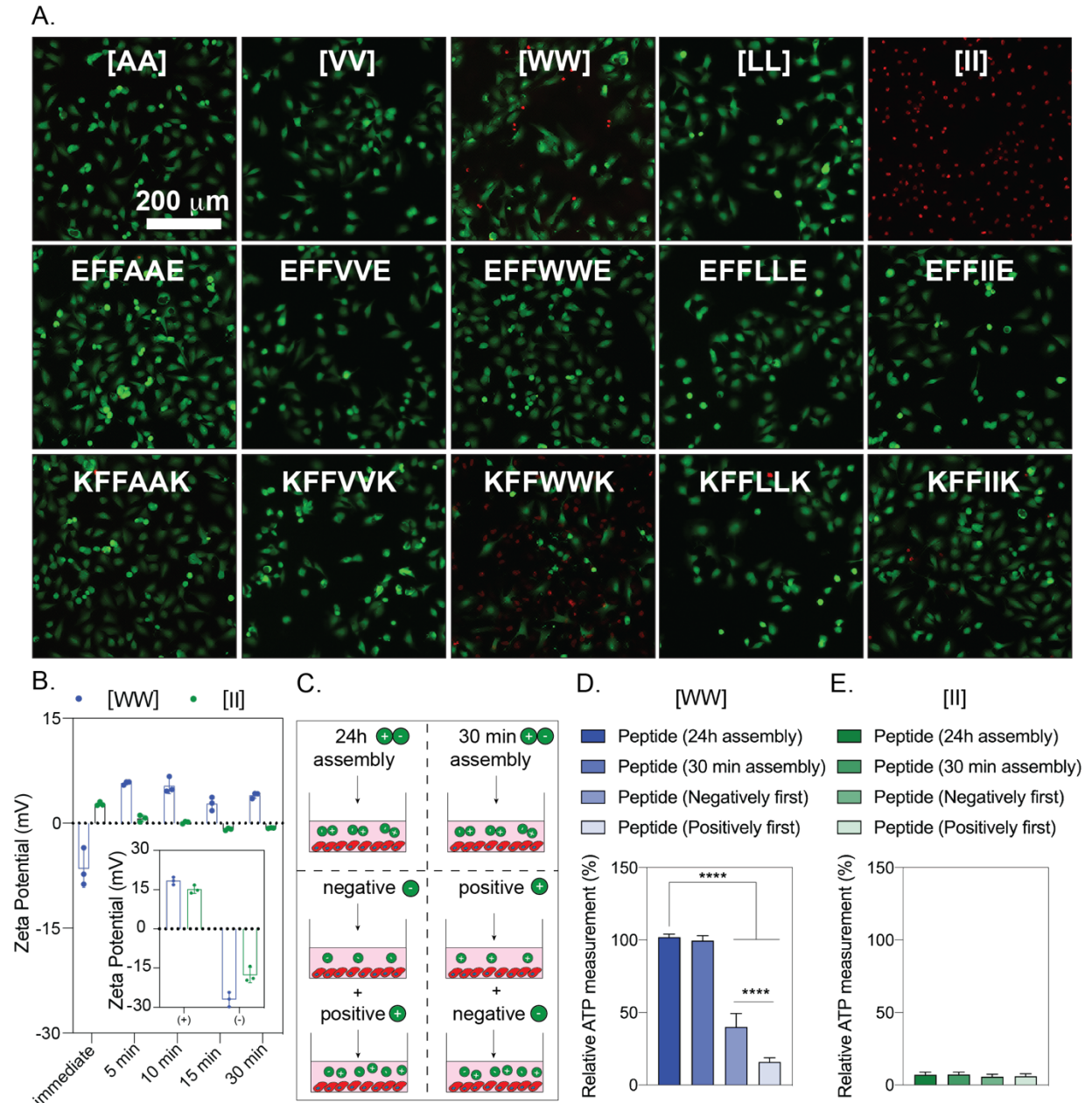


Figure 3. 4 Cytotoxicity of peptides to ovc8 cells. Negative peptides were added to the cells, followed by corresponding positive peptides. (A) live-dead images of ovc8 cells treated with peptide combinations and corresponding individual counterparts at 6h (peptide concentration is 0.5 mm) (B) zeta potential of individual and combined peptides. (C) illustration of peptide preparation for [WW] and [II]. The effect of peptide preparation on cell viability for [WW] (D) and [II] (E). The scale bar is 200 μ m. Data are representative of at least three experiments. Statistical analysis via one-way anova test, data are mean \pm sd, **** p <0.0001.

The confocal images analyses of 0.5 mM [II], which induces >85% of death in 6h (Fig.3.5 B) showed cell swelling and nuclear condensation; hallmarks of necrotic cell death (Fig.3.5C,D). ¹⁸⁴ Aggregation was visualized by labeling the positive charged [II] (KFFIIK) peptide with FITC (green fluorescent). We monitored the internalization and aggregation of KFFIIK through fluorescence microscopy. KFFIIK alone was internalized into the cells starting at 1h (Fig.3.5E), and cellular morphology did not change over time as KFFIIK alone does not cause cell death. When KFFIIK was introduced with its negatively charged counterpart, EFFIIE, the peptide-aggregation (more localized green KFFIIK) was apparent around and within the cells starting at 3h (Fig.3.5F). The peptide-aggregation induced nuclear area shrinking and loss of integrity of the cells (observed through the absence of actin fibers), indicating [II] aggregation-induced cell membrane damage and death.

Overall, among the peptides we studied [II] has the highest hydrophobicity which leads to lowest aggregation and fastest assembly. [II] aggregation also causes the highest cell death in serum albumin conditions. Next, we analyzed how [II] aggregated on cell membrane and how albumin affects the cell membrane damage.

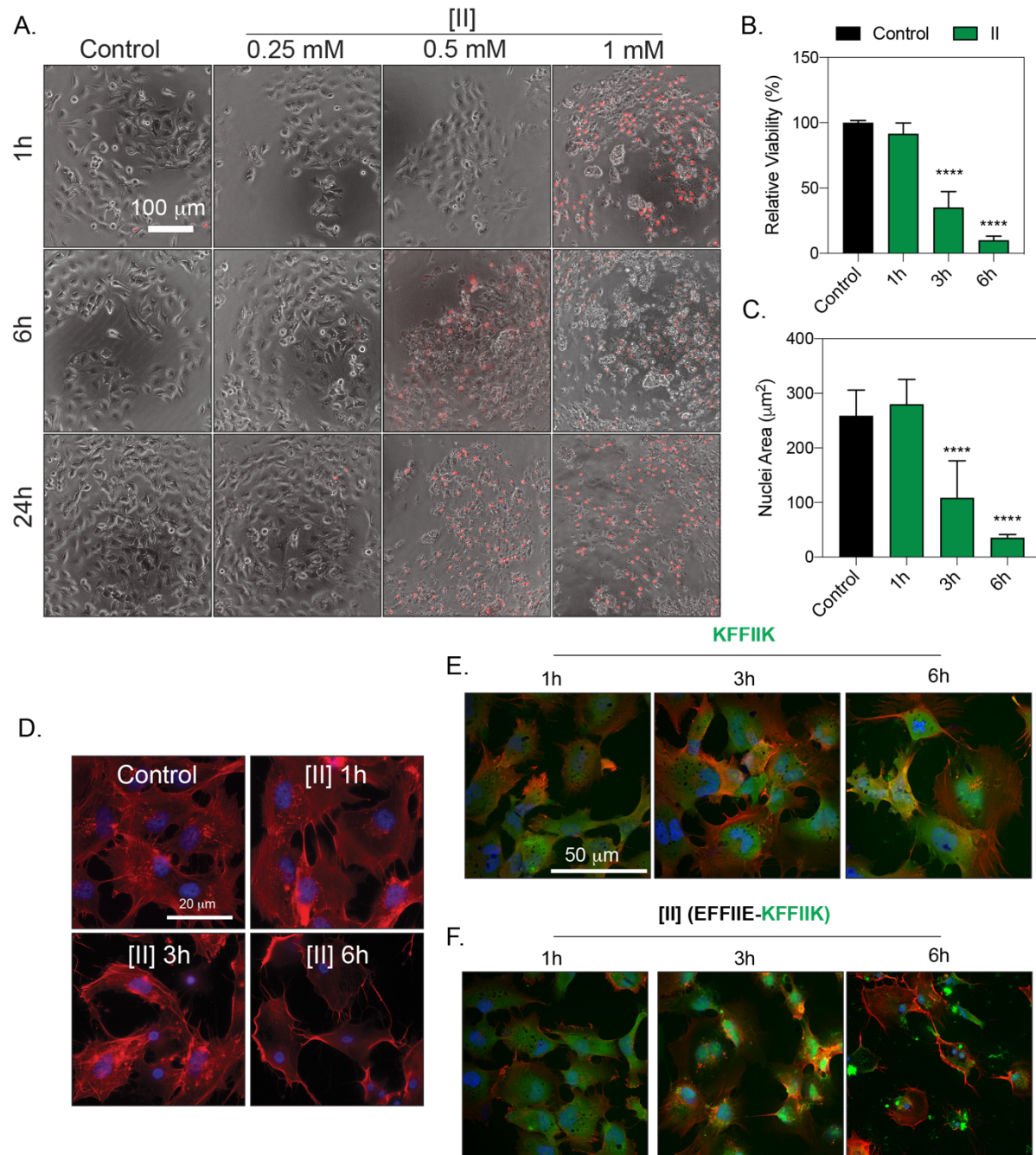


Figure 3. 5 [II] induces membrane rupture. (A) time and concentration-dependent cell membrane damage of [II] were analyzed through pi uptake (scale bar is 100 μm). (B) time-dependent viability measurement and (C) time-dependent nuclear size analysis. (d) actin cytoskeleton staining of [II] treated ocar-8 cells at 1,3 and 6h, scale bar is 20 μm . (e) internalization of FITC-KFFIIK and (f) FITC-[II] for 1, 3 and 6h, scale bar is 100 μm . Data are representative of at least three experiments. Statistical analysis was done with one-way anova test. Data are mean \pm sd, **** $p < 0.0001$.

3.2.4 INTEGRATION OF [II] PEPTIDES INTO LIPOSOME MEMBRANES

The membrane interaction of [II] peptides (Fig. 3.7) was analyzed using a liposomal membrane. Liposomes are commonly used tools for the analysis of interactions between amyloids and lipid membranes.^{185,186} We used the agarose embedded liposomes (blue, app. 100 μm in diameter, Fig 3.6) for long time imaging and the fluorescence tagged [II] peptides (KFFIIK with FITC (green) and EFFIIE with rhodamine B (red)) mixed with unlabeled counterparts (Fig 3.2) to identify their membrane interactions (Fig. 3.8A).¹⁸⁷ 30 min premixed [II] as in Fig. 3.8Ai initiates the interaction of oppositely charged groups, as the charge neutralization was observed through zeta potential (Fig. 3.9). The high affinity of peptides prevented disassembly and localizing on the lipid membrane of liposomes (Fig. 3.8B).

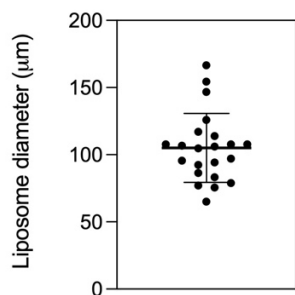


Figure 3. 6 Liposome diameters. Films of agarose enable rapid formation of giant liposomes having around 100 μm in diameter.

Incubation of EFFIIE alone for 60 min as in Fig. 3.8Aii allowed the integration of the peptide into the cell membrane (red fluorescence on blue liposomes). Despite the charge similarities with the lipid, the hydrophobicity of the FFII group might be the reason of this integration. After introducing KFFIIK on the EFFIIE+liposome, green fluorescent (KFFIIK) increased immediately in 5 min, which shows the localized interaction of [II] on the membrane (Fig. 3.8C). Additionally, formation of amyloid fibril aggregation around the

liposomes was also observed, indicates the remaining soluble EFFIIE interacts to its soluble counterpart peptide before integration into the lipids. Similarly, incubation of KFFIIK alone, as in Fig. 3.8Aii, showed integration into the lipid (Fig. 3.8D). The membrane localization of KFFIIK was faster than EFFIIE, likely because of the opposite liposome surface charge.¹⁸⁸ Addition of EFFIIE 60 min later also showed membrane integration of both peptides and fibrillar aggregations of [II] outside of the membrane.

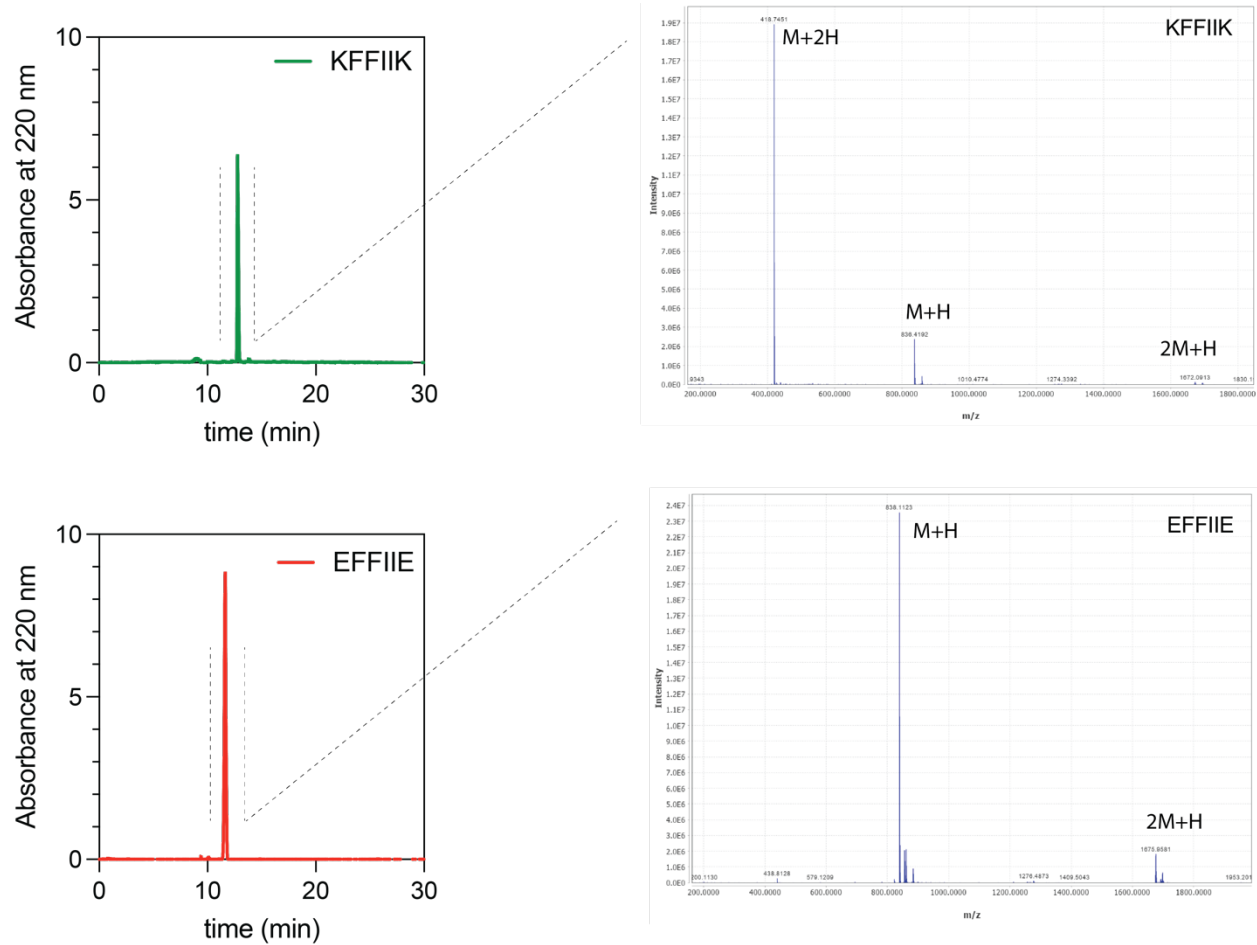


Figure 3. 7 Characterization of peptides after purification. LC and MS analysis of KFFIIK and EFFIIE peptides

Overall, these results demonstrated that the soluble forms of individual [II] peptides integrate into membrane. The pre-mixed [II] did not show a peptide integration, they were stable. The membrane-binding capacity of [II] is correlated to the amount of free peptides in the medium. Controlling the aggregation kinetics of [II], in another words, controlling the time and amount of free peptides in the medium, can control the amount of peptides integrate into the membrane.

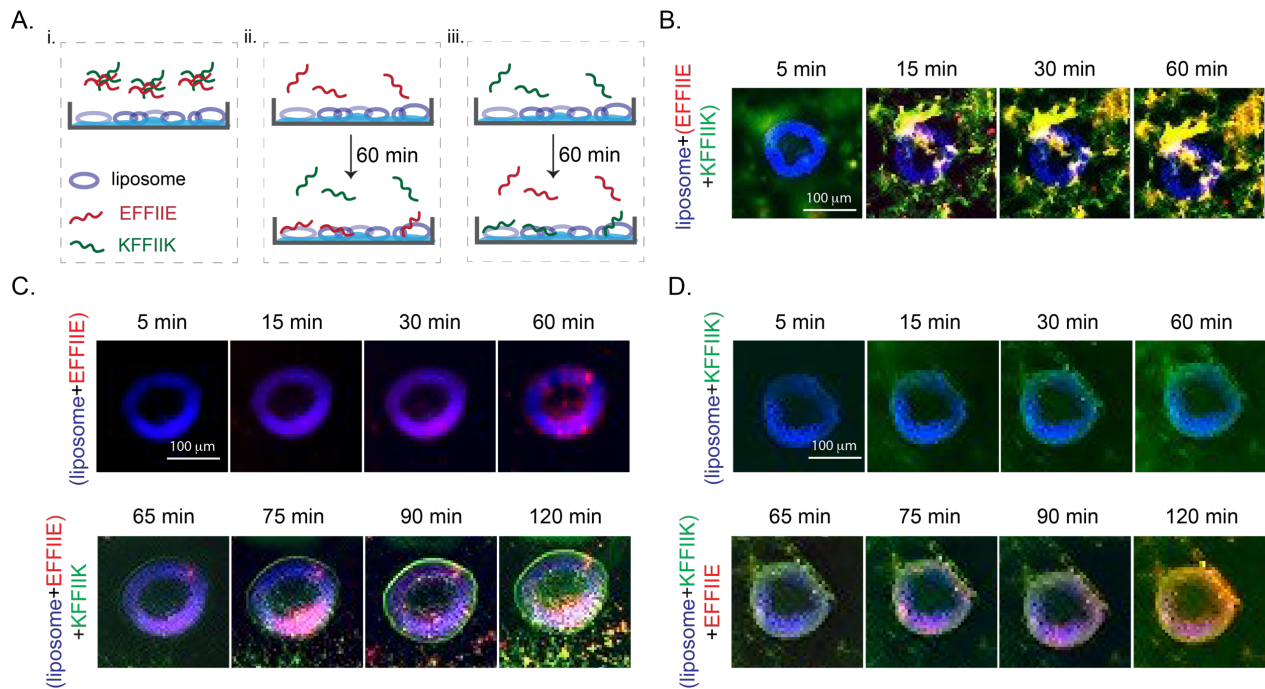


Figure 3. 8 Liposome (blue) membrane integration of [II] and individual peptides; KFFIIK (green), EFFIIE (red). (A) The schematic of membrane localization experiment by using agarose embedded liposomes. (B) Membrane localization of 30 min pre-mixed of EFFIIE+KFFIIK. (C) EFFIIE addition followed by KFFIIK and (D) KFFIIK addition followed by EFFIIE. (Scale bar = 100 μm).

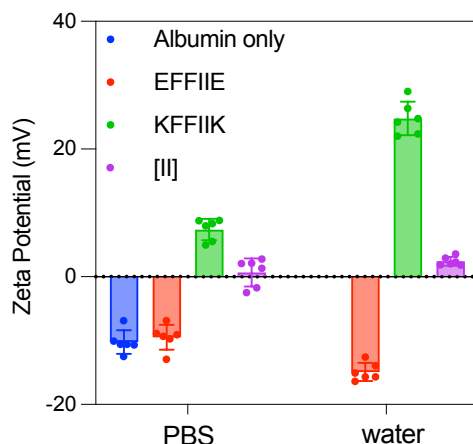


Figure 3. 9 Charge measurements. Zeta potential of individual oppositely charged peptides, co-assembled form and albumin only in PBS.

3.2.5 CONTROLLING PEPTIDE AGGREGATION KINETICS

The mechanism of ordered fibrillar amyloid assembly follows a sigmoidal growth divided into three steps: i) lag phase (nucleation) in which the peptides are mostly in misfolded monomeric form; ii) growth (elongation) phase in which the larger aggregates (misfolded or ordered) form of peptides and iii) final plateau in which grown aggregates (misfolded or ordered) dominate at the final equilibrium.¹⁸⁹ Amyloid forming proteins have hydrophobic domains which can misfold and form non-specific interactions and disordered aggregates with the other hydrophobic molecules in the body. The stability of these aggregates depends on the affinity of each component. Because ordered amyloid assembly of peptides have specific interactions that require a specific conformation, they are often more stable than non-specific hydrophobicity driven misfolded aggregates. However, the same conformational specificity creates an energy barrier. Any aggregation in the intermediate energy level, particularly when it is highly non-specific, impede the

conformational orientation for the ordered assembly and delay the equilibrium in the final plateau of stable fibrils. In another words, misfolding of monomers increases the initial lag and growth phase where the monomeric structures are soluble and less stable.

Albumin, as a flexible hydrophobic protein, aggregates with amyloid forming proteins, elongates the lag phase.^{173–175} The unstable and soluble monomers in the lag phase are mostly able to integrate to the cell membrane and become more toxic.¹⁹⁰ Although the elongated lag time is known to be more toxic, there is no correlation between the lag time, aggregate structures, and cell membrane damage. Since [II] showed amyloid- β characteristics such as highly ordered secondary structure, we hypothesized that albumin can change the aggregation behavior and fibrillar assembly kinetics of [II].¹⁶⁸ Fig. 3.10 shows the kinetics and morphology of [II] aggregates in increasing amount of albumin (0, 0.002, 0.02, 0.05, 0.1, 0.2, 0.5, 1, and 2 w%) in PBS. To distinguish the kinetics of ordered amyloid assembly from misfolded oligomer aggregates, we used Thioflavin T (ThT) and 1,6-diphenyl-1,3,5-hexatriene (DPH) assays, respectively. The morphology and size of the aggregates were studied with AFM and DLS.

ThT is a fluorescent dye, commonly used for β -sheet structure identification.¹⁹¹ The transition from oligomers to fibrils was characterized with ThT in prion protein.¹⁹² Individual peptides prepared in PBS with increasing albumin content and constant ThT, and the fluorescent of ThT was tracked for 4h (Fig. 3.10B). Albumin only groups with different w% were measured with constant ThT as the background, which also showed some degree of intensity as the structures have hydrophobic core but did not increase by time (Fig. 3.11). When mixed, [II] assemble into ordered structures and achieve final equilibrium of fibrillar form in less than 10 min.¹⁶⁸ The final equilibrium where the fibrils

form was only observed in the medium without albumin (0 w%) and 0.002, 0.02, 0.05, and 0.1 w% albumin in 4h (Fig. 3.10B). Similarly, the fibrillar structures were observed in the overnight incubated samples in these parameters with AFM (Fig. 3.10D). The addition of albumin delayed the formation of ordered of amyloid-b by increasing the rate of the lag phase (nucleation) and growth (elongation) phase.¹⁹³ There was also a reduction in the total amount of fibers generated as indicated by ThT fluorescence signals as shown with AFM, and no fibrillar structure was observed for 0.2 and 2w% albumin incubated overnight (Fig. 3.10D).

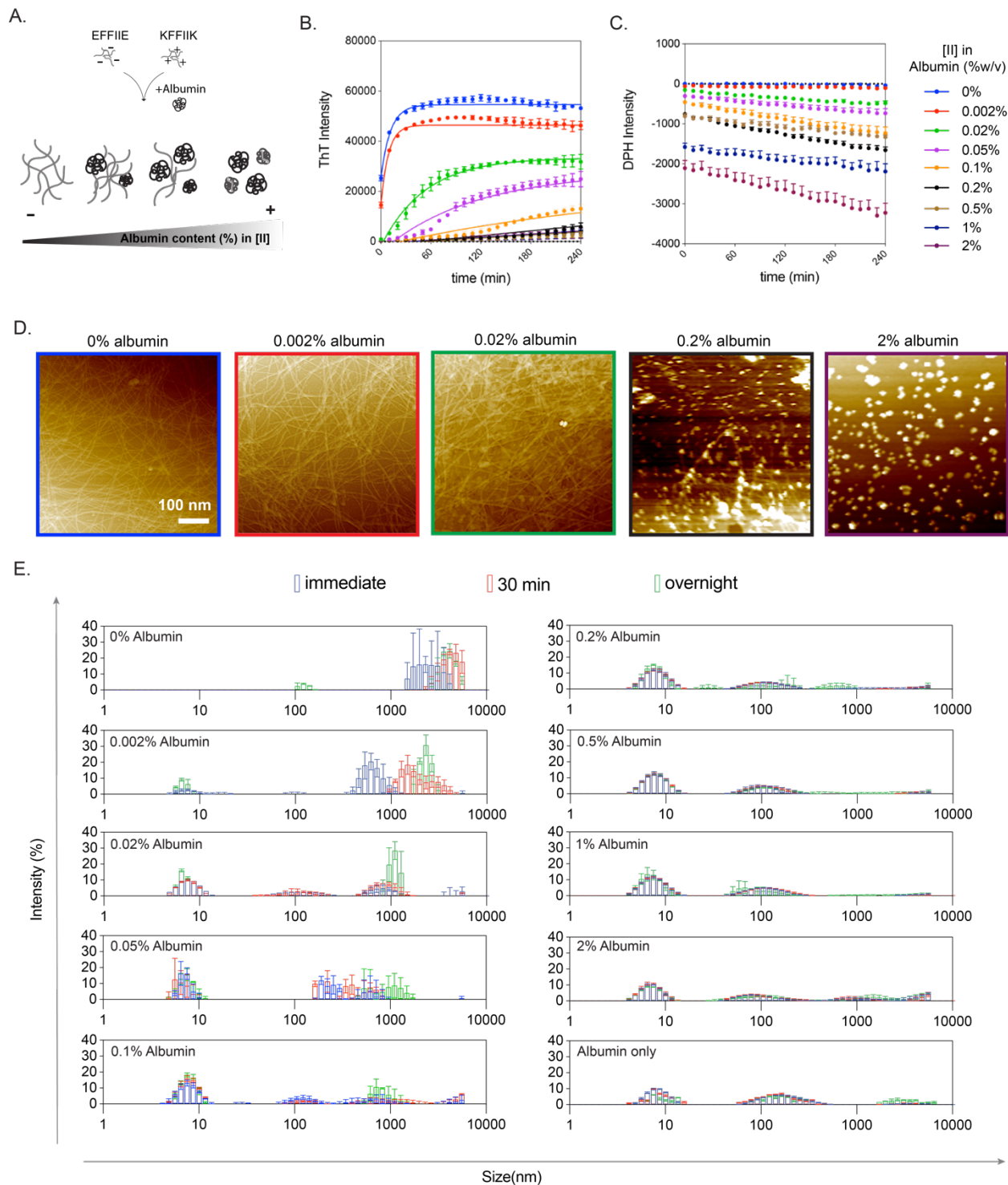


Figure 3. 10 Aggregation kinetics depend on albumin concentration. (A) The schematic of [II] aggregation with albumin. Aggregation kinetics performed with (B) ThT and (C) DPH assays in increasing albumin content. (D) AFM images of [II]-albumin structures (Scale bar = 100 nm). (E) DLS measurements [II]-albumin mixtures.

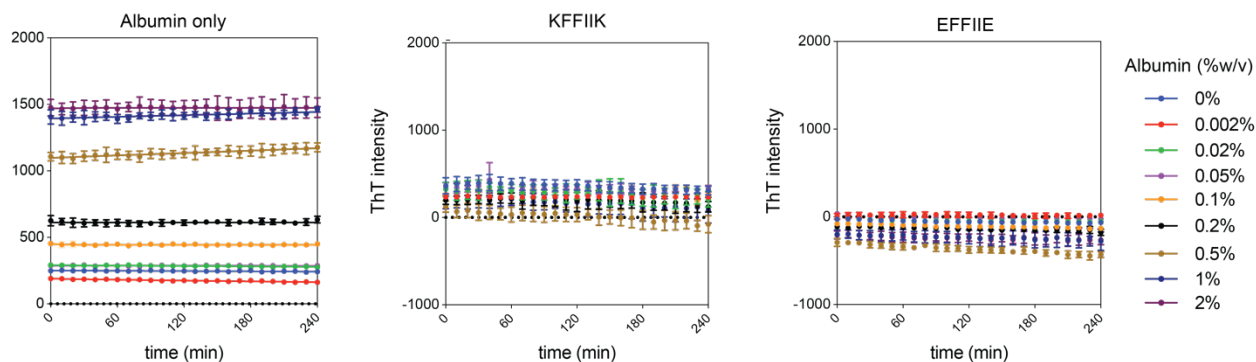


Figure 3. 11 ThT analysis of albumin and individual peptides in different concentrations. Albumin only and peptide counterparts did not give any fluorescence increase respect to time due to non-fibrillar organization.

The formation of disordered structures were identified with DPH assay; a fluorescent dye that has increasing intensity in the hydrophobic environment.¹⁹⁴ Because albumin itself is a hydrophobic protein and form soluble aggregates in PBS, the initial measurements were performed with only DPH and albumin as the background (Fig. 3.12). Individual peptides prepared in PBS, increasing amount of albumin, and constant concentration of DPH, mixed and tracked for 4h (Fig. 3.5C). The decreased intensity of DPH with increasing albumin is interpreted as the decrease the number and sizes of the aggregates. This might be due to the cover of the hydrophobic parts of the albumin with the charged peptides created more soluble and smaller albumin aggregates in PBS. In the PBS with the lowest amount of albumin, 0.002 w%, albumin showed an insignificant intensity, as the structures in this solution are mostly fibrillar, as observed through increasing ThT assay, which indicates that the amount of disorganized aggregates were negligible. Presence of increased albumin concentrations showed slowly lowered intensities, in another words, more change between the intensity of the [II]+peptide complexes

compared to the same amount of albumin alone, is because of formation of smaller aggregates.

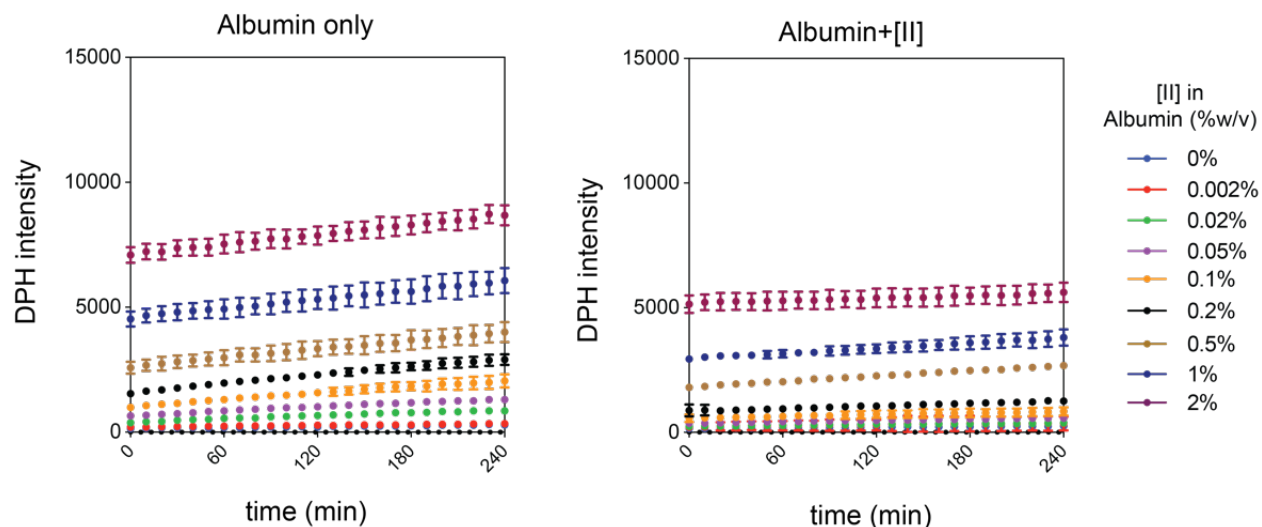


Figure 3.12 DPH analysis of albumin and albumin+[II] in different concentrations. Albumin intensity increased with increased concentration, however [II] disrupted albumin aggregation which leads to decrease in DPH intensity.

While the aggregation of individual peptides did not change with the addition of albumin, several observations of trends are worth to note. When alone, KFFIIK showed slightly higher and stable ThT intensity, which reduced but remained stable by time with increasing albumin (Fig. 3.11). Similarly, the DPH assay showed increasing intensity by time in KFFIIK alone (Fig. 3.13). These measurements were all preformed in PBS in which the charges of the peptides are screened by the salt ions. Therefore, KFFIIK alone shows misfolded aggregation due to the hydrophobic nature of the alkyl tail of Lysine (K). Yet, when KFFIIK is mixed with EFFIIK, the ThT intensity changes immediately and dramatically, indicates that the peptides co-assembling in PBS (Fig. 3.10B). The negative counterpart, EFFIE, in the PBS without albumin, does not aggregate in ordered or disordered manner (Fig. 3.11 and 13). It might be a result of the hydrophobic amino acids'

lower contact probability in the core of EFFIIE compared to KFFIIK and [II].¹⁶⁸ Considering albumin alone also has ThT and DPH intensities due to its hydrophobic nature (Fig. 3.11 and 3.12), the observed negative and consistent intensities of EFFIIE and KFFIIK solutions with increasing albumin indicates formation of smaller and stable aggregates; peptides interact and aggregate with albumin individually. However, when mixed, the increase of ThT intensities, or formation of peptide fibers, indicates that the individual peptide and albumin aggregations are not as favorable as peptide-to-peptide interactions. Addition of the same amount of albumins on the same amount of [II] that is premixed in PBS for 60 min showed stable DPH intensity that were lower than the albumin only (Fig. 3.13, no background subtraction), which might be because albumin falls apart and form non-specific bindings with the fibrillar structures.

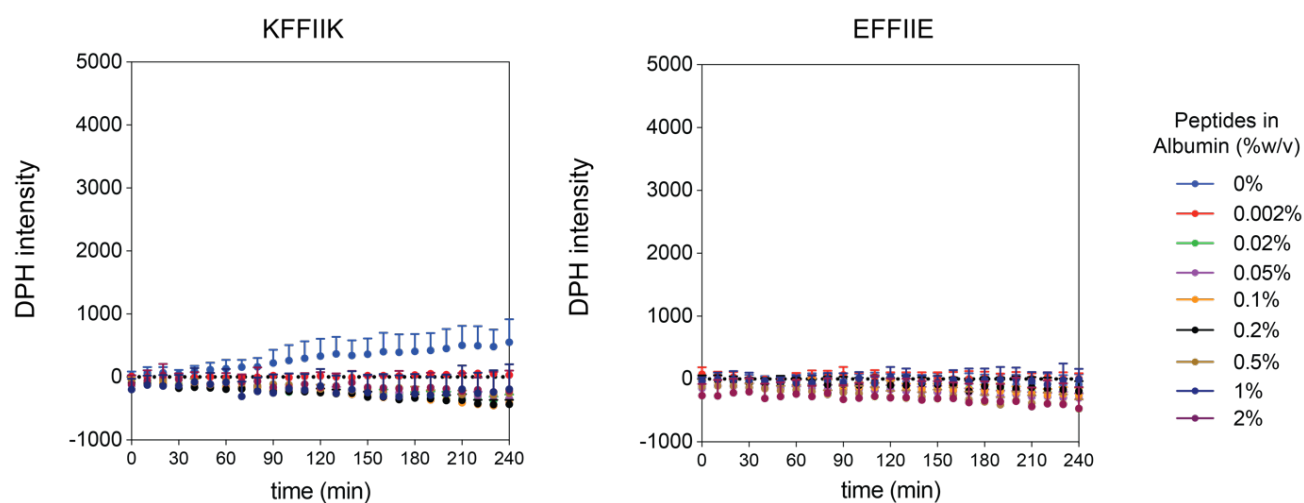


Figure 3. 13 DPH analysis of individual peptides in different albumin concentrations. Individual peptides did not form aggregation.

Size measurements of the aggregates was performed in three different time points; immediately, after 30 min and overnight incubation with DLS (Fig. 3.10E). Without albumin, [II] aggregated immediately with average bigger than 1000 nm structures with a

shift toward higher sizes after 30 min (Fig. 3.10E, 0w% albumin). Similarly, the shift toward bigger structures was observed for the conditions between 0.002 to 0.1w% albumin, which are the conditions where the final fibrillar equilibrium was observed with ThT. After 0.2 w%, size distribution and intensity profiles were almost similar to the 2 w% albumin-only group. The population of structures around 10 nm were higher in the presence of peptides compared to 2 w% albumin-only, indicates smaller aggregates in the presence of peptides, and explains the reduce in intensities observed with DPH. In overall, the observed trend of behavior of [II] with albumin is similar to amyloid; the increasing albumin causes the decrease of the maximum fluorescence intensity, or the total amount of fibrils generated, and increases soluble disordered aggregates; oligomers.

3.2.6 DELAYED AGGREGATION INCREASED THE LIPID MEMBRANE INTEGRATION OF [II]

Among the studied albumin concentrations, 0.2w% showed the threshold for diminishing the ordered fibril formation, therefore the rest of the analyses were performed in 0.2w% albumin. To compare the integration on the lipid membrane of the liposomes, [II] prepared in 0.2w%, incubated for 30 min, then added on the liposomes (Fig. 3.14A). Unlike the premixed [II] in 0w% albumin (Fig. 3.8B), the individual peptides were localized in the liposomes starting from 5 min. Albumin slows down the peptide-peptide interactions by aggregating with the membrane and the interactions of peptides with the lipid membrane is likely to be more stable than their interactions with albumin. Incubation of individual peptides with 0.2w% albumin for 60 min showed that KFFIIK integrates to the lipid bilayer even in 5 min, while the negative one, EFFIIE, does not integrate, which is likely due to the charges of the lipids (Fig. 3.15). The integration of EFFIIE when incubated with albumin and KFFIIK might be because of initial membrane integration of soluble KFFIIK

followed by the aggregation of EFFIIE, even in the lipid interface. These results indicates that without albumin KFFIIK and EFFIIE co-assemble, form fibers, which do not interfere with the integrity of the lipid membrane. In the presence of albumin, the co-assembly process delays due to the aggregation of the individual peptides with albumin. The delay time (lag time or the time require to achieve equilibrium fibril phase) is correlated to the amount of albumin in the solvent.

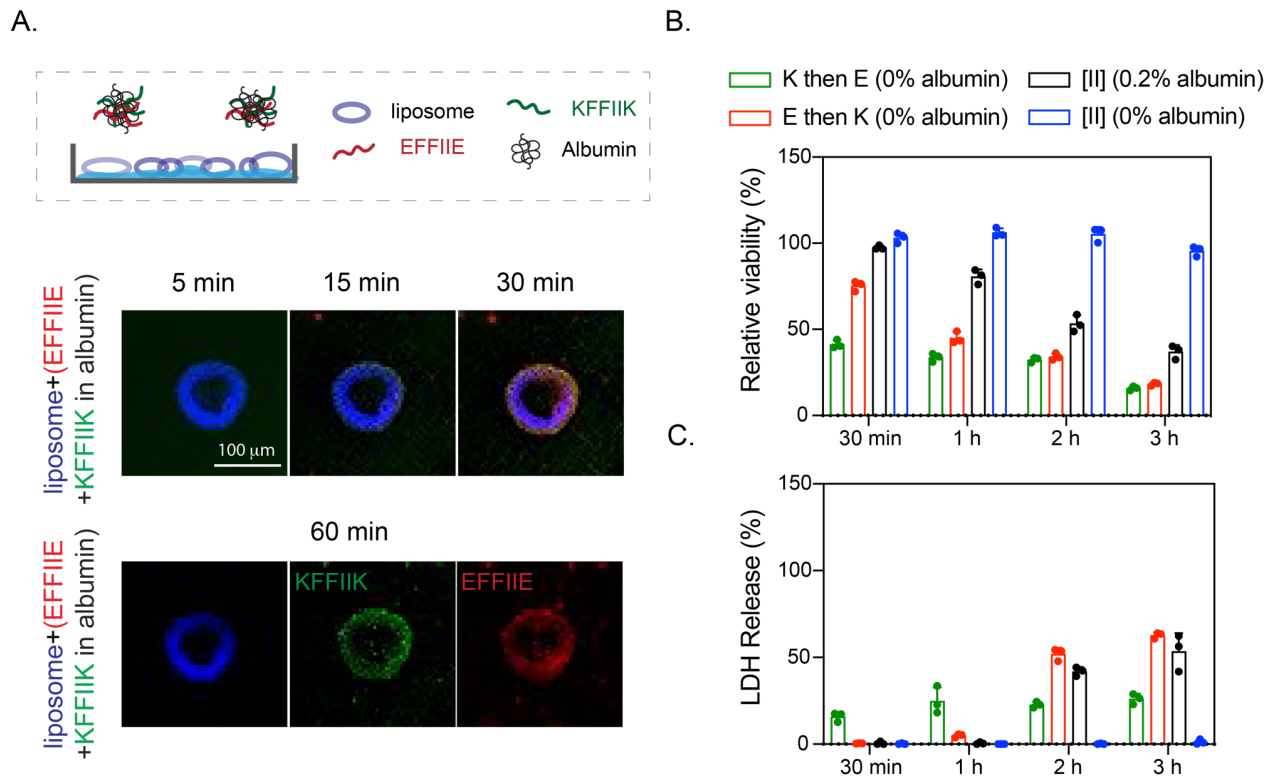


Figure 3. 14 Delayed [II] aggregation increases its integration on the lipid membranes. (A) Liposomal membrane localization of 0.5 mM [II] in 0.2 w% albumin; liposome = blue, EFFIIE = red, KFFIIK = green (Scale bar = 100 μm). (B) Relative viability and (C) LDH release of EMT6 cells treated with individual and aggregates with 0.5 mM [II] in 0 and 0.2 w% of albumin in PBS.

The effect of enhanced lipid membrane accumulation of [II] altered its toxicity (Fig. 3.14B, C). [II] induces immunogenic rupture of mammalian cell membranes, initiates immunogenic cell death in 6h in cell medium supplemented with 10v% FBS (has app.

0.2w% albumin) as shown before.¹⁶⁹ During 3h of treatment, [II] in 0% (without) albumin did not cause any membrane damage (Fig. 3.14B), as [II] fibrils do not interact with the lipid membrane (Fig. 3.8B). Addition of [II] with 0.2w% albumin showed increasing membrane damage over time which is quantified by the release of lactate dehydrogenase (LDH), a cytoplasmic enzyme released upon membrane damage.¹⁹⁵ These results correlate with ThT (high intensity, high ordered fibril assembly) and DPH results (low intensity, high disordered aggregation) indicating that delayed fibril formation increases the membrane damage. Furthermore, we also tested the effects of consecutively introduced peptides to cells without albumin to correlate the toxicity to the membrane integration. When KFFIIK was given first (green bar) followed by EFFIIE addition, cellular viability decreased to 50% at 30 min and reduced to 25% at 3h (Fig. 3.14B). The opposite scenario where EFFIIE added first and then KFFIIK (red bar), started from 75% cell viability at 30 min and decreased to 25% at 3h. As observed from liposomal experiments (Fig. 3.8C, D), KFFIIK accumulated faster on the membrane compared to EFFIIE. Therefore, when peptides were introduced consecutively (30 min), we observed faster cell death in K then E condition. However, cell death was similar at 3h regardless of the addition order (Fig. 3.14B). These results show that the toxicity of [II] can be controlled through control over its aggregation kinetics.

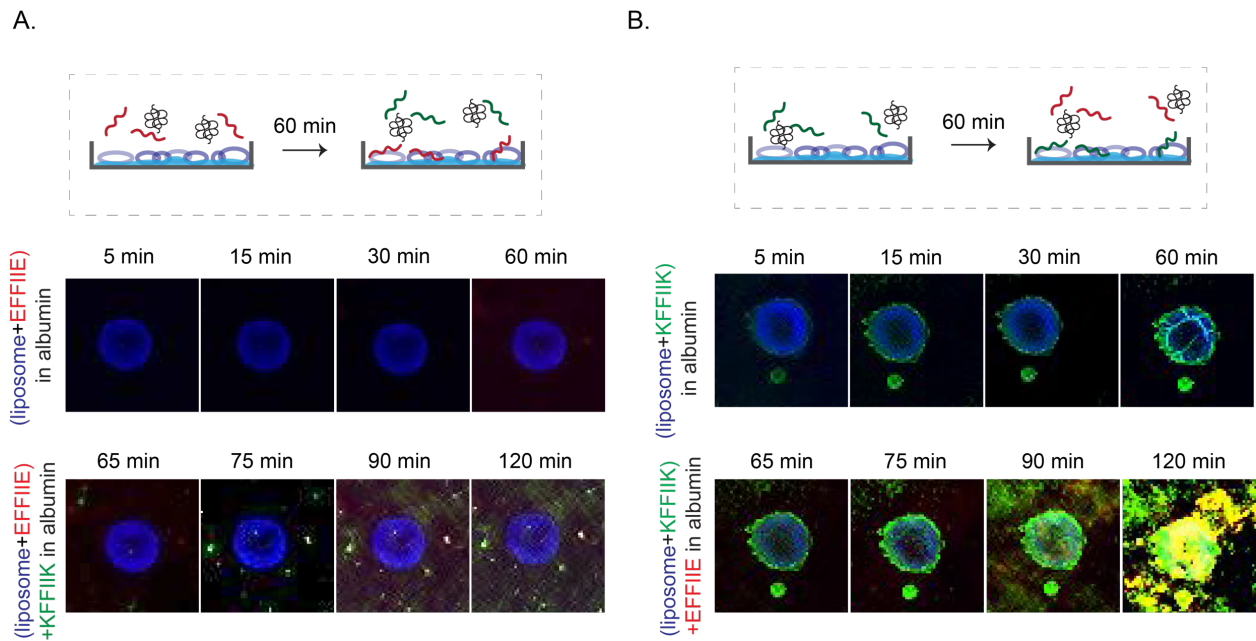


Figure 3. 15 Individual peptide localization on the liposomal membrane. (A) EFFIIE and KFFIIK (B) localization on the liposomal membrane with and without 0.2w% albumin

3.2.7 FRET ANALYSIS FOR ALBUMIN AND [II] INTERACTIONS

FITC and TRITC are fluorescent dyes and FRET couples. When the distance of the two fluorophores is less than 8 nm, the excitation of light with 488 nm wavelength triggers FRET; emission from FITC (donor) at 520 nm excites TRITC (acceptor) that emits light at 578 nm.¹⁹⁶ We used albumin conjugated with TRITC and incubated with FITC-KFFIIK for this analysis. Incubation of FITC-KFFIIK with 0.2w% albumin for 30 min and 24h which did not show FRET, indicates that they are not in proximity (Fig. 3.16A). In the presence of EFFIIE (not fluorescent tagged) also in 0.2w% albumin showed the FRET intensity, TRITC emission at 580 nm and FITC emission at 488 nm was reduced (Fig. 3.16B), indicating the peptides and albumin are aggregated in closer proximity than 8 nm.

The cell membranes were stained with Wheat Germ Agglutinin (WGA) (gray) and incubated with [II] (FITC-KFFIIK (green) and Rhodamine-EFFIIE (red)) in 0.2w% albumin

for 1h and 2h to identify the localization of the peptides. Accumulation of each peptide increased from 1h to 2h with lost integrity of the membrane, which also explained the higher LDH release (Fig. 3.14C). When the peptides were preincubated in the absence of albumin for 30 min, no cell membrane localization was observed (Fig. 3.17), also in line with viability results. Overall, these results demonstrates that in the absence of albumin, peptides assemble into ordered fibrillar structures and do not localize to the cell membrane. Presence of the albumin in the solution prevents immediate peptide-peptide interactions and allows time for peptide aggregation to occur within the cell and at the membrane. Therefore, changing albumin concentration is changing the peptide aggregation kinetics, which results in controllable membrane accumulation and cell death.

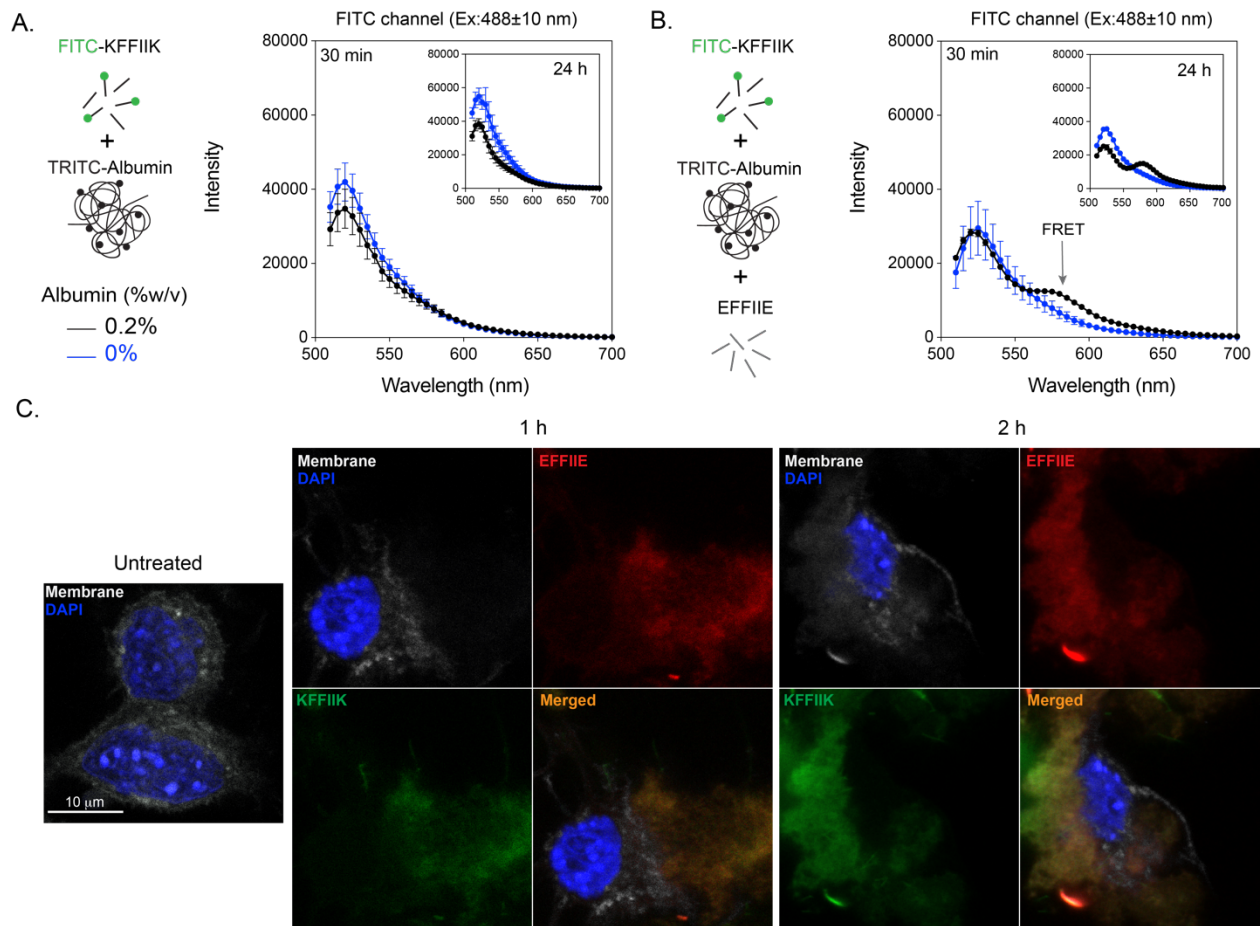


Figure 3. 16 Albumin and [II] interaction. (A) The FRET analysis of the presence and absence of TRITC-albumin with FITC-KFFIIK and (B) with [II]. (C) Confocal analysis of cells treated with 0.5 mM [II] for 30 min, 1h, and 2h in the presence of 0.2 w% albumin. Membrane stained with WGA, gray; cells treated with Rhodamine B labelled EFFIIE, red; FITC labelled KFFIIK, green. (Scale bar = 10 μ m)

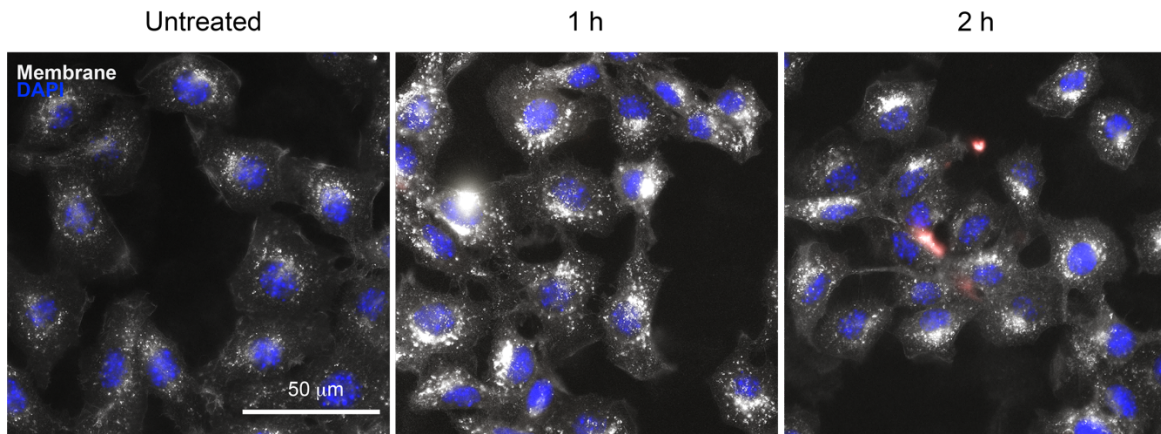


Figure 3. 17 The treatment of cells with preincubated [II] without albumin for 1h and 2h. [II] did not accumulate on the cell membrane due to fibrillar formation.

3.2.8 AGGREGATION OF [II] INDUCES CELL STRESS

The cell plasma membrane senses external stimuli to adapt to changes through intracellular signaling. One of the pathways responding against a variety of external stimuli such as mechanical stress is the Hippo pathway. A β 1-42-mediated neurodegeneration involves the activation of the Hippo pathway.¹⁹⁷ One of the central proteins within the Hippo pathway is YAP. YAP is a transcription factor found in the nucleus in active form and gets inactivated when translocate to the cytoplasm. We treated the cells to analyze the effect of [II] aggregation on YAP localization. At the early time points, 30 min, YAP localized in the cytoplasm (Fig. 3.18A). More specifically, cytoplasmic localization of YAP is mediated by its phosphorylation (Serine 127 (S127)), leading to its inactivation¹⁹⁸ and degradation.¹⁹⁹ Upon administration of [II] with 0.2w% albumin, YAP phosphorylation in the cytoplasm can be observed green at 30 min and 1h (Fig. 3.18B) However, after 1h, phosphorylated YAP in the cytoplasm starts to degrade, which is parallel with YAP localization to the cytoplasm at early time points (30 min). Western blot results also confirmed the phosphorylation of YAP and degradation (Fig. 3.18C). Together

these results show that [II] aggregation is inducing cytoplasmic localization of YAP through its phosphorylation, thus related to the mechanical stress on the cell membrane.

eIF2 α is another factor integrated into the stress response to external stimuli. Under cell stress, eIF2 α gets phosphorylated and initiates the activation of genes responsible for stress response. Phosphorylation of eIF2 α is a consistent marker in a variety of neurodegenerative diseases,²⁰⁰ including AD.²⁰¹ Histological analysis on AD patients showed elevated phosphorylation of eIF2 α .²⁰² Moreover, in in vitro studies, A β 1-42 was shown to induce eIF2 α phosphorylation in human neuroblastoma cells.²⁰³ We analyzed eIF2 α phosphorylation for 0.5mM [II] in 0.2w% albumin and 0.5mM [II] in 0% albumin (non-membrane damaging condition). [II] aggregation-induced eIF2 α phosphorylation at 1h (Fig. 3.18C) followed by rapid degradation due to proteasome activity reported previously.²⁰⁴

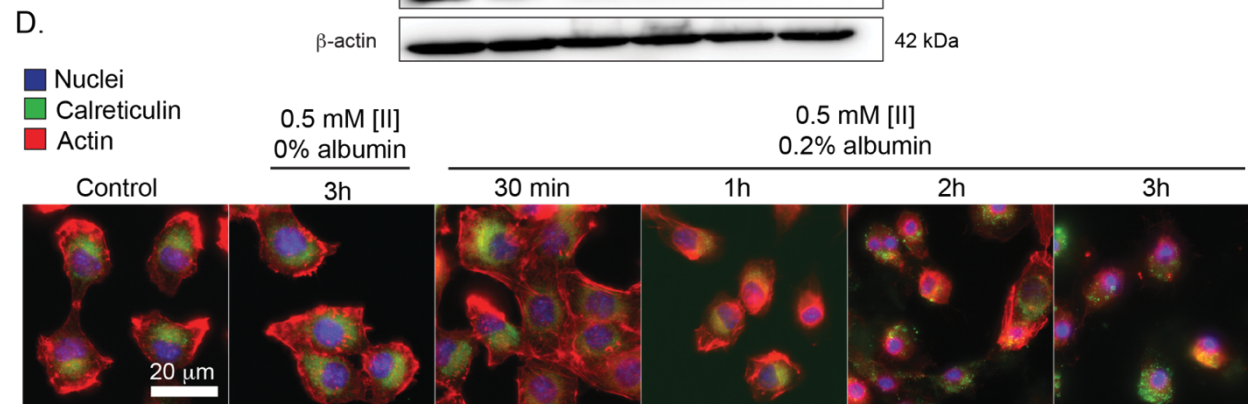
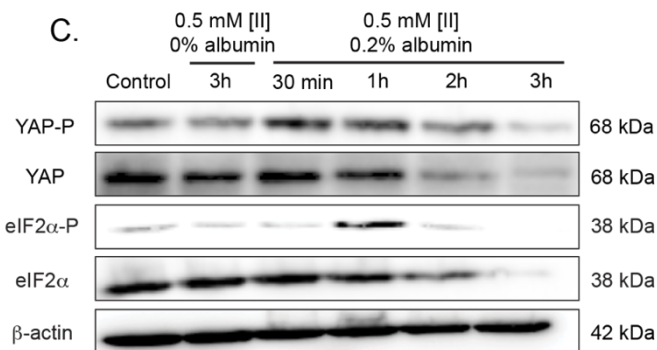
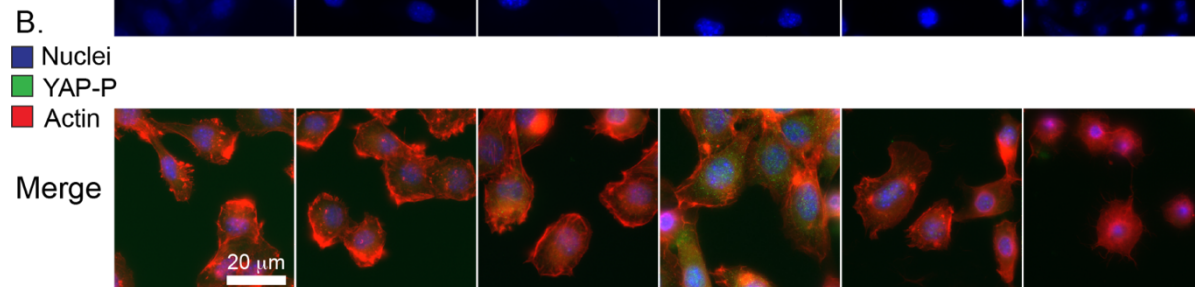
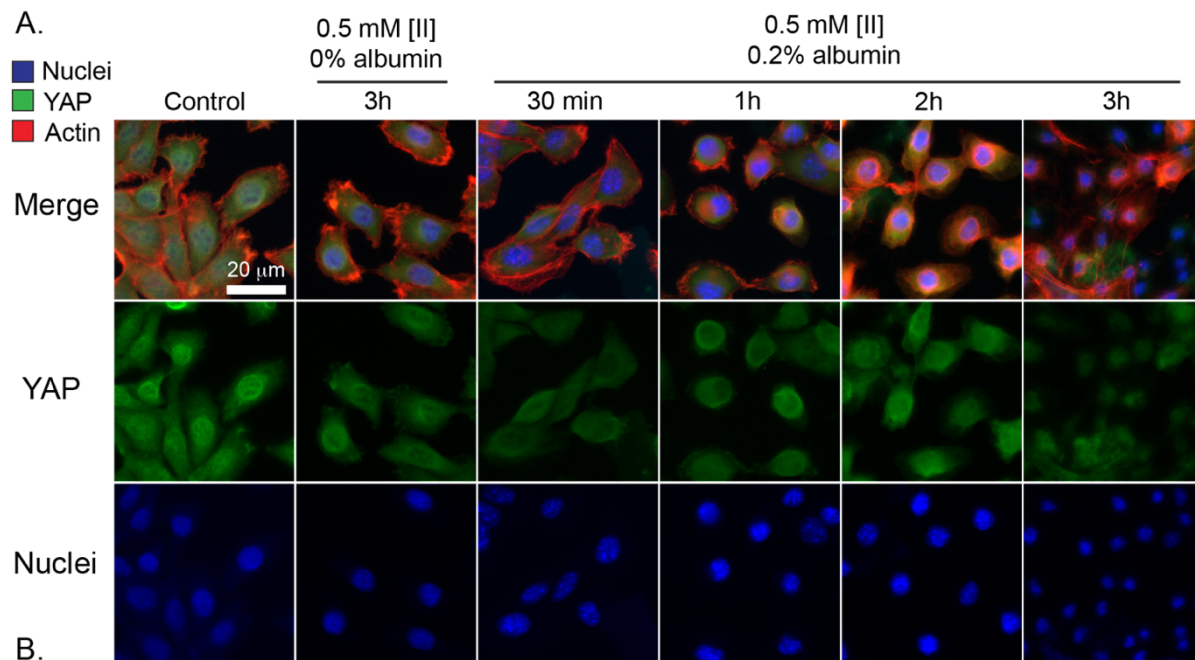


Figure 3. 18 [II] aggregation on the cell membrane induces cell stress. (A) Immunocytochemistry of YAP localization (YAP = green, Actin = red, Nuclei = blue) (B) and phosphorylation based on aggregation (YAP-P = green). (C) Western blot analysis of YAP, YAP phosphorylation, eIF2 α and eIF2 α phosphorylation in different time points β -actin was used as an internal loading control. (D) Immunocytochemistry of calreticulin cell surface localization (calreticulin = green, Actin = red, Nuclei = blue). (Scale bars = 20 μ m)

3.3 CONCLUSIONS

First, we designed peptide sequences to cause cell membrane damage by mimicking A β protein. CoOP strategy is based on a framework (i.e., the diphenylalanine (FF) domain and terminal charges) that defines the peptide-peptide orientation and thus initiates the interactions of the peptides. However, the forces that affect the kinetics of the assembly and the properties of the final product are provided by the two amino acids of the substitution domain which is the hydrophobic domain that we changed with different amino acids such as VV, LL, WW and II. Our CoOP strategy provides a quantitative correlations between changes in the amino acid sequence of the framework and the properties of the assembly¹⁶⁸. Hence, CoOP represents a uniquely powerful strategy to create small peptides with controllable aggregation profiles that can be used to design peptide-aggregation-induced cell membrane.

Second, we show that [II] aggregation induces cell membrane damage and engages cell stress markers as in a variety of neurodegenerative disorders. Furthermore, we showed that this aggregation can be controlled by using albumin. [II] aggregation-induced the phosphorylation of eIF2 α and calreticulin surface localization, which highlighted ICD. Overall, the modulation of peptide aggregation presented here, allows us to control cell membrane damage and offers us to modulate immunogenic cell death.

Protein and peptide aggregation is a phenomenon that can be seen in both pathogenic conditions and during developmental stages of amyloid proteins.^{157,158} Oligomeric species form transiently during the aggregation process and not only act as essential intermediates but also represent major pathogenic agents in disorders.¹⁵⁹ However, the transient and complex structures and aggregates of oligomers create confusing results and challenge in drug development.¹⁶⁴ In this study, we showed an engineered peptide complex via CoOP strategy as a synthetic and simple tool to study the amyloid aggregation mechanism into ordered assemblies (fibrils) and disordered aggregates (oligomers) with the presence of albumin, and correlate it to its toxicity. Importantly, we showed that, albumin can control the aggregation kinetics of [II], which induce mechanical stress on the cells and ICD. The immune response against ICD is potent. Controlling ICD means control over the immune response and progress of amyloidosis-related diseases. Overall, [II] offers a unique engineered platform to study aggregation kinetics of amyloidosis. The simplicity of [II] as an engineered tool allowed the detailed characterization of disorganized structures to fibril aggregation kinetics and the effects of each step on cell. Studies with [II] can serve to establish clear and direct results for drug development with amyloidosis.

3.4 MATERIALS AND METHODS

Peptide synthesis. KFFWWK and EFFWWE were purchased from Biomatik (Biomatik Corporation, Canada). KFFIIK, EFFIIE, KFFLLK, EFFLLE, KFFVVK and EFFVVE peptides were synthesized via solid phase peptide synthesis with PreludeX automatic peptide synthesizer (Protein Technologies, Inc., Tucson, AZ). They were prepared on a

0.25 scale by repeated amino acid couplings using Fmoc protected amino acid (3 eq. 1mL), DIC (7.5 eq. 1mL) and Oxyma (7.5 eq. 1mL). MBHA Rink Amide resin (High-Loaded, Gyros Protein Technologies) was used as solid support to construct the peptides. Fmoc protected amino acids (Gyros Protein Technologies) were removed through treatment with 20% piperidine/DMF solution for 45 min (three times for 15 min) at 80°C. All the peptide conjugation was performed for 2h at 80°C and acetylated with a treatment with 10% acetonitrile/DMF solution for 15 min twice. Cleavage of the peptides from resin and deprotection of acid labile protected amino acids were carried out with a mixture of TFA/ TIS/ water in a ratio of 95:2.5:2.5 for 3h at room temperature. Excess TFA and organic solvents were removed by evaporation and the remaining peptide was precipitated using diethyl ether at -80°C by using 1:4 volume ratio and stayed overnight. After precipitation, peptides in ether solutions were centrifuged at 8000 rpm for 15 min. Peptide precipitates were collected and ether was removed. The centrifuged white peptide precipitate was dissolved in either (0.1% formic acid in water for KFFIIK peptide) or (0.1% ammonium hydroxide in water for EFFIIE peptide). Peptides were purified with preparative HPLC (Agilent 1260) with Agilent ZORBAX 300 SB-C18 (9.4 x 250 mm) column with a mobile phase of water/acetonitrile mixture (0.1% ammonium hydroxide) used for negatively charged peptides; water/acetonitrile mixture (0.1% formic acid) was used for positively charged peptides. All peptides were tested with a purity >95%. HPLC run started with 100% water for 3 min, followed by a gradient increase in acetonitrile from 0% to 100% over 25 min, followed 100% acetonitrile for 3 min, and ended with 100% for 2 min. The flow rate is 2 mL/min and injection volumes are 10 µL.

Critical Aggregation Determination and Congo Red analysis. All peptide aggregation analyses were performed in PBS. DPH assay was performed to understand the CAC. Peptides (except [AA]) were prepared in PBS starting from a concentration of 500 μM to 3.9 μM with serial dilution. [AA] was prepared from 10 mM to 15.6 μM to check the aggregation behavior even in higher concentrations. First, negatively charged peptide (48 μL) was put to the black 96 well- plate, then 4 μL (from 4 μM in PBS) DPH was added, and finally, positively charged peptide (48 μL) was added to each well. The solutions were incubated at 37 °C for an hour. After the incubation, fluorescence intensity was collected immediately with Ex:360 \pm 40 nm, Em: 460 \pm 40 nm with BioTek Neo2SM microplate reader. We performed a Congo Red assay to visualize aggregations deposited on the well plate. Peptides having 0.5 mM concentration and equal volume (48 μL each) were prepared in PBS. Then first, negatively charged peptide was put to 96 well-plate. Congo red having a final concentration of 20 μM (4 μL), was added, followed by the addition of a positively charged peptide (48 μL each). Brightfield images were taken immediately with Keyence bz-x710 microscope at defined time points.

TEM analysis. Peptide samples were prepared from 10 mM stock solutions (incubated for 24h) of co-assembled samples to 0.02 mM with water. Then, 10 μL of diluted peptide samples were dropped onto the TEM grid (Ted Pella, Catalog number:01813-F) and incubated for 10 min. Then, samples were taken with a pipette, negatively stained with 2% uranyl acetate and imaged using JEOL 2010F Field Emission Transmission Electron Microscope.

Liposome formation and imaging. Giant liposomes were formed based on previously published data with simple modifications.¹⁸⁷ First, agarose (UltraPure Agarose,

ThermoFisher Scientific) was prepared with 1%w/v in water and boiled in a microwave oven until all agarose powder was dissolved. Then, it was poured down into a petri dish to cool down at room temperature to form a gel for 2-3h. Before coating the glass slides, agarose gel was melted in a microwave until all gel turned into a solution. One side of glass slides was dipped into agarose solution and excess solution was removed. After coating, glass slides were placed on a hotplate (37°C) and waited for 1-2h until an agarose film was formed on top of the glass slides. For making liposomes, DPPC (1,2-dipalmitoyl-sn-glycero-3-phosphocholine, Avanti Polar Lipids, Inc.) was used with cholesterol (Sigma-Aldrich). At first, DPPC was prepared in 2 mM in chloroform, and cholesterol was prepared in 400 mM in chloroform. Both of the solutions were mixed with equal volume (1 mL each) to have 5:1 molar ratio (DPPC:cholesterol). For staining the liposomes with DiR (1,1'-Dioctadecyl-3,3',3'-Tetra methylindotricarbocyanine Iodide) dye, 4 mL of DiR (1 mM in chloroform) was mixed with 2 mL DPPC:cholesterol. Then, 50 mL of labeled liposomes was dropped onto agarose-covered glass slides and spread out homogeneously by rolling a glass rod. Then, slides were placed in a vacuum chamber for 30 min. After removing from the vacuum chamber, slides were placed in a clean petri dish and 1xPBS was added from the side of the petri dish to allow hydration and swelling of liposomes for 3h. For peptide-membrane localization assay, FITC labeled KFFIIK and Rhodamine-B labeled EFFIIE peptides (Biomatik Corporation) were used. KFFIIK and EFFIIE were first solubilized in 10 mM as a stock solution in water, which was diluted to 0.5 mM with 1x PBS. The fluorescent portion consisted of 1:100 molar ratio. For example, FITC-KFFIIK was 50 mM in 0.5 mM KFFIIK peptide as a final concentration. After liposome formation, 0.5 mM of fluorescent labeled one peptide counterpart (200 mL) were

incubated with liposomes for 60 min, then oppositely charged 0.5 mM of fluorescent labeled peptide (200 mL) was added and incubated for another 60 min. The imaging was performed with Keyence BZ-X800 with BZ-X filter Cy7 (DiR labeled liposome), BZ-X filter GFP (FITC-KFFIIK), and BZ-X filter mCherry (Rho-EFFIIE).

Assembly and aggregation kinetics determination. Thioflavin T (ThT) (Sigma-Aldrich) and 1,6-Diphenyl-1,3,5-hexatriene (DPH) (Sigma-Aldrich) were used to understand the kinetics involved in ordered assembly and aggregation kinetics. Both fluorescence measurements included albumin (bovine serum albumin, Sigma-Aldrich) with different concentrations indicated based on weight/volume% (w%) and without albumin (in 1x PBS). At first, fresh albumin (40mg/mL, 4 w%) was dissolved in 1x PBS and diluted into 2, 1, 0.5, 0.2, 0.1, 0.05, 0.02, 0.002 w% in 1x PBS. Then, stock peptides (10 mM in water) were diluted (0.5 mM) in different albumin concentrations, individually. For ThT measurements, 5 mL from 400 mM ThT in PBS was added to 195 mL of 0.5 mM KFFIIK and EFFIIE (either in different albumin concentrations or in 1x PBS), individually. Then, each peptide in the same albumin concentration was mixed and read with BioTek Neo2SM microplate reader for 4 h with 10 min intervals (Ex: 440, Em:480 with gain:90). For DPH analysis, stock DPH (1 mM in water) was diluted to 80 mM working concentration in 1x PBS. Similar to ThT assay, 5 mL from 80 mM DPH in 1x PBS was added to 195 mL of 0.5 mM KFFIIK and EFFIIE (in different albumin concentrations for in 1x PBS), individually. Then, each peptide in the same albumin concentration was mixed and read with BioTek Neo2SM microplate reader for 4h with 10 min intervals (Ex: 360, Em:450 with gain:100). Albumin with different concentrations (without any peptide) was also analyzed for both of the assays and subtracted from [II]+Albumin data. For [II] in 0w% albumin, 1x

PBS (with ThT or DPH) was used as a background for subtraction. For ThT analysis, relative intensity values were calculated within each group. Data fitting was applied with a one-phase association to calculate half-time in ordered assembly kinetics by using GraphPad Prism 9.3.0.

AFM analysis. Morphological characterization of [II] was performed with AFM (NX-10 Park Systems Corp) with a non-contact mode by using cantilever probe (OMCL-AC160TS 5M). Peptide were prepared by either with albumin (0.002 w%, 0.02 w%, 0.2 w%, 2 w%) or without albumin (0 w%) in PBS. At first, 0.5 mM KFFIIK (50 μ L) was prepared with or without albumin and 0.5 mM EFFIIE (50 μ L) was prepared with or without albumin in PBS. Then, two oppositely charged peptides were mixed and incubated overnight (~ 20h). For sample preparation, mixed samples were diluted to 0.1 mM with water and 20 μ L dropped onto silicon wafer. Prepared samples were dried at room temperature and imaged with a 1 kHz scanning frequency. Data points were taken in a 256 x 256 grid over 5 μ m–by–5 μ m area.

Dynamic Light scattering (DLS). Hydrodynamic size and ζ potential of single and mixed peptides were measured by DLS.²⁰⁵ For particle size analysis, intensity of scattered light was measured under Brownian motion and hydrodynamic radius, R_h , was calculated by using stokes- Einstein equation (Eq. 1):

$$R_h = kT / (6\pi\eta D_t)$$

where k is the Boltzmann's constant, T is temperature in K (298 K) and η is the solvent viscosity. Diameter that measures in DLS is value that refers to diffusion of the particle.

A ZetaSizer Nano ZS (Malvern, UK) instrument with a detector angle of 173° in a

backscatter mode was used for analysis. Clear disposable cell cuvettes were first washed three times with 0.22- μm filtered deionized water (resistance of 18.2 megohm $\cdot\text{cm}$). Before measurements, peptide solutions in phosphate-buffered saline were also filtered with a 0.22- μm filter to avoid any dust that can alter the measurements. For individual peptides, 500 μM (500 μl) positively and negatively charged peptides were used in PBS. For [II], equimolar (500 μM , 250 μl) of KFFIIK and, equimolar (500 μM , 250 μl) EFFIIE were mixed analyzed immediately, at 30 min and overnight (~ 20 h). For [II] with albumin samples, individual peptides (500 μM each) were prepared in albumin solution (0.002, 0.02, 0.05, 0.1, 0.2, 0.5, 1, or 2 w% albumin in PBS) individually and mixed with equal volume (250 μL each). Then analyzed immediately, at 30 min and overnight (~ 20 h). ζ potential measurements were performed at 30 min.

FRET analysis. FITC and TRITC could act as the donor and acceptor of a FRET pair, respectively.¹⁹⁶ FITC-KFFIIK peptide was prepared as 500 mM (1:50 FITC-KFFIIK:KFFIIK molar ratio) and albumin was prepared as 2 w% (20 mg/mL, 300 mM) mixed with TRITC-albumin as 1:100 molar ratio. EFFIIE peptide was prepared as 500 mM. For a group consisting of FITC-KFFIIK and TRITC-albumin, 50 mL of FITC-KFFIIK was mixed 10 mL TRITC-albumin and 50 mL of PBS was added to have a final volume 110 mL. For 0w% albumin, 50 mL of FITC-KFFIIK was mixed with 60 mL of PBS. [II] was prepared as follows. For 0.2 w% albumin. 50 mL of FITC-KFFIIK was mixed with 50 mL of EFFIIE and 10 mL of TRITC-albumin was added to have a final volume 110 mL. For 0% albumin, 50 mL of FITC-KFFIIK was mixed with 50 mL of EFFIIE and 10 mL of PBS was added. These mixtures were incubated for 30 min and 24h at room temperature and subjected to

fluorescence measurements with an excitation of 488 nm for FITC as donor and scan between the emission of 500 and 700 nm for TRITC as acceptor.

Cell Culture. EMT6 cells were cultured in Roswell Park Memorial Institute (RPMI) 1640 Medium, supplemented with 10% FBS (Hyclone SH30910.03) and 1% antibiotics; penicillin (100 U/mL), and streptomycin (100 mg/mL) (Thermo Fisher 15240062) according to the manufacturer's instructions. Cells were cultured in a humidified incubator at 37°C supplied with 5% CO₂. T75 flasks (TPP 90076) were used for culturing and cells were passaged upon 85% confluency by using trypsin (Sigma 59418C). Cell culture media was changed every 2 days.

Peptide preparation for in vitro experiments. [II] peptides were prepared in either 0.2 w% albumin or 0 w% albumin for in vitro conditions. First, albumin was prepared as a stock solution in 2 w% (20 mg in 1 mL the RPMI medium). Then, was diluted 1:10 to reach 0.2 w% in the RPMI medium. The prepared KFFIIK and EFFIIE stock peptides (10 mM in water) were diluted to 0.5 mM separately into 0.2 w% albumin/medium. For 0 w% albumin condition, KFFIIK and EFFIIE stock peptides 10 mM in water) were diluted to 0.5 mM separately into albumin/medium. For 96 well plate, each well consisted of 100 mL of peptide having 50 mL EFFIIE and 50 mL KFFIIK in either only RPMI medium (0 w% albumin) or 0.2 w% albumin in RPMI medium.

Viability assay. Cells were seeded onto 96 well plates and left for O/N attachment. The next day, media was removed and treatments were carried out. Viability was measured with Cell Titer Glo 2.0 solution (Promega G9248). The luminescent signal was measured in accordance with the manufacturer's instructions. Measurements were carried out with

BioTek Neo2SM microplate reader and relative viability was calculated by using untreated control group. Live-Dead assay was carried out using Viability/Cytotoxicity Assay kit (BIOTIUM 30002). After peptide treatment, cells were treated with calcein and ethidium homodimer in accordance with the manufacturer's instructions. Fluorescent images were taken by using Keyence bz-x710 microscope.

LDH Release. LDH release was measured with Cytoscan-LDH Cytotoxicity Assay (G-BIOSCIENCES 786-210). Briefly, at the end the treatments, collected supernatants were mixed with reaction mixture and incubated for 20 min at 37°C. Reaction was stopped with stop solution, and absorbance was measured at 490 nm and 680 nm. Triton-X treatment is used as a 100% LDH release control. Absorbance at 680 nm is used as the background signal and values were subtracted from absorbance values at 490 nm. Measurements were carried out with BioTek Neo2SM microplate reader and relative LDH release was quantified based on the positive control for LDH release (maximum LDH release through Triton-X treatment).

Immunocytochemistry. Phalloidin staining OVCAR-8 cells were seeded on glass coverslips in a 24 well plate. Cells were treated with [II] for 1-3 and 6h. After each treatment period, cells were washed with 1X PBS and fixed with 4% PFA for 20 min, then, stained for 30 min with Phalloidin-iFluor 555 (Abcam ab176756) in 1% BSA. After the staining coverslips were mounted in ProLong Glass Antifade Mountant with NucBlue Stain (Thermo Fisher P36981) and stored in the dark until imaging.

Confocal Imaging. EMT6 cells were seeded on glass coverslips in a 24 well plate and incubated overnight for attachment. Prior to the experiment, cells were labeled with WGA

633 membrane stain (ThermoFisher W21404) accordingly with the manufacturer's instructions. After membrane staining, cells were washed 2x with PBS and treated in the presence (0.2 w%) and absence (0 w%) of albumin.

Immunoblotting, Reagents. Acrylamide/Bis-acrylamide, 30% solution (Sigma A3699), 1.5 M Tris-HCl, pH 8.8 (Teknova T1588), Tris HCl Buffer 0.5 M solution, sterile pH 6.8 (Bio Basic SD8122), Ammonium persulfate (Sigma A3678), UltraPure 10% SDS (Invitrogen 15553-027), TEMED (Thermo Fisher Scientific 17919), Dithiothreitol (DTT) (BIO-RAD 1610610) Tris Base (Fisher Bioreagents BP152), Glycine (Fisher Bioreagents BP381), 4x Laemmli sample buffer (BIO-RAD 1610747), TWEEN 20 (Sigma P9416), Mini Trans-Blot filter paper (BIO-RAD 1703932), Nitrocellulose Membranes 0.45 mm (BIO-RAD 1620115), EveryBlot Blocking Buffer (BIO-RAD 12010020), Clarity Western ECL Substrate (BIO-RAD 170-5060).

Procedure. Samples were prepared in Laemmli buffer and boiled for 8 min at 96°C. Then, proteins were separated with sodium dodecyl sulfate-polyacrylamide gel electrophoresis (SDS-PAGE) gels (8.5% and 15%) and transferred to nitrocellulose membranes (45 mm). After transfer, the membranes were blocked EverBlot Blocking Buffer and washed with Tris Buffered Saline with 0.1% Tween 20 (TBST). Blots were incubated with Phospho-YAP (Ser127) (Cell Signaling 13008), YAP (Cell Signaling 4912), Phospho-eIF2a (S51) (Cell Signaling 9721), eIF2a (Cell Signaling 9722) overnight. The next day blots were washed and incubated with Goat anti rabbit secondary antibody (Invitrogen 31460) and imaged with Clarity Western ECL substrate (BIO RAD 170-5060). b-actin (Santa Cruz sc-47778 HRP) was used as an internal loading control. Blots were imaged by using Azure c600.

Immunocytochemistry. EMT6 cells were seeded on glass coverslips in a 24 well plate and incubated overnight for attachment. After indicated treatments, samples were washed with 1X PBS, and fixed with 4% PFA for 20 min. Then, Triton-X (0.5%) was used to permeabilize the cells for 20 min on shaker. Samples were blocked with 3% BSA for 1h on shaker, washed 3 times with 1X PBS and incubated with the following antibodies Phospho-YAP (S127) (Cell Signaling 13008), YAP (Cell Signaling 4912) or calreticulin (Cell Signaling D3E6) overnight on shaker on ice. The next day samples were washed and incubated for 1h on shaker with DyLight™ 488 Donkey anti-rabbit IgG (minimal x-reactivity) Antibody (BioLegend 406404). After the incubation period, samples were washed and incubated with Flash Phalloidin™ Red 594 (BioLegend 424203) for 30 min on shaker. Lastly, samples were washed and mounted in ProLong™ Glass Antifade Mountant with NucBlue™ Stain (Thermo Fisher P36981) and stored in the dark until imaging.

CHAPTER 4. MODULATING PEPTIDE AGGREGATION

KINETICS

Manuscripts in preparation:

From: Gunay, G.[#], Hamsici[#], S., & Acar, H. (2022). Peptide Aggregation kinetics modulates immunological cell death [#]Contributed equally

The formation of heterogenous mixtures of peptide aggregates is closely related to neurodegenerative diseases like Alzheimer's disease. Structural rearrangements during aggregation are important because they affect the kinetics of toxic globular aggregates. However, the heterogeneity of structures and the dynamic process make the identification of this process extremely difficult. Here, we designed a co-assembled peptide aggregation model to study the structure-property and toxicity of amyloid-like structure. This strategy offers a simple and controllable aggregation model which mimics the cell membrane damaging functionality of amyloid forming proteins. We utilized the controllable aggregation model to develop two vaccination strategies: antigen-specific antibody production against model antigen ovalbumin and prophylactic tumor vaccine application. Overall, control over aggregation kinetics and structure provided modulation of immune system.

4.1 INTRODUCTION

A wide variety of human disorders are characterized by the formation of supramolecular aggregates.²⁰⁶ For instance, more than 30 human proteins, including transthyretin (TTR), islet amyloid polypeptide (IAPP), α -synuclein, and amyloid-beta ($A\beta$), contribute to a variety of degenerative disorders by misfolding and/or misassembling into different aggregate structures.²⁰⁷ It is still unclear how the disease is brought on and how aggregation occurs structurally and molecularly since no probes can track the various aggregate types created or structures produced during this dynamic process.⁶⁵ Also, the variety of intermediate structures produced by different nucleation processes makes it more challenging to isolate and accurately predict the toxic agents causing amyloid disease.⁶⁶ However, according to the latest hypothesis, which is called toxic oligomer hypothesis, the smaller diffusible oligomers, which display a variety of structural variations, rather than the insoluble cross- β -sheet amyloid fibrils, are the cause of degenerative effects.²⁰⁸ Therefore, it is important to analyze oligomeric structures during the aggregation pathway to understand the relationship between oligomers and toxicity.

It is widely accepted that amyloid fibrillization is a nucleated polymerization phenomenon because the kinetics of fibril formation is mostly sigmoidal.¹⁶⁵ According to this model, there are three distinct steps which are the lag phase, nucleation or elongation phase and plateau phase.¹⁶⁵ Through hydrophobic and aromatic interactions, a hydrophobic core - also known as the amyloidogenic core, form and self-associate with another peptide during the lag phase.²⁰⁹ Monomers and oligomers above their critical concentration, combine to form protofibrils, yielding the final, highly ordered β -sheet structures.¹⁶⁵ In general, the formation of oligomeric aggregation nuclei (nucleation) is considered a key

event in the onset of protein aggregation and often the rate-limiting step of fibril growth.²¹⁰ For the nucleation step, intermolecular hydrophobic interactions are among the key determinants of the rate and extent of the hydrophobic collapse of the misfolded monomers into oligomers, along with A β concentration, medium temperature, and polarity.^{67,210} The critical determinants of the propensity of proteins to form amyloid structures varies with amino acid mutations within the sequence,²¹¹ external stimuli such as the addition of ions²¹² or chaperons like albumin.²¹³ These determinants affect the kinetics of fibrilization, and so the toxicity of the amyloids. The experimental understanding of the kinetics landscape of any amyloid structure can be determined by the fluorescent intensity change of Thioflavin T (ThT, a fluorescent marker for amyloid structure, more explanation is in Section 1.3.1) by time. The information collected from the amyloid fibrilization kinetics of samples with different determinants was combined in a mathematical model to identify the affected parameters^{63,189}.

The determination of the kinetics landscape parameters can be identified by fitting the model to the collected ThT data of the amyloid samples in different concentrations.²¹⁴ This approach is applicable when the aggregation mechanism follows a sigmoidal curve, having a lag time. In other words, if the sample form a detectable amount of pre-fibrilization seeds or oligomers.⁹⁰ However, when the fibrilization of the protein is exponential, no lag time was observed.⁶³ The possible reason is increased hydrophobicity overcome the nucleation process due to exceeding the kinetic barrier of the lag phase formation. Another study showed the importance of concentration-based aggregation mechanism of a small peptide, FGAIL, forming amyloid-like structures.¹⁶⁵ These studies revealed that the concentration and the size of the peptides are also affective in slowing

aggregation, extending the lag time, and stabilizing the population of oligomers, which all steps of the free energy change of monomers to fibril formation.¹⁶⁵ If oligomeric intermediates refold into amyloid fibrils, a free energy for "oligomer activation" was met.¹⁶⁵

Proteins that are in the unfolded oligomeric state interact with the cell membrane in a higher level. The hydrophobic residues that are typically in the core of the folded proteins become dispersed on the surface of unfolded oligomer proteins. These hydrophobic residues facilitate the adherence and penetration of the unfolded peptides into the plasma membrane. Cell membrane interactions of the early oligomers are causing lipid membrane disruption and initiating essential cellular functions.²¹⁵ For example, A β 42 (which has additional I and A) is more hydrophobic and more cytotoxic than A β 40 isoform.²¹⁶ Furthermore, the size of the oligomers is another parameter showing the membrane localization and penetration; the decrease in size of the oligomers has known increase effect on the cytotoxicity, due to the enhanced binding capability of small oligomers to the membrane.²¹⁷ The accumulation of the amyloid-structures on the plasma membrane create damage which results in an inflammatory response and causes chronic activation of innate-immune systems by releasing damage-associated molecular patterns (DAMPs).^{218,219}

Despite the evidenced importance of understanding the structure-property relationship of the amyloid-forming cytotoxic peptides for understanding the mechanism and progression of the disease, the dynamic process of amyloid aggregation and heterogeneity limits the studies related to oligomer-based cytotoxicity. To understand the relationship of structure-property of amyloidogenic oligomers: i. samples were taken in different times of the fibrilization,²²⁰ ii. aggregation was stopped by using various inhibitors,²²¹ iii. oligomers

were isolated based on their sizes and conformation with highly challenging techniques.²²² However, there is no technique that allows the formation of oligomers with different aggregation kinetics of the same peptide, which could provide a systematic understanding of the structure-property and cytotoxicity relationship of amyloids.

Previously, we created a co-assembling oppositely charged (CoOP) as a strategy to study the effects of intermolecular interactions on the amyloid formation with small peptides.¹⁶⁸ By utilizing this tool, we identified that CoOPs formed with diisoleucine [II] show amyloid-like structures that also induced membrane damage and immunogenic cell death, of which effects we harvested as a vaccine adjuvant against influenza.¹⁶⁹ Furthermore, we applied this tool to induce controllable membrane damage by changing the peptide aggregation with albumin, the degree of DAMP release from cells, which regulated the antigen specific antibody production in vivo.²¹³ In this study, we analyzed a correlation between the properties of the globular and fibrillar aggregates and their function. We studied the peptide and albumin concentrations as the critical determinants of the kinetics, which altered the cytotoxicity. We hypothesized that the defined correlation between the structure, kinetic parameters, and immune responses can create a defined trend for [II] as an immunoengineering tool with predictable effects. Finally, controlled cytotoxicity levels were further applied to modulate the immune response, which was used for prophylactic breast cancer vaccine application and the level of antigen-specific antibody production against the model antigen Ovalbumin (OVA). This study shows the first molecular engineering tool that can be modulated with predictable immune responses and define global rules for peptide-based immunoengineering tools.

4.2 RESULTS AND DISCUSSION

4.2.1 THE CHANGE OF PEPTIDE AGGREGATION KINETICS AFFECTS CELLULAR VIABILITY

Albumin serves as the primary chaperone for A β in the blood (albumin amount: 640 μ M) and cerebrospinal fluid (albumin amount: 3 μ M), and is the most abundant protein in both plasma and cerebrospinal fluid.²²³ Albumin inhibits the kinetics of A β fibrillization, which contributes to the formation of increase oligomers.¹⁹⁰ Similarly, albumin also slows down [II] fibrilization, while in the absence of albumin [II] peptide aggregation favors fibrillization.²¹³ To analyze the changes in fibrillization, we prepared [II] peptides in different albumin concentrations (%w/v) and measured ThT intensity over time. Increased albumin concentration resulted in lower ThT intensities, favoring globular aggregates. On the other hand, a decrease in albumin concentration resulted in higher ThT intensities and favored fibrillar aggregates (Figure 4. 1 A,B). ThT analysis also showed that changes in albumin resulted in different ThT intensities indicating different amount of fibrillization (Figure 4. 1A). Previously, we showed the individual peptides of [II] were able to integrate into the lipid membrane, separately.²¹³ The treatment of HEK293T cells with the same amount of [II] prepared with different albumin concentrations (thus having different aggregation kinetics) for 3, 6 and 24h showed increased cytotoxicity with increasing albumin concentration (Figure 4. 1C). On the other hand, higher fibrillization resulted in lower cell death.

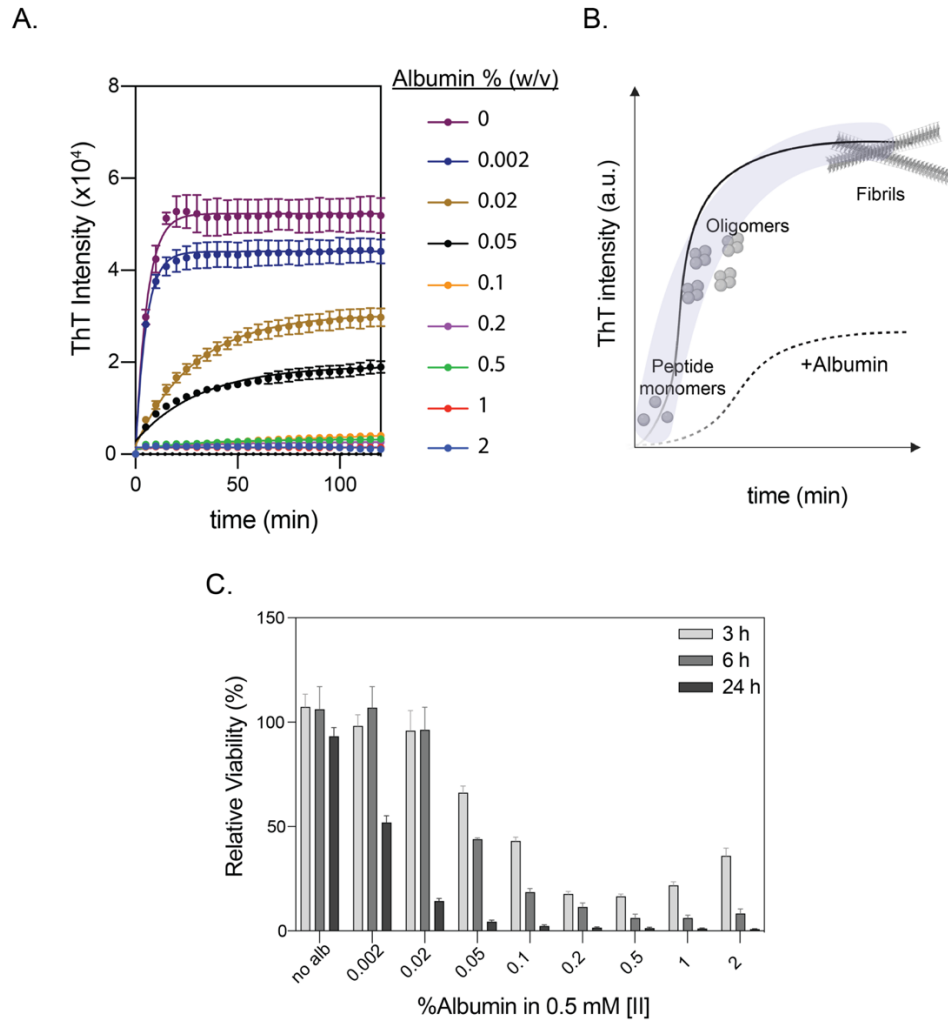


Figure 4. 1 The change of peptide aggregation kinetics affects the cellular viability. ThT measurement of [II] aggregation controlled through albumin concentration (A). Albumin modulates the [II] aggregation state (B). Relative viability of cells treated with 0.5 mM [II] peptide prepared in indicated albumin %w/v for 3, 6 and 24h (C).

4.2.2 CELL MEMBRANE DAMAGE MODULATED THROUGH CONTROL OF [II] AGGREGATION

A β aggregation induces membrane damage and contributes to neuroinflammation¹⁶¹. This effect depends on the aggregation status, which can be fibrillar (ordered) or globular structures (unordered). During the amyloid growth process, membrane damage is associated with oligomer-like structures.^{189,215} This effect conveys through the interaction of oligomer-like structures with the cell membrane and subsequent disassembly of the lipid bilayer.²²⁴

Aggregation of [II] induces ICD and DAMP release in multiple cell types through cell membrane damage.¹⁶⁹ To understand the controllability of membrane damage through modulating aggregation, we quantified lactate dehydrogenase (LDH) release (Figure 4. 2A). Organized fibrillar structures induced lower to no membrane damage (Figure 4. 2B). Increased globular structures resulted in higher membrane damage analyzed by propidium iodide (PI) staining (Figure 4. 2C). Treating the cells with fibrillar structures showed no effect on cell morphology (Figure 4. 2D). However, as the globular structures increased, cells rounded up and lost membrane integrity and protrusions, which are the morphological hallmarks for ICD²²⁵ as opposed to apoptosis (non-ICD). These results showed that the cytotoxicity is dependent on both aggregation kinetics and time.

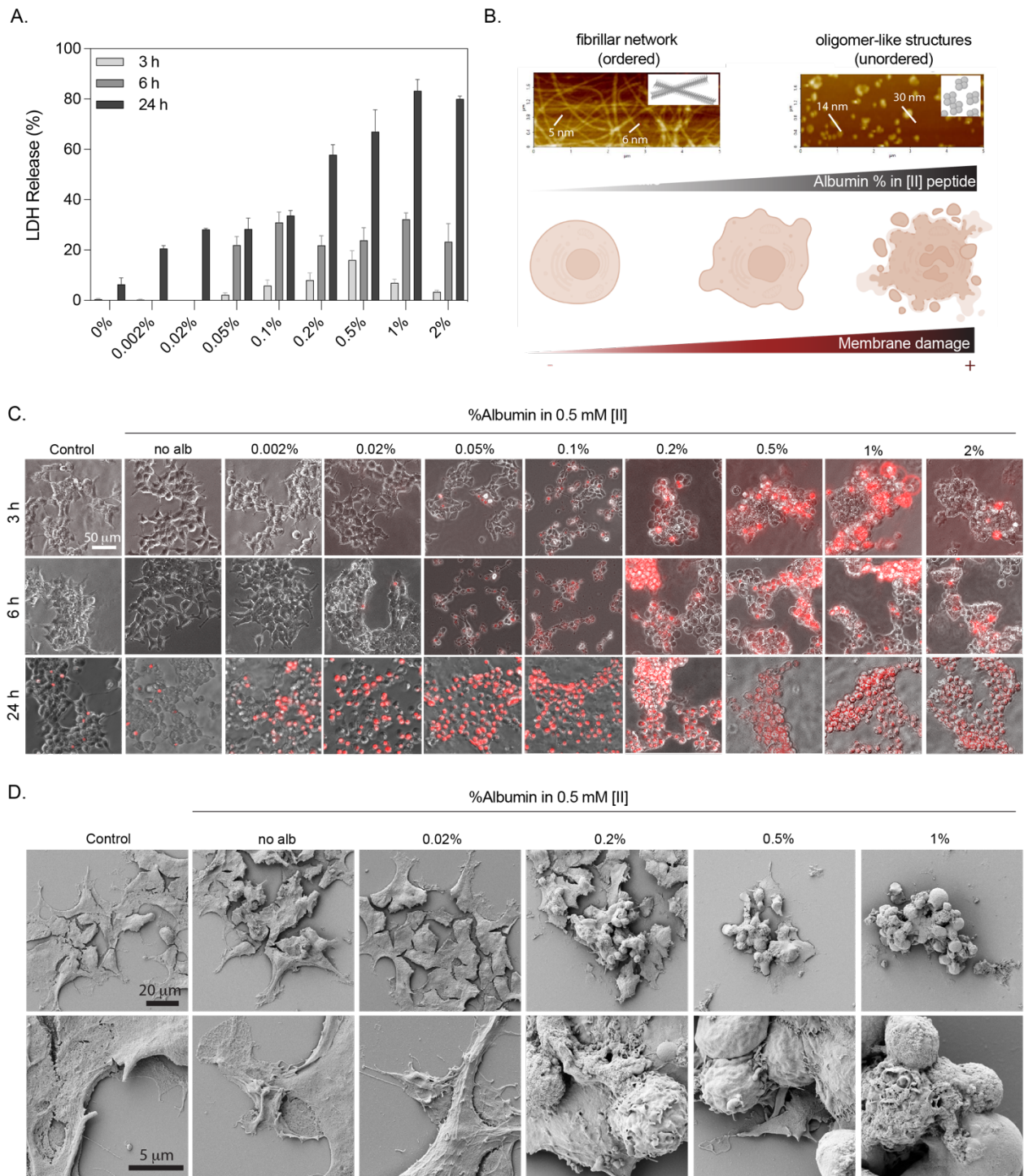


Figure 4. 2 Cell membrane damage can be modulated through control of [II] peptide aggregation. LDH release of cells treated with 0.5 mM [II] peptide prepared in indicated albumin %w/v for 3, 6 and 24h (A). Schematic illustrating the effect of fibrillar networks and globular structures on the membrane damage (B). Propidium iodide staining of cells treated with 0.5 mM [II] peptide prepared in indicated albumin %w/v for 3, 6 and 24h, the scale bar is 50 μ m (C). SEM images of the cells (top row) and magnified images (bottom

row) treated with 0.5mM peptide prepared in indicated albumin %w/v for 6h (D). The scale bars are 20 μ m and 5 μ m. (%w/v indicates weight/volume)

4.2.3 DAMP RELEASE WITH PEPTIDE AGGREGATION

The stage of cell death and the composition of DAMPs ultimately alter the immunogenicity of dying cells.²²⁶ Blocking or silencing of individual DAMPs partially reduce the immunogenic effects but not completely,²²⁷ suggesting synergistic effects of released DAMPs. To understand if the controlled membrane damage is effecting the amplitude of ICD and DAMP release, we studied four different conditions involving the highest globular aggregates to the highest fibrillar network and prepared 0.5mM [II] peptide in 0.2 w/v% (highest globular structures), 0.1 w/v%, 0.05 w/v%, and 0.02 w/v% (highest fibrillar structures) albumin and analyzed the release of HMGB-1, HSP90, extracellular ATP and dsDNA at different time points. Faster cell death was induced by 0.5mM [II] peptide in 0.2 w/v%, which showed the highest globular structures, induced the highest levels of HMGB-1, HSP90, and dsDNA release at 3 and 6h (Figure 4. 3). DAMPs could be detected at later time points for cells treated with [II] peptide prepared in 0.1% and 0.05% albumin due to slower cell death. The DAMP release heat map for the conditions we studied showed the present of all DAMPs at 3h in the supernatant of the cells treated with [II] peptide in 0.2 w/v% albumin, while other conditions had one or two DAMPs. Release of HMGB-1, HSP90, and dsDNA increased overtime at 6h (Figure 4. 3A, B, D). However, ATP is rapidly degraded as the cell death continues (Figure 4. 3C). Therefore, at 6h, the condition which had all the DAMPs in the supernatant was [II] peptide in 0.05 w/v% albumin. These data shows the importance of controlling aggregation for time-dependent modulation of DAMP release.

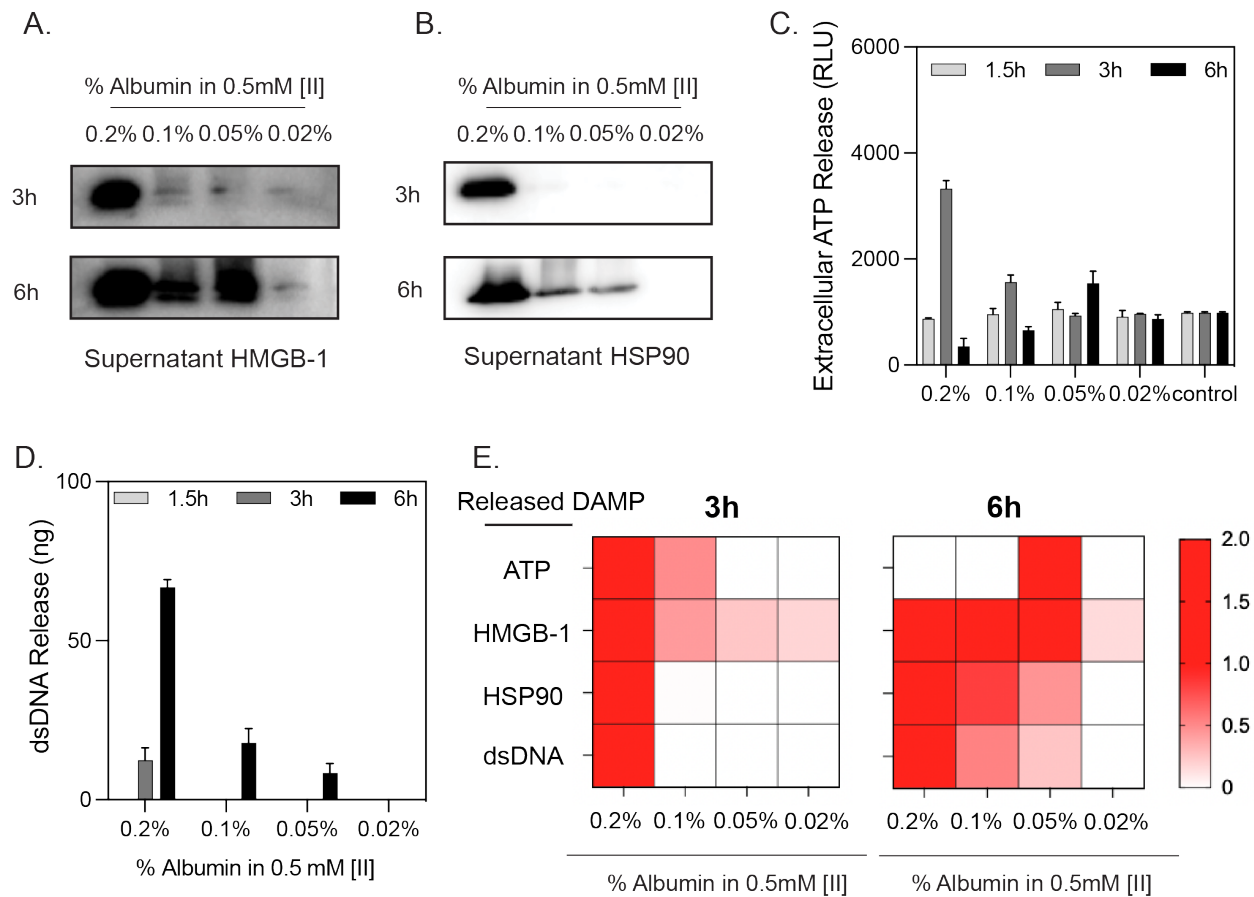


Figure 4. 3 DAMP release can be modulated through control of [II] peptide aggregation. Cells were treated with 0.5mM [II] peptide in indicated albumin w/v% for 1.5, 3 and 6h. Western blot images of HMGB-1 release (A) and HSP90 release (B) at 3 and 6h. Extracellular ATP (C) and dsDNA release (D) release at 1.5, 3 and 6h. Heat map of DAMP release at 3 and 6h (E).

4.2.4 THE CHANGE OF PEPTIDE AGGREGATION KINETICS AFFECTS THE ANTIBODY LEVELS IN VACCINE APPLICATIONS

To analyze whether control over aggregation would lead to modulation of adaptive immunity, we analyzed the level of antigen-specific antibody production against model antigen OVA by varying [II] peptide aggregation. Higher globular structures led to higher antibody production due to inducing higher local DAMP release. We used [II] prepared in 0.2 w/v%, 0.02 w/v% and 0 w/v% mouse serum albumin (MSA). Given that the

aggregation changes with the presence of albumin, we tested whether the addition of OVA into the peptide mixture alters the aggregation kinetics and viability of the cells. 10 μg of OVA (the amount used in vaccination) did not alter the fluorescent intensity of ThT measurement, indicating that OVA addition does not alter the aggregation process after reaching equilibrium (Figure 4. 4A). Moreover, addition of OVA did not alter the cytotoxicity (Figure 4. 4B). These results confirmed that OVA addition did not alter the kinetics of aggregation and cytotoxicity.

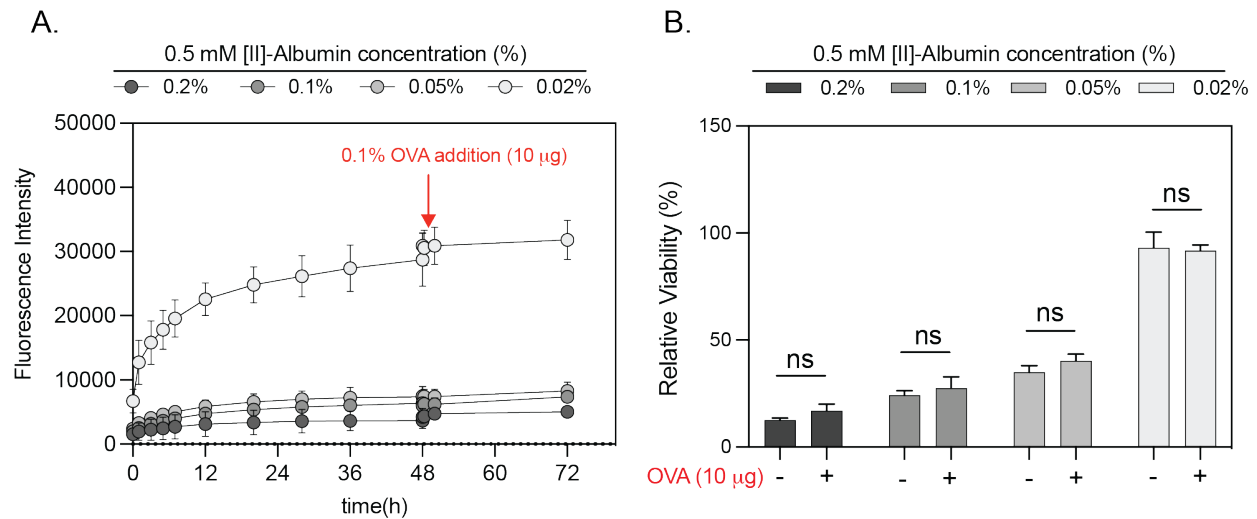


Figure 4. 4 OVA addition does not change aggregation and cell membrane damage. 10 μg of OVA was added into the [II] peptide mixture prepared in indicated albumin w/v% and ThT measurement was carried out (A). Viability measurement at 6h with 0.5mM [II] peptide prepared in indicated albumin w/v% with and without the addition of 10 μg OVA. Statistical analysis was done by one-way analysis of variance (ANOVA) with Tukey's multiple-comparison test, data are mean \pm SD, ns, not significant.

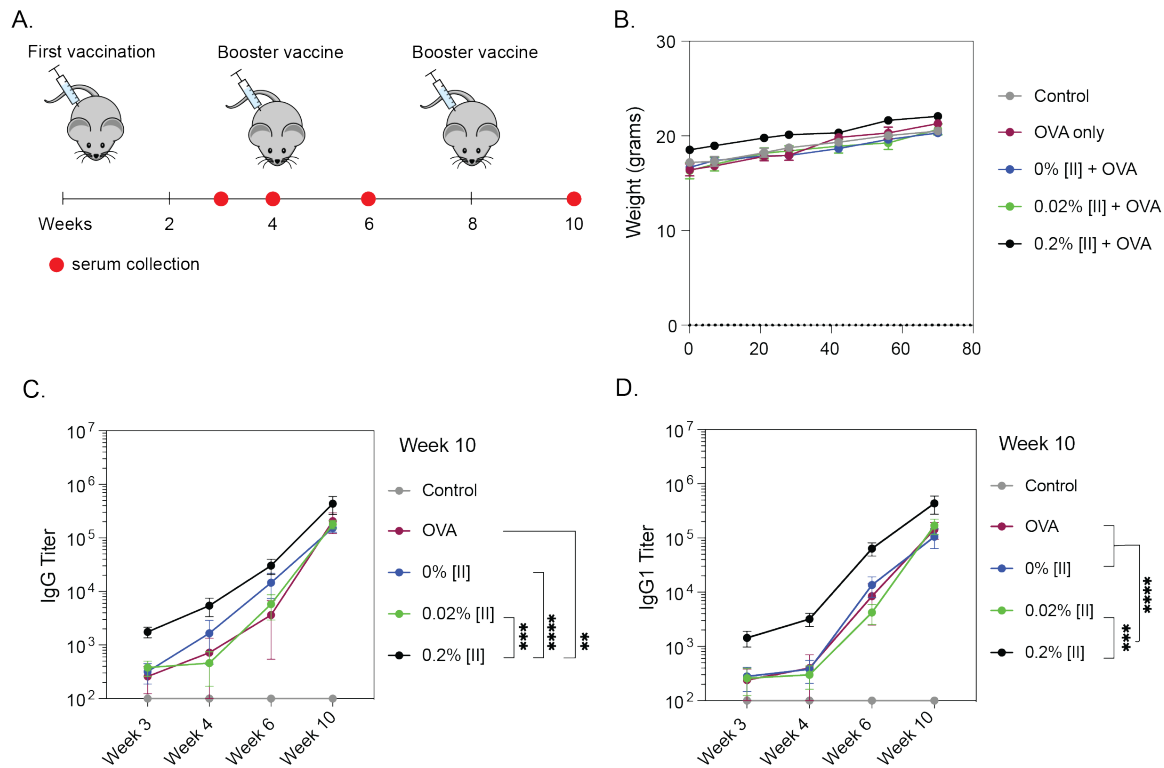


Figure 4. 5 Experimental planning of vaccination and antibody responses. Injection groups were control (only PBS), only OVA and 0.5mM [II] prepared in 0 w/v%, 0.02 w/v% and 0.2 w/v% MSA. Booster vaccinations were carried out at week 4 and 8, identical to first vaccination. Serum was collected to analyze antibody levels at week 3, 4, 6 and 10. Statistical analysis was done by one-way analysis of variance (ANOVA) with Tukey's multiple-comparison test, data are mean \pm SD, **** p<0.0001, *** p<0.001, ** p<0.01.

Then, we vaccinated mice (n=5) and used only OVA and only PBS condition as vaccination controls. Vaccinations were identical and were carried out at t=0, week 4 and week 8. Serum was collected to analyze the OVA-specific antibody formation at week 3, 4, 6 and 10 (Figure 4. 5A). Weight loss is an important safety criterion for vaccines²²⁸; therefore, we tracked the weight of the mice throughout the study and found no differences (Figure 4. 5B), indicating the safety of the vaccine. We found significantly increased IgG and IgG1 antibody levels when vaccination formulation had higher globular structures ([II] in 0.2 w/v% MSA) (Figure 4. 5C, D). [II] in 0 w/v% and 0.02 w/v% resulted

in similar antibody levels as OVA control group, potentially due to very high fibrillar structures and not enough globular structures to induce local DAMP release. These results show that [II] is a safe vaccine adjuvant tool that can be modulated to increase antigen-specific antibody levels.

4.2.5 CONTROLLED PEPTIDE AGGREGATION FOR CONTROLLING THE CELLULAR IMMUNITY

Inducing protective immunity using dying cells through ICD and DAMP release is vital for prophylactic vaccination strategies. However, immunogenicity of dying cells change depending on the stage of cell death.²²⁶ We used different aggregation profiles to induce different cell death using EMT6 breast cancer cells and developed a prophylactic vaccine. ICD and DAMP release was induced with 0.5 mM [II] in either 0.2 w/v% or 2 w/v% albumin for 1.5 and 3h, respectively. Prior to vaccination cell death was confirmed with propidium iodide (Figure 4. 6A), and intracellular ATP measurement (Figure 4. 6B). Dying cells and released DAMPs were injected subcutaneously and mice were challenged with live EMT6 cells 7 days later (Figure 4. 6C). Tumor formation on both the vaccination and challenge site were monitored and tumor-free mice were plotted as a survival graph (Figure 4. 6D). Dying cells in both conditions prolonged the tumor formation time and resulted in 40% ([II] in 0.2% albumin) and 20% ([II] in 2% albumin) complete protection against challenge. At the time of vaccination cell death profiles were similar in both groups, however, differed in protection. These results showed that modulating aggregation to control cell death alters the immunogenicity cells.

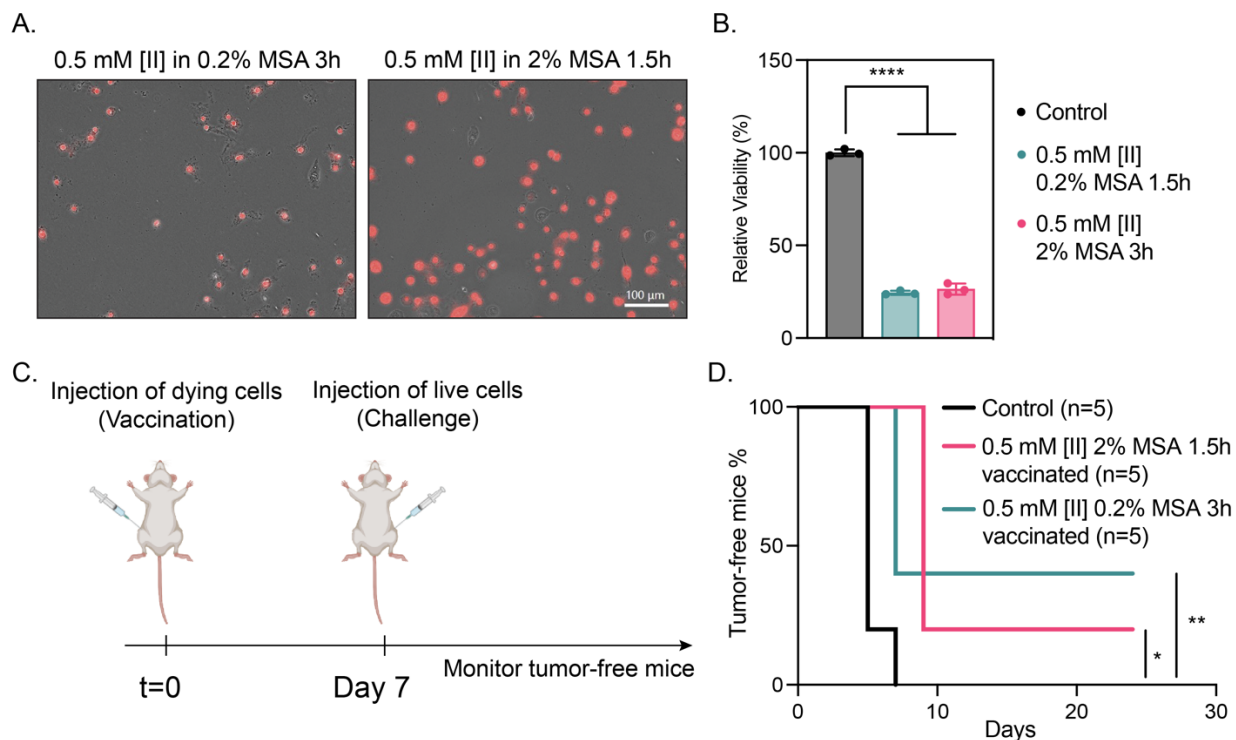


Figure 4. 6 Peptide aggregation induced cell death stages effect immunogenicity. Experimental design involving the treatment of EMT6 cells for 1.5 and 3h with 0.5 mM [II] peptide prepared in 0.02 w/v%, 0.2 w/v% and 2 w/v% albumin. Propidium iodide uptake (A) and ATP analysis (B) of dying cells prior to injection. Experimental design for prophylactic vaccination (C). Tumor-free mice survival graph (D). Statistical analysis was done by one-way analysis of variance (ANOVA) with Tukey's multiple-comparison test, data are mean \pm SD, **** $p < 0.0001$, ** $p < 0.01$, * $p < 0.1$.

4.3 CONCLUSIONS

Interest in peptide-based materials has flourished in health, energy, materials science, and national security.¹¹⁶ By advancing the discovery of peptide domains with unique intermolecular interactions, the design of peptides with desired properties in appropriate conditions can be achievable. Inspired by the mechanism of natural membrane rupturing proteins that aggregate and induce ICD and DAMP release, we showed the controllability

of DAMP release through modulating [II] peptide aggregation. Using albumin, we showed different aggregation profiles of [II] peptides like fibrillar, globular aggregates, or a mixture of fibrillar and globular aggregates. We found that fibrillar structures do not interact with the cell membrane and therefore are not cytotoxic; however, globular structures localize on the cell membrane leading to ICD and DAMP release. This platform was utilized as a controllable adjuvant and showed differential production of antigen-specific antibodies also applied for prophylactic vaccination.

4.4 MATERIALS AND METHODS

Assembly and Aggregation Kinetics. Thioflavin T (ThT) was used to understand the fibrillization of [II] in the presence and absence of albumin (bovine serum albumin, Sigma-Aldrich). Different albumin concentration indicated based on weight/volume (%w/v) and without albumin (in 1x PBS) was indicated as %0. At first, fresh albumin (20 mg/mL, 2% w/v) was dissolved in 1x PBS and diluted into 1, 0.5, 0.2, 0.1, 0.05, 0.02, 0.002 w/v % in 1x PBS. For kinetic modeling analysis, 0.1 and 0.2 μ M of albumin was used. Both KFFIIK and EFFIIE peptides were purchased from Biomatik Corporation (Canada) with higher than 95% purity. Stock peptides (10 mM in water) were diluted (0.5 mM, 0.35mM, 0.25 mM and 0.2 mM) in different albumin concentrations, individually. Each peptide counterparts were dissolved in different albumin concentrations in separate tubes. ThT was prepared as 400 μ M ThT in PBS, and 5 μ L was added to 195 μ L of 0.5 mM KFFIIK and EFFIIE (either in different albumin concentrations or in 1x PBS), individually. Each tube were sonicated at room temperature for 10 sec before mixing. Then, each peptide in the same albumin concentration was mixed and read with BioTek Neo2SM microplate

reader for 2h with 5 min intervals (Ex: 440, Em:480 with gain:90). Results were plotted by using GraphPad Prism 9.0 and initial fluorescence measurements of each group were subtracted from the rest of intensity in the same group.

Cell Culture. HEK293T and EMT-6 cells were cultured in Dulbecco's Modified Eagle Medium (DMEM) (Sigma, D6429), supplemented with 10% FBS (Hyclone SH30910.03) and 1% antibiotics; penicillin (100 U/mL), and streptomycin (100 µg/mL) (Thermo Fisher 15240062) according to the manufacturer's instructions. Cells were cultured in humidified incubator at 37°C supplied with 5% CO₂. T75 flask (TPP 90076) were used for culturing and cells were passaged upon 85% confluency by using trypsin (Sigma 59418C). Media was changed every 2 days.

Peptide preparation for in vitro and in vivo experiments. For in vitro analyses, individual counterparts of [II] peptide (EFFIIE and KFFIIK) were separately prepared in RPMI medium different albumin concentrations and mixed for 30 min prior to cell culture experiments. For in vivo analyses, individual counterparts of [II] peptide were separately prepared in 1X PBS containing either 0.2%, 0.02% or 0% mouse serum albumin (Innovative Research IMSALB100MG) and mixed for 30 min and OVA was introduced to the vaccine before injection.

Cell Titer Glo2.0 Viability. Cells were seeded onto 96 well plates and left for O/N attachment. Next day, media was removed, and treatments were carried out. Viability was measured with Cell Titer Glo 2.0 solution (Promega G9248). Luminescent signal was measured in accordance with the manufacturer's instructions. Measurements were

carried out with BioTek Neo2SM microplate reader and relative viability was calculated by using untreated control group.

LDH Release. LDH release was measured with Cytoscan-LDH Cytotoxicity Assay (Cat# 786-210). Briefly, collected supernatants were mixed with reaction mixture and incubated for 20 min at 37°C. Reaction was stopped with stop solution and absorbance was measured at 490nm and 680nm. Triton-X treatment is used as a 100 % LDH release control. 680 nm absorbance is used as the background signal and values were subtracted from 490nm absorbance values. Relative LDH release was quantified based on the positive control for LDH release (maximum LDH release through Triton-X treatment).

SEM imaging. SEM imaging was conducted by Zeiss Neon 40EsB with 2 kV at Samuel Roberts Noble Microscopy Laboratory, University of Oklahoma. Briefly, specimens treated with 0.02, 0.2, 0.5, 1% albumin with [II] and only [II] were fixed with 2% gluteraldehyde in PBS (1x pH: 7.4) and left for 6h. Then, specimens were washed with PBS for 10 minutes three times. Then, secondary fixation was performed with 1% osmium tetroxide in PBS and left at 4°C for 1 h. After fixation, specimens were immersed three times in MilliQ water to remove all fixative solutions and PBS buffer. Washing was followed by dehydration, which performed for 10 minutes each in 25, 50, 70, 85, 95 and 100% ethanol to remove water. After dehydration, specimens were exposed to critical point dry, mounted onto SEM stubs and coated with 5 nm of AuPd.

PI Staining. Propidium iodide (Thermo Fisher Scientific V13242) was used to stain the cells after treatment. Briefly, PI was added onto each well and images were captured with Keyence BZ-X710 microscope at indicated time points.

Supernatant proteins. Acetone precipitation was used to isolate supernatant proteins. Supernatants were added ice-cold acetone (4:1, v:v), incubated at -20°C for 1h and centrifuged for 10 min at 10,000 g. RIPA buffer supplemented with protease and phosphatase inhibitor cocktail was used to resuspend the proteins. Protein concentrations were determined through BCA protein assay kit (Thermo Fisher Scientific 23225) by measuring the absorbance at 562 nm in accordance with the manufacturer's instructions.

Immunoblotting, Reagents. Acrylamide/Bis-acrylamide, 30% solution (Sigma A3699), 1.5 M Tris-HCl, pH 8.8 (Teknova T1588), Tris HCl Buffer 0.5 M solution, sterile pH 6.8 (Bio Basic SD8122), Ammonium persulfate (Sigma A3678), UltraPure 10% SDS (Invitrogen 15553-027), TEMED (Thermo Fisher Scientific 17919), Dithiothreitol (DTT) (BIO-RAD 1610610) Tris Base (Fisher Bioreagents BP152), Glycine (Fisher Bioreagents BP381), 4x Laemmli sample buffer (BIO-RAD 1610747), TWEEN 20 (Sigma P9416), Mini Trans-Blot filter paper (BIO-RAD 1703932), Nitrocellulose Membranes 0.45 µm (BIO-RAD 1620115), EveryBlot Blocking Buffer (BIO-RAD 12010020), Clarity Western ECL Substrate (BIO-RAD 170-5060).

Procedure. Samples were prepared in Laemmli buffer and boiled for 8 min at 96 °C. Then, proteins were separated with sodium dodecyl sulfate-polyacrylamide gel electrophoresis (SDS-PAGE) gels (8.5% and 15%) and transferred to nitrocellulose membranes. After transfer, the membranes were blocked EverBlot Blocking Buffer and washed with Tris Buffered Saline with 0.1% Tween 20 (TBST). Blots were incubated with Direct-Blot™ HRP anti-HMGB1 Antibody (Biolegend 651411) or HSP90 overnight. Next day, the blots were washed with TBST and ECL substrate was added on top of the membranes to detect chemiluminescence signal by Azure c600 Imaging Biosystems.

HRP conjugated secondary goat-mouse antibody was used for nob-HRP conjugated primary HSP90 antibody.

Extracellular ATP release. Cell Titer Glo 2.0 solution (Promega G9248) was used to detect extracellular ATP levels. Briefly, supernatants were taken after each treatment and mixed with (1:1 v:v) with Cell Titer Glo 2.0 solution. Luminescent signal was measured in accordance with the manufacturer's instructions. Measurements were carried out with BioTek Neo2SM microplate reader.

Extracellular dsDNA release. AccuGreen™ High Sensitivity dsDNA Quantitation Kit (31066-T) was used to detect dsDNA from supernatants. Briefly, supernatants were taken after indicated treatment and time points and dsDNA release was measured in accordance with the manufacturer's instructions. Standard curve was generated and used to quantify the released dsDNA amounts.

Ethics. This study was carried out in accordance with the recommendations of Guide for the Care and Use of Laboratory Animals from National Institute of Health. Animal procedures were approved by the OU Health Sciences Center (OUHSC) Institutional Animal Care and Use Committee (protocol number R19-017A).

Immunization and Sera Collection. Model antigen Ovalbumin (OVA) (InvivoGen vac-pova) was used for immunization studies. C57BL/6 mice (n=5) were immunized subcutaneously with PBS, only OVA, 0.5 mM [II] in 0% MSA, 0.5 mM [II] in 0.02% MSA and 0.5 mM [II] in 0.2% MSA. Total of three vaccinations were carried out on t=0, week 4 and week 8. Peptides are mixed for 30 min as explained in the manuscript and mixed with

OVA at room temperature to formulate the vaccines before immunizations. Blood was collected on weeks; 3, 4, 6 and 10 through submandibular vein for antibody analyses.

Prophylactic Vaccination. BALB/c mice (n=5) were vaccinated subcutaneously with PBS, 100.000 EMT6 cells treated with 0.5 mM [II] peptide in 2% MSA for 1.5h or 100.000 EMT6 cells treated with 0.5 mM [II] peptide in 0.2% MSA for 3h. 7 days later all mice were challenged with 50.000 EMT6 cells at the contralateral site subcutaneously. Formation of palpable tumor on both vaccination site and challenge site were recorded and presented as a survival graph indicating tumor-free mice.

Enzyme Linked Immunosorbent Assay. Enzyme-linked immunosorbent assay (ELISA) Nunc MaxiSorp™ flat-bottom plates (Invitrogen 44-2404-21) were coated with 10 µg/mL with OVA phosphate coating buffer (0.1 M Na₂HPO₄ in deionized water, pH 9.0) overnight at 4°C. Next day, coated plates were blocked with 1% BSA in phosphate buffered saline-Tween (1X PBS, 0.05% Tween (PBS-T)) for 2h at room temperature. Then plates were washed 4x (200 µL for each wash) with PBS-T and incubated overnight at 4°C with serially diluted sera collected from mice in PBS-T. Next day, wells were washed 4x with PBS-T (200 µL for each wash) and incubated for 1h at room temperature either with HRP-IgG (SouthernBiotech 1030-05) (1:4000) or HRP-IgG1 (SouthernBiotech 1070-05) (1:4000). Then, wells were washed 4x with PBS-T and developed with Component Microwell Peroxidase Substrate Kit (SeraCare 5120-0043) substrate for 5 min at room temperature. Lastly, reaction was stopped with 10% SDS solution. Absorbance was measured at 405 nm to determine endpoint antibody titers.

CHAPTER 5. CONCLUSIONS AND FUTURE PERSPECTIVES

The structural organization and functional capabilities of natural materials have led to numerous technological and scientific developments. Creating materials that can address enduring problems in biomedical engineering involves adapting engineering concepts found in biological models, which is the focus of the field known as "biomaterials." Proteins are the basic building blocks of all living things. Combinational peptide intermolecular interactions direct protein structures, affecting proteins' functionality. The complexity of protein intermolecular interactions can be overcome using synthetic engineering techniques for peptides, which also offer scalable technological solutions.

Minimalistic supramolecular peptide co-assembly is paving the way to offer a convenient replacement for challenging, uncontrollable, and expensive synthesis. By taking inspiration from a natural protein, A β , we engineered peptide building blocks with multiple functions to enhance the chemical diversity and structural diversity. Co-assembly of oppositely charged peptide (CoOP) platform provides to study of intermolecular interactions in a simplistic way. CoOP consists of two oppositely charged hexapeptides, diphenylalanine (FF) at the core, and replacement units of amino acids (XX) that can be changed to understand the role of hydrophobic interactions. In the first part of this thesis, we explained the roles of electrostatic interactions between Lys (K) and Glu (E) in initiating the assembly of peptides, and a hydrophobic portion at the core contributed to the secondary structure organization. Among the CoOPs we studied, peptides consisting of diisoleucine (KFFIIK+EFFIIE, [II]) showed the highest level of organization. In the second part of the thesis, other aliphatic amino acids (V, L) were included to study hydrophobic interactions. It was found that peptide aggregation followed the trend of hydrophobicity,

where [II] was the highest, [LL] and [VV] were the second and third, respectively. All CoOPs were tested in vitro and found that [II] resulted in membrane damage due to the highest hydrophobicity index and having structural and physical similarities with the core motif of A β 16-22 (KLVFFAE). Membrane damage of [II] was tested by changing the aggregation of albumin. Membrane accumulation was enhanced when [II] showed globular aggregates, whereas fibrillar formation did not interact with the membrane. These findings were correlated with the oligomer toxicity hypothesis driven from A β . Controllable membrane damage of [II] leads to DAMP release, which was further used with two different vaccination applications.

This thesis provides a detailed account of the ability of CoOPs to form tunable assemblies by self-organization. The formation of nanostructures with unique physical and biological properties demonstrates the utility of CoOPs in the design of peptide structures. In the future, this unique design can be further modulated for tissue engineering and therapeutic delivery applications by changing the intermolecular interactions, such as hydrophobicity.

In chapter 2, we showed the modulation of aggregation kinetics by using different hydrophobic amino acids. The next steps may involve integrating non-canonical (unnatural) amino acids and combine with a bioactive epitope for tissue engineering applications. With the CoOP strategy, tissue scaffolds can be formulated by integrating biologically active epitopes such as RGD, IKVAV, and YIGSR. Furthermore, the mechanical properties of the peptide hydrogel can be tuned by changing the hydrophobicity, which is useful in creating scaffolds for engineering different tissues such as bone, cartilage, cardiac, muscle, skin, and neural. A similar strategy could also be applied to therapeutic delivery applications. The release kinetics can be tuned by

changing mesh size, affected by hydrogel assembly. Because of the variety of therapeutic windows of drugs, combining both mathematical and computational models to predict release from hydrogel networks would be significant in controlling the release of therapeutics and such technology would be an important contribution to clinical applications. Release kinetic models could also be applied to enhance the application area of the prophylactic vaccine development. We already showed aggregation-dependent immunological cell death by using albumin. Cells that are under stress because of the triggered immunogenic cell death and secreted DAMPs can be encapsulated in different peptide gels having different release kinetics. These engineered CoOP based peptide gels can facilitate the slow release of DAMPs in a localized area. Creating a local inflammatory niche coupled with the sustained DAMP release will enhance the magnitude and protective capacity of anticancer vaccines.

Furthermore, control over the CoOP strategy via enzymatic reaction is a promising approach. Using enzymes as an external stimulus for co-assembly, peptide units can be converted into cytotoxic assembly in/on the targeted cancer cells. For example, Matrix metalloproteinases (MMPs) degrade a range of extracellular matrix proteins allowing cancer cells to migrate and invade.²²⁹ Inserting MMP cleavable domain in [II] offers that the active form of peptide that will not be exposed to other parts of metabolically active tissues and avoid damage to healthy tissues. Indeed, enzyme-specific co-assembly allows the modification of peptides for different cancer types by changing enzyme-specific domains.

In summary, this thesis serves as the basis for a novel approach to developing peptide-based tools for a range of biomedical applications. The framework that is created and

examined in this thesis is simple enough to combine computational and mathematical methods in the design, as well as being modular and adaptable. The method we presented in this thesis will be a significant step forward in the design and development of peptide-based materials, especially in light of recent developments in machine learning and artificial intelligence.

REFERENCES

1. Langer R, Peppas NA. Advances in biomaterials, drug delivery, and bionanotechnology. *AIChE Journal*. 2003;49(12):2990-3006. doi:10.1002/aic.690491202
2. Sanchez C, Arribart H, Giraud Guille MM. Biomimetism and bioinspiration as tools for the design of innovative materials and systems. *Nature Materials*. 2005;4(4):277-288. doi:10.1038/nmat1339
3. Seroski DT, Dong X, Wong KM, et al. Charge guides pathway selection in β -sheet fibrillizing peptide co-assembly. *Communications Chemistry*. 2020;3(1):1-11. doi:10.1038/s42004-020-00414-w
4. Hudalla GA, Modica JA, Tian YF, et al. A self-adjuvanting supramolecular vaccine carrying a folded protein antigen. *Adv Healthc Mater*. 2013;2(8). doi:10.1002/adhm.201200435
5. Makam P, Gazit E. Minimalistic peptide supramolecular co-assembly: expanding the conformational space for nanotechnology. *Chem Soc Rev*. 2018;47(10):3406-3420. doi:10.1039/C7CS00827A
6. Yadav N, K. Chauhan M, S. Chauhan V. Short to ultrashort peptide-based hydrogels as a platform for biomedical applications. *Biomaterials Science*. 2020;8(1):84-100. doi:10.1039/C9BM01304K
7. Fleming S, Ulijn RV. Design of nanostructures based on aromatic peptide amphiphiles. *Chem Soc Rev*. 2014;43(23):8150-8177. doi:10.1039/C4CS00247D
8. Zhang S. Fabrication of novel biomaterials through molecular self-assembly. *Nature Biotechnology*. 2003;21(10):1171-1178. doi:10.1038/nbt874
9. Abid N, Khan AM, Shujait S, et al. Synthesis of nanomaterials using various top-down and bottom-up approaches, influencing factors, advantages, and disadvantages: A review. *Advances in Colloid and Interface Science*. 2022;300:102597. doi:10.1016/j.cis.2021.102597
10. Smith KH, Tejeda-Montes E, Poch M, Mata A. Integrating top-down and self-assembly in the fabrication of peptide and protein-based biomedical materials. *Chem Soc Rev*. 2011;40(9):4563-4577. doi:10.1039/C1CS15064B
11. Cook AB, Clemons TD. Bottom-Up versus Top-Down Strategies for Morphology Control in Polymer-Based Biomedical Materials. *Advanced NanoBiomed Research*. 2022;2(1):2100087. doi:10.1002/anbr.202100087

12. Groß A, Hashimoto C, Sticht H, Eichler J. Synthetic Peptides as Protein Mimics. *Front Bioeng Biotechnol.* 2016;3. doi:10.3389/fbioe.2015.00211
13. Frantz C, Stewart KM, Weaver VM. The extracellular matrix at a glance. *J Cell Sci.* 2010;123(24):4195-4200. doi:10.1242/jcs.023820
14. Gazit E. Reductionist Approach in Peptide-Based Nanotechnology. *Annu Rev Biochem.* 2018;87(1):533-553. doi:10.1146/annurev-biochem-062917-012541
15. Vijayakumar M, Qian H, Zhou HX. Hydrogen bonds between short polar side chains and peptide backbone: Prevalence in proteins and effects on helix-forming propensities. *Proteins: Structure, Function, and Bioinformatics.* 1999;34(4):497-507. doi:10.1002/(SICI)1097-0134(19990301)34:4<497::AID-PROT9>3.0.CO;2-G
16. Mu Y, Yu M. Effects of hydrophobic interaction strength on the self-assembled structures of model peptides. *Soft Matter.* 2014;10(27):4956-4965. doi:10.1039/C4SM00378K
17. Gazit E. A possible role for π -stacking in the self-assembly of amyloid fibrils. *The FASEB Journal.* 2002;16(1):77-83. doi:10.1096/fj.01-0442hyp
18. Peptide self-assembly: thermodynamics and kinetics - Chemical Society Reviews (RSC Publishing). Accessed March 19, 2020. <https://pubs.rsc.org/ko/content/articlelanding/2016/cs/c6cs00176a/unauth#!divAbstract>
19. Fan T, Yu X, Shen B, Sun L. Peptide Self-Assembled Nanostructures for Drug Delivery Applications. *Journal of Nanomaterials.* 2017;2017:1-16. doi:10.1155/2017/4562474
20. Bera S, Gazit E. Self-assembly of Functional Nanostructures by Short Helical Peptide Building Blocks. *Protein & Peptide Letters.* 2018;26(2):88-97. doi:10.2174/0929866525666180917163142
21. Lupas BAN, Gruber M. The structure of alpha-helical coiled coils. *Advances in Protein Chemistry.* 2005;70(04):37-78. doi:10.1016/S0065-3233(04)70003-0
22. Nowick JS. Exploring β -Sheet Structure and Interactions with Chemical Model Systems. *Accounts of Chemical Research.* 2008;41(10):1319-1330. doi:10.1016/j.cgh.2008.07.016.Cytokeratin
23. Stephanopoulos N, Ortony JH, Stupp SI. Self-assembly for the synthesis of functional biomaterials. *Acta Materialia.* 2013;61(3):912-930. doi:10.1016/j.actamat.2012.10.046
24. Dobson CM. Protein-misfolding diseases: Getting out of shape. *Nature.* 2002;418(6899):729-730. doi:10.1038/418729a

25. Das S, Jacob RS, Patel K, Singh N, Maji SK. Amyloid Fibrils: Versatile Biomaterials for Cell Adhesion and Tissue Engineering Applications. *Biomacromolecules*. 2018;19(6):1826-1839. doi:10.1021/acs.biomac.8b00279
26. Murphy RM. Kinetics of amyloid formation and membrane interaction with amyloidogenic proteins. *Biochimica et Biophysica Acta (BBA) - Biomembranes*. 2007;1768(8):1923-1934. doi:10.1016/j.bbamem.2006.12.014
27. Raskatov JA, Teplow DB. Using chirality to probe the conformational dynamics and assembly of intrinsically disordered amyloid proteins. *Sci Rep*. 2017;7(1):12433. doi:10.1038/s41598-017-10525-5
28. Caballero AB, Gamez P. Nanochaperone-Based Strategies to Control Protein Aggregation Linked to Conformational Diseases. *Angewandte Chemie*. 2021;133(1):41-52. doi:10.1002/ange.202007924
29. Makin OS, Atkins E, Sikorski P, Johansson J, Serpell LC. Molecular basis for amyloid fibril formation and stability. *PNAS*. 2005;102(2):315-320. doi:10.1073/pnas.0406847102
30. Yan X, Zhu P, Li J. Self-assembly and application of diphenylalanine-based nanostructures. *Chem Soc Rev*. 2010;39(6):1877-1890. doi:10.1039/b915765b
31. Tenidis K, Waldner M, Bernhagen J, et al. Identification of a penta- and hexapeptide of islet amyloid polypeptide (IAPP) with amyloidogenic and cytotoxic properties. Edited by R. Huber. *Journal of Molecular Biology*. 2000;295(4):1055-1071. doi:10.1006/jmbi.1999.3422
32. Lan Y, Lv M, Guo S, et al. Molecular motifs encoding self-assembly of peptide fibers into molecular gels. *Soft Matter*. 2019;15(45):9205-9214. doi:10.1039/C9SM01793C
33. Chun Ke P, Zhou R, C. Serpell L, et al. Half a century of amyloids: past, present and future. *Chemical Society Reviews*. 2020;49(15):5473-5509. doi:10.1039/C9CS00199A
34. Krone MG, Hua L, Soto P, Zhou R, Berne BJ, Shea JE. Role of Water in Mediating the Assembly of Alzheimer Amyloid- β A β 16-22 Protofilaments. *J Am Chem Soc*. 2008;130(33):11066-11072. doi:10.1021/ja8017303
35. Frederix PWJM, Scott GG, Abul-Haija YM, et al. Exploring the sequence space for (tri-)peptide self-assembly to design and discover new hydrogels. *Nat Chem*. 2015;7(1):30-37. doi:10.1038/nchem.2122
36. Martin AD, Wojciechowski JP, Robinson AB, et al. Controlling self-assembly of diphenylalanine peptides at high pH using heterocyclic capping groups. *Scientific Reports*. 2017;7(1):43947. doi:10.1038/srep43947

37. Tang Y, Yao Y, Wei G. Expanding the structural diversity of peptide assemblies by coassembling dipeptides with diphenylalanine. *Nanoscale*. 2020;12(5):3038-3049. doi:10.1039/C9NR09317F
38. Smith AM, Williams RJ, Tang C, et al. Fmoc-Diphenylalanine Self Assembles to a Hydrogel via a Novel Architecture Based on π - π Interlocked β -Sheets. *Advanced Materials*. 2008;20(1):37-41. doi:10.1002/adma.200701221
39. M. Abul-Haija Y, G. Scott G, Kishore Sahoo J, Tuttle T, V. Ulijn R. Cooperative, ion-sensitive co-assembly of tripeptide hydrogels. *Chemical Communications*. 2017;53(69):9562-9565. doi:10.1039/C7CC04796G
40. Huang R, Wang Y, Qi W, Su R, He Z. Temperature-induced reversible self-assembly of diphenylalanine peptide and the structural transition from organogel to crystalline nanowires. *Nanoscale Res Lett*. 2014;9(1):653. doi:10.1186/1556-276X-9-653
41. Chen L, Raeburn J, Sutton S, et al. Tuneable mechanical properties in low molecular weight gels. *Soft Matter*. 2011;7(20):9721-9727. doi:10.1039/C1SM05827D
42. Xu XD, Chen CS, Lu B, Cheng SX, Zhang XZ, Zhuo RX. Coassembly of Oppositely Charged Short Peptides into Well-Defined Supramolecular Hydrogels. *J Phys Chem B*. 2010;114(7):2365-2372. doi:10.1021/jp9102417
43. Fleming S, Debnath S, Frederix PWJM, Hunt NT, Ulijn RV. Insights into the Coassembly of Hydrogelators and Surfactants Based on Aromatic Peptide Amphiphiles. *Biomacromolecules*. 2014;15(4):1171-1184. doi:10.1021/bm401720z
44. Raeburn J, J. Adams D. Multicomponent low molecular weight gelators. *Chemical Communications*. 2015;51(25):5170-5180. doi:10.1039/C4CC08626K
45. Roy K, Chetia M, Kumar Sarkar A, Chatterjee S. Co-assembly of charge complementary peptides and their applications as organic dye/heavy metal ion (Pb²⁺, Hg²⁺) absorbents and arsenic(III/V) detectors. *RSC Advances*. 2020;10(69):42062-42075. doi:10.1039/D0RA08407G
46. Adler-Abramovich L, Marco P, Arnon ZA, et al. Controlling the Physical Dimensions of Peptide Nanotubes by Supramolecular Polymer Coassembly. *ACS Nano*. 2016;10(8):7436-7442. doi:10.1021/acsnano.6b01587
47. Webber MJ, Appel EA, Meijer EW, Langer R. Supramolecular biomaterials. *Nature Materials*. 2016;15(1):13-26. doi:10.1038/nmat4474
48. Furth ME, Atala A, Van Dyke ME. Smart biomaterials design for tissue engineering and regenerative medicine. *Biomaterials*. 2007;28(34):5068-5073. doi:10.1016/j.biomaterials.2007.07.042
49. Holmes TC. Novel peptide-based biomaterial scaffolds for tissue engineering. *Trends in Biotechnology*. 2002;20(1):16-21. doi:10.1016/S0167-7799(01)01840-6

50. Stevens MM, George JH. Exploring and Engineering the Cell Surface Interface. *Science*. 2005;310(5751):1135-1138. doi:10.1126/science.1106587
51. Zhou M, Smith AM, Das AK, et al. Self-assembled peptide-based hydrogels as scaffolds for anchorage-dependent cells. *Biomaterials*. 2009;30(13):2523-2530. doi:10.1016/j.biomaterials.2009.01.010
52. Chakraborty P, Guterman T, Adadi N, et al. A Self-Healing, All-Organic, Conducting, Composite Peptide Hydrogel as Pressure Sensor and Electrogenic Cell Soft Substrate. *ACS Nano*. 2019;13(1):163-175. doi:10.1021/acsnano.8b05067
53. Chakraborty P, Oved H, Bychenko D, et al. Nanoengineered Peptide-Based Antimicrobial Conductive Supramolecular Biomaterial for Cardiac Tissue Engineering. *Advanced Materials*. 2021;33(26):2008715. doi:10.1002/adma.202008715
54. Schnaider L, Shimonov L, Kreiser T, et al. Ultrashort Cell-Penetrating Peptides for Enhanced Sonophoresis-Mediated Transdermal Transport. *ACS Appl Bio Mater*. 2020;3(12):8395-8401. doi:10.1021/acscabm.0c00682
55. Sinnige T. Molecular mechanisms of amyloid formation in living systems. *Chem Sci*. 2022;13(24):7080-7097. doi:10.1039/D2SC01278B
56. Giorgetti S, Greco C, Tortora P, Aprile FA. Targeting Amyloid Aggregation: An Overview of Strategies and Mechanisms. *Int J Mol Sci*. 2018;19(9):2677. doi:10.3390/ijms19092677
57. Campioni S, Mannini B, Zampagni M, et al. A causative link between the structure of aberrant protein oligomers and their toxicity. *Nat Chem Biol*. 2010;6(2):140-147. doi:10.1038/nchembio.283
58. Das AK, Rawat A, Bhowmik D, Pandit R, Huster D, Maiti S. An Early Folding Contact between Phe19 and Leu34 is Critical for Amyloid- β Oligomer Toxicity. *ACS Chem Neurosci*. 2015;6(8):1290-1295. doi:10.1021/acscchemneuro.5b00074
59. Cao P, Abedini A, Wang H, et al. Islet amyloid polypeptide toxicity and membrane interactions. *Proceedings of the National Academy of Sciences*. 2013;110(48):19279-19284. doi:10.1073/pnas.1305517110
60. Engel MFM, Khemtémourian L, Kleijer CC, et al. Membrane damage by human islet amyloid polypeptide through fibril growth at the membrane. *Proceedings of the National Academy of Sciences*. 2008;105(16):6033-6038. doi:10.1073/pnas.0708354105
61. Bieschke J, Herbst M, Wiglenda T, et al. Small-molecule conversion of toxic oligomers to nontoxic β -sheet-rich amyloid fibrils. *Nat Chem Biol*. 2012;8(1):93-101. doi:10.1038/nchembio.719

62. Yasumoto T, Takamura Y, Tsuji M, et al. High molecular weight amyloid β 1-42 oligomers induce neurotoxicity via plasma membrane damage. *Alzheimer's & Dementia*. 2020;16(S2):e037546. doi:<https://doi.org/10.1002/alz.037546>
63. Mannini B, Mulvihill E, Sgromo C, et al. Toxicity of Protein Oligomers Is Rationalized by a Function Combining Size and Surface Hydrophobicity. *ACS Chem Biol*. 2014;9(10):2309-2317. doi:10.1021/cb500505m
64. Im D, Heo CE, Son MK, Park CR, Kim HI, Choi JM. Kinetic Modulation of Amyloid- β (1–42) Aggregation and Toxicity by Structure-Based Rational Design. *J Am Chem Soc*. 2022;144(4):1603-1611. doi:10.1021/jacs.1c10173
65. Eisele YS, Monteiro C, Fearn C, et al. Targeting protein aggregation for the treatment of degenerative diseases. *Nat Rev Drug Discov*. 2015;14(11):759-780. doi:10.1038/nrd4593
66. Young LM, Ashcroft AE, Radford SE. Small molecule probes of protein aggregation. *Curr Opin Chem Biol*. 2017;39:90-99. doi:10.1016/j.cbpa.2017.06.008
67. Willbold D, Strodel B, Schröder GF, Hoyer W, Heise H. Amyloid-type Protein Aggregation and Prion-like Properties of Amyloids. *Chem Rev*. 2021;121(13):8285-8307. doi:10.1021/acs.chemrev.1c00196
68. Zhao X, Pan F, Xu H, et al. Molecular self-assembly and applications of designer peptide amphiphiles. *Chem Soc Rev*. 2010;39(9):3480-3498. doi:10.1039/B915923C
69. Hu X, Liao M, Gong H, et al. Recent advances in short peptide self-assembly: from rational design to novel applications. *Current Opinion in Colloid & Interface Science*. 2020;45:1-13. doi:10.1016/j.cocis.2019.08.003
70. Sardan Ekiz M, Cinar G, Khalily MA, Guler MO. Self-assembled peptide nanostructures for functional materials. *Nanotechnology*. 2016;27:1-37. doi:10.1088/0957-4484/27/40/402002
71. Griffiths PR, Haseth JAD. *Fourier Transform Infrared Spectrometry*,. 2nd Edition. John Wiley & Sons; 2007. Accessed August 9, 2020. <https://www.wiley.com/en-us/Fourier+Transform+Infrared+Spectrometry%2C+2nd+Edition-p-9780471194040>
72. Yang H, Yang S, Kong J, Dong A, Yu S. Obtaining information about protein secondary structures in aqueous solution using Fourier transform IR spectroscopy. *Nature Protocols*. 2015;10(3):382-396. doi:10.1038/nprot.2015.024
73. Krimm S, Bandekar J. Vibrational Spectroscopy and Conformation of Peptides, Polypeptides, and Proteins. *Advances in Protein Chemistry*. 1986;38:181-364. doi:10.1016/S0065-3233(08)60528-8

74. Pelton JT, McLean LR. Spectroscopic Methods for Analysis of Protein Secondary Structure. *Analytical Biochemistry*. 2000;277(2):167-176. doi:10.1006/abio.1999.4320
75. Tang JD, Mura C, Lampe KJ. Stimuli-Responsive, Pentapeptide, Nanofiber Hydrogel for Tissue Engineering. *J Am Chem Soc*. 2019;141(12):4886-4899. doi:10.1021/jacs.8b13363
76. Beck JG, Frank AO, Kessler H. NMR of Peptides. In: *NMR of Biomolecules*. John Wiley & Sons, Ltd; 2012:328-344. doi:10.1002/9783527644506.ch19
77. Mendes AC, Baran ET, Reis RL, Azevedo HS. Self-assembly in nature: using the principles of nature to create complex nanobiomaterials. *Wiley Interdisciplinary Reviews: Nanomedicine and Nanobiotechnology*. 2013;5(6):582-612. doi:10.1002/wnan.1238
78. Rajbhandary A, Nilsson BL. Investigating the effects of peptoid substitutions in self-assembly of Fmoc-diphenylalanine derivatives. *Peptide Science*. 2017;108(2):e22994. doi:10.1002/bip.22994
79. de Groot NS, Parella T, Aviles FX, Vendrell J, Ventura S. Ile-Phe Dipeptide Self-Assembly: Clues to Amyloid Formation. *Biophys J*. 2007;92(5):1732-1741. doi:10.1529/biophysj.106.096677
80. Jekhmane S, Prachar M, Pugliese R, et al. Design Parameters of Tissue-Engineering Scaffolds at the Atomic Scale. *Angewandte Chemie International Edition*. 2019;58(47):16943-16951. doi:10.1002/anie.201907880
81. Shao Q, Wong KM, Seroski DT, et al. Anatomy of a selectively coassembled β -sheet peptide nanofiber. *PNAS*. 2020;117(9):4710-4717. doi:10.1073/pnas.1912810117
82. Micsonai A, Wien F, Kernya L, et al. Accurate secondary structure prediction and fold recognition for circular dichroism spectroscopy. *PNAS*. 2015;112(24):E3095-E3103. doi:10.1073/pnas.1500851112
83. Bakshi K, Liyanage MR, Volkin DB, Middaugh CR. Circular Dichroism of Peptides. In: Nixon AE, ed. *Therapeutic Peptides: Methods and Protocols*. Methods in Molecular Biology. Humana Press; 2014:247-253. doi:10.1007/978-1-62703-673-3_17
84. J. Miles A, A. Wallace B. Circular dichroism spectroscopy of membrane proteins. *Chemical Society Reviews*. 2016;45(18):4859-4872. doi:10.1039/C5CS00084J
85. Li J, Du X, Hashim S, Shy A, Xu B. Aromatic–Aromatic Interactions Enable α -Helix to β -Sheet Transition of Peptides to Form Supramolecular Hydrogels. *J Am Chem Soc*. 2017;139(1):71-74. doi:10.1021/jacs.6b11512

86. Ji W, Yuan C, Chakraborty P, Gilead S, Yan X, Gazit E. Stoichiometry-controlled secondary structure transition of amyloid-derived supramolecular dipeptide co-assemblies. *Communications Chemistry*. 2019;2(1):1-11. doi:10.1038/s42004-019-0170-z
87. Hawe A, Sutter M, Jiskoot W. Extrinsic Fluorescent Dyes as Tools for Protein Characterization. *Pharm Res*. 2008;25(7):1487-1499. doi:10.1007/s11095-007-9516-9
88. Wei G, Su Z, Reynolds NP, et al. Self-assembling peptide and protein amyloids: From structure to tailored function in nanotechnology. *Chemical Society Reviews*. 2017;46(15):4661-4708. doi:10.1039/c6cs00542j
89. Aliyan A, Cook NP, Martí AA. Interrogating Amyloid Aggregates using Fluorescent Probes. *Chem Rev*. 2019;119(23):11819-11856. doi:10.1021/acs.chemrev.9b00404
90. Malmos KG, Blancas-Mejia LM, Weber B, et al. ThT 101: a primer on the use of thioflavin T to investigate amyloid formation. *Amyloid*. 2017;24(1):1-16. doi:10.1080/13506129.2017.1304905
91. Hellstrand E, Boland B, Walsh DM, Linse S. Amyloid β -Protein Aggregation Produces Highly Reproducible Kinetic Data and Occurs by a Two-Phase Process. *ACS Chem Neurosci*. 2009;1(1):13-18. doi:10.1021/cn900015v
92. Cinar G, Orujalipour I, Su CJ, Jeng US, Ide S, Guler MO. Supramolecular Nanostructure Formation of Coassembled Amyloid Inspired Peptides. *Langmuir*. 2016;32(25):6506-6514. doi:10.1021/acs.langmuir.6b00704
93. Losev Y, Paul A, Frenkel-Pinter M, et al. Novel model of secreted human tau protein reveals the impact of the abnormal N-glycosylation of tau on its aggregation propensity. *Scientific Reports*. 2019;9(1):2254. doi:10.1038/s41598-019-39218-x
94. Wu C, Scott J, Shea JE. Binding of Congo Red to Amyloid Protofibrils of the Alzheimer A β 9–40 Peptide Probed by Molecular Dynamics Simulations. *Biophysical Journal*. 2012;103(3):550-557. doi:10.1016/j.bpj.2012.07.008
95. Zhan FK, Liu JC, Cheng B, et al. Tumor targeting with DGEA peptide ligands: a new aromatic peptide amphiphile for imaging cancers. *Chemical Communications*. 2019;55(8):1060-1063. doi:10.1039/C8CC08679F
96. Peterson AM, Tan Z, Kimbrough EM, Heemstra JM. 3,3'-Diocetadecyloxycarbocyanine perchlorate (DiO) as a fluorogenic probe for measurement of critical micelle concentration. *Anal Methods*. 2015;7(16):6877-6882. doi:10.1039/C5AY01444A
97. Kalyanasundaram K, Thomas JK. Environmental effects on vibronic band intensities in pyrene monomer fluorescence and their application in studies of micellar systems. *J Am Chem Soc*. 1977;99(7):2039-2044.

98. Bains GK, Kim SH, Sorin EJ, Narayanaswami V. Extent of Pyrene Excimer Fluorescence Emission is a Reflector of Distance and Flexibility: Analysis of the Segment Linking the LDL Receptor-binding and Tetramerization Domains of Apolipoprotein E3. *Biochemistry*. 2012;51(31):6207-6219. doi:10.1021/bi3005285
99. Morel B, Carrasco MP, Jurado S, Marco C, Conejero-Lara F. Dynamic micellar oligomers of amyloid beta peptides play a crucial role in their aggregation mechanisms. *Phys Chem Chem Phys*. 2018;20(31):20597-20614. doi:10.1039/C8CP02685H
100. Aguiar J, Carpena P, Molina-Bolívar JA, Carnero Ruiz C. On the determination of the critical micelle concentration by the pyrene 1:3 ratio method. *Journal of Colloid and Interface Science*. 2003;258(1):116-122. doi:10.1016/S0021-9797(02)00082-6
101. Hutchinson JA, Hamley IW, Torras J, Alemán C, Seitsonen J, Ruokolainen J. Self-Assembly of Lipopeptides Containing Short Peptide Fragments Derived from the Gastrointestinal Hormone PYY3–36: From Micelles to Amyloid Fibrils. *J Phys Chem B*. 2019;123(3):614-621. doi:10.1021/acs.jpccb.8b11097
102. Stuart MCA, Pas JC van de, Engberts JBFN. The use of Nile Red to monitor the aggregation behavior in ternary surfactant–water–organic solvent systems. *Journal of Physical Organic Chemistry*. 2005;18(9):929-934. doi:10.1002/poc.919
103. Torres-Martínez A, A. Angulo-Pachón C, Galindo F, F. Miravet J. In between molecules and self-assembled fibrillar networks: highly stable nanogel particles from a low molecular weight hydrogelator. *Soft Matter*. 2019;15(17):3565-3572. doi:10.1039/C9SM00252A
104. Hamsici S, Sardan Ekiz M, Cinar Ciftci G, Tekinay AB, Guler MO. Gemcitabine Integrated Nano-Prodrug Carrier System. *Bioconjugate Chem*. 2017;28(5):1491-1498. doi:10.1021/acs.bioconjchem.7b00155
105. Ji W, Yuan C, Chakraborty P, et al. Coassembly-Induced Transformation of Dipeptide Amyloid-Like Structures into Stimuli-Responsive Supramolecular Materials. *ACS Nano*. 2020;14(6):7181-7190. doi:10.1021/acsnano.0c02138
106. Acar H, Srivastava S, Chung EJ, et al. Self-assembling peptide-based building blocks in medical applications. *Adv Drug Deliv Rev*. 2017;110-111:65-79. doi:10.1016/j.addr.2016.08.006
107. Nagy KJ, Giano MC, Jin A, Pochan DJ, Schneider JP. Enhanced Mechanical Rigidity of Hydrogels Formed From Enantiomeric Peptide Assemblies. *J Am Chem Soc*. 2011;133(38):14975-14977. doi:10.1021/ja206742m
108. Wu D, Sinha N, Lee J, et al. Polymers with controlled assembly and rigidity made with click-functional peptide bundles. *Nature*. 2019;574(7780):658-662. doi:10.1038/s41586-019-1683-4

109. Hamsici S, Sardan Ekiz M, Cinar Ciftci G, Tekinay AB, Guler MO. Gemcitabine Integrated Nano-Prodrug Carrier System. *Bioconjugate Chem.* 2017;28(5):1491-1498. doi:10.1021/acs.bioconjchem.7b00155
110. Cinar G, Ozdemir A, Hamsici S, et al. Local delivery of doxorubicin through supramolecular peptide amphiphile nanofiber gels. *Biomater Sci.* 2017;5(1):67-76. doi:10.1039/C6BM00656F
111. Gunay G, Sardan Ekiz M, Ferhati X, et al. Antigenic GM3 Lactone Mimetic Molecule Integrated Mannosylated Glycopeptide Nanofibers for the Activation and Maturation of Dendritic Cells. *ACS Appl Mater Interfaces.* 2017;9(19):16035-16042. doi:10.1021/acsami.7b04094
112. Gunay G, Sever M, Tekinay AB, Guler MO. Three-Dimensional Laminin Mimetic Peptide Nanofiber Gels for In Vitro Neural Differentiation. *Biotechnol J.* 2017;12(12):1-9. doi:https://doi.org/10.1002/biot.201700080
113. Hamsici S, Cinar G, Celebioglu A, Uyar T, B. Tekinay A, O. Guler M. Bioactive peptide functionalized aligned cyclodextrin nanofibers for neurite outgrowth. *J Mater Chem B.* 2017;5(3):517-524. doi:10.1039/C6TB02441F
114. Acar H, Garifullin R, Aygun LE, Okyay AK, Guler MO. Amyloid-like peptide nanofiber templated titania nanostructures as dye sensitized solar cell anodic materials. *J Mater Chem A.* 2013;1(36):10979-10984. doi:10.1039/C3TA11542A
115. Acar H. *Self-Assembled Peptide Template Directed Synthesis of One-Dimensional Inorganic Nanostructures and Their Applications.* Thesis. Bilkent University; 2012. Accessed February 8, 2020. <http://repository.bilkent.edu.tr/handle/11693/16921>
116. Hamsici S, Gunay G, Kirit H, Kamatar A, Loving K, Acar H. CHAPTER 9 Drug Delivery Applications of Peptide Materials. In: *Peptide-Based Biomaterials.* The Royal Society of Chemistry; 2021:291-334. doi:10.1039/9781839161148-00291
117. Webber MJ, Pashuck ET. (Macro)molecular self-assembly for hydrogel drug delivery. *Adv Drug Deliv Rev.* 2021;172:275-295. doi:10.1016/j.addr.2021.01.006
118. Wei G, Su Z, P. Reynolds N, et al. Self-assembling peptide and protein amyloids: from structure to tailored function in nanotechnology. *Chem Soc Rev.* 2017;46(15):4661-4708. doi:10.1039/C6CS00542J
119. Aliyan A, Cook NP, Martí AA. Interrogating Amyloid Aggregates using Fluorescent Probes. *Chem Rev.* 2019;119(23):11819-11856. doi:10.1021/acs.chemrev.9b00404
120. Lodish H, Berk A, Zipursky SL, Matsudaira P, Baltimore D, Darnell J. Noncovalent Bonds. In: *Molecular Cell Biology. 4th Edition.* 4th ed. WH Freeman; 2000. Accessed September 1, 2021. <https://www.ncbi.nlm.nih.gov/books/NBK21726/>

121. Zeravcic Z, Manoharan VN, Brenner MP. Size limits of self-assembled colloidal structures made using specific interactions. *PNAS*. 2014;111(45):15918-15923. doi:10.1073/pnas.1411765111
122. Klimov DK, Thirumalai D. Dissecting the Assembly of A β 16–22 Amyloid Peptides into Antiparallel β Sheets. *Structure*. 2003;11(3):295-307. doi:10.1016/S0969-2126(03)00031-5.
123. White AD, Keefe AJ, Ella-Menye JR, et al. Free Energy of Solvated Salt Bridges: A Simulation and Experimental Study. *J Phys Chem B*. 2013;117(24):7254-7259. doi:10.1021/jp4024469
124. Jalan AA, Hartgerink JD. Pairwise Interactions in Collagen and the Design of Heterotrimeric Helices. *Curr Opin Chem Biol*. 2013;17(6):960-967. doi:10.1016/j.cbpa.2013.10.019.
125. Banerjee J, Azevedo HS. Crafting of Functional Biomaterials by Directed Molecular Self-Assembly of Triple Helical Peptide Building Blocks. *Interface Focus*. 2017;7(6):20160138. doi:10.1098/rsfs.2016.0138.
126. Monera OD, Sereda TJ, Zhou NE, Kay CM, Hodges RS. Relationship of sidechain hydrophobicity and α -helical propensity on the stability of the single-stranded amphipathic α -helix. *J Pept Sci*. 1995;1(5):319-329. doi:https://doi.org/10.1002/psc.310010507
127. Mu Y, Yu M. Effects of Hydrophobic Interaction Strength on the Self-Assembled Structures of Model Peptides. *Soft Matter*. 2014;10(27):4956-4965. doi:10.1039/C4SM00378K.
128. Heffernan R, Paliwal K, Lyons J, et al. Improving prediction of secondary structure, local backbone angles and solvent accessible surface area of proteins by iterative deep learning. *Sci Rep*. 2015;5(1):11476. doi:10.1038/srep11476
129. Lins L, Thomas A, Brasseur R. Analysis of accessible surface of residues in proteins. *Protein Science*. 2003;12(7):1406-1417. doi:10.1110/ps.0304803
130. Chou PY, Fasman GD. Conformational parameters for amino acids in helical, β -sheet, and random coil regions calculated from proteins. *Biochemistry*. 1974;13(2):211-222. doi:10.1021/bi00699a001
131. Amirkulova DB, Chakraborty M, White AD. Experimentally Consistent Simulation of A β 21–30 Peptides with a Minimal NMR Bias. *J Phys Chem B*. 2020;124(38):8266-8277. doi:10.1021/acs.jpcc.0c07129
132. Thurston BA, Tovar JD, Ferguson AL. Thermodynamics, morphology, and kinetics of early-stage self-assembly of π -conjugated oligopeptides. *Molecular Simulation*. 2016;42(12):955-975. doi:10.1080/08927022.2015.1125997

133. Guo AZ, Fluit AM, de Pablo JJ. Early-stage human islet amyloid polypeptide aggregation: Mechanisms behind dimer formation. *J Chem Phys.* 2018;149(2):025101. doi:10.1063/1.5033458
134. Shao Q, Wong KM, Seroski DT, et al. Anatomy of a selectively coassembled β -sheet peptide nanofiber. *PNAS.* 2020;117(9):4710-4717. doi:10.1073/pnas.1912810117
135. Kol N, Adler-Abramovich L, Barlam D, Shneck RZ, Gazit E, Rousso I. Self-Assembled Peptide Nanotubes Are Uniquely Rigid Bioinspired Supramolecular Structures. *Nano Lett.* 2005;5(7):1343-1346. doi:10.1021/nl0505896
136. Cinar G, Ceylan H, Urel M, et al. Amyloid inspired self-assembled peptide nanofibers. *Biomacromolecules.* 2012;13(10):3377-3387. doi:10.1021/bm301141h
137. Kalyanasundaram K, Thomas JK. Environmental Effects on Vibronic Band Intensities in Pyrene Monomer Fluorescence and Their Application in Studies of Micellar Systems. *J Am Chem Soc.* 1977;99(7):2039-2044.
138. Castelletto V, Hamley IW. Self assembly of a model amphiphilic phenylalanine peptide/polyethylene glycol block copolymer in aqueous solution. *Biophys Chem.* 2009;141(2-3):169-174. doi:10.1016/j.bpc.2009.01.008
139. Howie AJ, Brewer DB. Optical Properties of Amyloid Stained by Congo Red: History and Mechanisms. *Micron.* 2009;40(3):285-301. doi:10.1016/j.micron.2008.10.002.
140. Hughes M, Frederix PWJM, Raeburn J, et al. Sequence/Structure Relationships in Aromatic Dipeptide Hydrogels Formed under Thermodynamic Control by Enzyme-Assisted Self-Assembly. *Soft Matter.* 2012;8(20):5595-5602. doi:10.1039/C2SM25224D.
141. Pelton JT, McLean LR. Spectroscopic Methods for Analysis of Protein Secondary Structure. *Anal Biochem.* 2000;277(2):167-176. doi:10.1006/abio.1999.4320.
142. Barth A, Zscherp C. What vibrations tell about proteins. *Q Rev Biophys.* 2002;35(4):369-430. doi:10.1017/S0033583502003815
143. Gopal R, Park JS, Seo CH, Park Y. Applications of Circular Dichroism for Structural Analysis of Gelatin and Antimicrobial Peptides. *Int J Mol Sci.* 2012;13(3):3229-3244. doi:10.3390/ijms13033229
144. Clarke DE, Parmenter CDJ, Scherman OA. Tunable Pentapeptide Self-Assembled β -Sheet Hydrogels. *Angew Chem Int Ed.* 2018;57(26):7709-7713. doi:10.1002/anie.201801001
145. Andrushchenko VV, Vogel HJ, Prenner EJ. Solvent-Dependent Structure of Two Trypto-phan-Rich Antimicrobial Peptides and Their Analogs Studied by FTIR and CD Spectroscopy. *Bio-chimica et Biophysica Acta (BBA) - Biomembranes.* 2006;1758(10):1596-1608. doi:10.1016/j.bbamem.2006.07.013.

146. Pashuck ET, Cui H, Stupp SI. Tuning Supramolecular Rigidity of Peptide Fibers through Molecular Structure. *J Am Chem Soc.* 2010;132(17):6041-6046. doi:10.1021/ja908560n
147. Bakota EL, Wang Y, Danesh FR, Hartgerink JD. Injectable Multidomain Peptide Nanofiber Hydrogel as a Delivery Agent for Stem Cell Secretome. *Biomacromolecules.* 2011;12(5):1651-1657. doi:10.1021/bm200035r
148. Bera S, Mondal S, Tang Y, et al. Deciphering the Rules for Amino Acid Co-Assembly Based on Interlayer Distances. *ACS Nano.* Published online 2019:1703-1712. doi:10.1021/acsnano.8b07775
149. Gallivan JP, Dougherty DA. Cation- π interactions in structural biology. *PNAS.* 1999;96(17):9459-9464. doi:10.1073/pnas.96.17.9459
150. Zhao R, Zhang RQ. A new insight into π - π stacking involving remarkable orbital interactions. *Phys Chem Chem Phys.* 2016;18(36):25452-25457. doi:10.1039/C6CP05485D
151. Samanta U, Pal D, Chakrabarti P. Packing of aromatic rings against tryptophan residues in proteins. *Acta Cryst D.* 1999;55(8):1421-1427. doi:10.1107/S090744499900726X
152. Dong H, Paramonov SE, Aulisa L, Bakota EL, Hartgerink JD. Self-Assembly of Multidomain Peptides: Balancing Molecular Frustration Controls Conformation and Nanostructure. *J Am Chem Soc.* 2007;129(41):12468-12472. doi:10.1021/ja072536r
153. Wong KM, Wang Y, Seroski DT, et al. Molecular Complementarity and Structural Heterogeneity within Co-Assembled Peptide β -Sheet Nanofibers. *Nanoscale.* 2020;12(7):4506-4518. doi:10.1039/C9NR08725G.
154. de Pablo JJ, Jackson NE, Webb MA, et al. New frontiers for the materials genome initiative. *Npj Comput Mater.* 2019;5(1):1-23. doi:10.1038/s41524-019-0173-4
155. Sadownik JW, Leckie J, Ulijn RV. Micelle to Fibre Biocatalytic Supramolecular Transformation of an Aromatic Peptide Amphiphile. *Chem Commun.* 2010;47(2):728-730. doi:10.1039/C0CC03796F.
156. Iadanza MG, Jackson MP, Hewitt EW, Ranson NA, Radford SE. A new era for understanding amyloid structures and disease. *Nature Reviews Molecular Cell Biology.* 2018;19(12):755-773. doi:10.1038/s41580-018-0060-8
157. Gallardo R, Ranson NA, Radford SE. Amyloid structures: much more than just a cross- β fold. *Current Opinion in Structural Biology.* 2020;60:7-16. doi:10.1016/j.sbi.2019.09.001

158. Jia Z, Schmit JD, Chen J. Amyloid assembly is dominated by misregistered kinetic traps on an unbiased energy landscape. *Proceedings of the National Academy of Sciences*. 2020;117(19):10322-10328. doi:10.1073/pnas.1911153117
159. Kulenkampff K, Wolf Perez AM, Sormanni P, Habchi J, Vendruscolo M. Quantifying misfolded protein oligomers as drug targets and biomarkers in Alzheimer and Parkinson diseases. *Nat Rev Chem*. 2021;5(4):277-294. doi:10.1038/s41570-021-00254-9
160. Fusco G, Chen SW, Williamson PTF, et al. Structural basis of membrane disruption and cellular toxicity by α -synuclein oligomers. *Science*. 2017;358(6369):1440-1443. doi:10.1126/science.aan6160
161. Milner MT, Maddugoda M, Götz J, Burgener SS, Schroder K. The NLRP3 inflammasome triggers sterile neuroinflammation and Alzheimer's disease. *Current Opinion in Immunology*. 2021;68:116-124. doi:10.1016/j.coi.2020.10.011
162. Tanaka H, Homma H, Fujita K, et al. YAP-dependent necrosis occurs in early stages of Alzheimer's disease and regulates mouse model pathology. *Nat Commun*. 2020;11(1):507. doi:10.1038/s41467-020-14353-6
163. McKenzie BA, Dixit VM, Power C. Fiery Cell Death: Pyroptosis in the Central Nervous System. *Trends in Neurosciences*. 2020;43(1):55-73. doi:10.1016/j.tins.2019.11.005
164. Walsh DM, Selkoe DJ. Amyloid β -protein and beyond: the path forward in Alzheimer's disease. *Current Opinion in Neurobiology*. 2020;61:116-124. doi:10.1016/j.conb.2020.02.003
165. Serrano AL, Lomont JP, Tu LH, Raleigh DP, Zanni MT. A Free Energy Barrier Caused by the Refolding of an Oligomeric Intermediate Controls the Lag Time of Amyloid Formation by hIAPP. *J Am Chem Soc*. 2017;139(46):16748-16758. doi:10.1021/jacs.7b08830
166. Fan J, Lan H, Ning W, et al. Modeling amide-I vibrations of alanine dipeptide in solution by using neural network protocol. *Spectrochimica Acta Part A: Molecular and Biomolecular Spectroscopy*. 2022;268:120675. doi:10.1016/j.saa.2021.120675
167. Kazman P, Absmeier RM, Engelhardt H, Buchner J. Dissection of the amyloid formation pathway in AL amyloidosis. *Nat Commun*. 2021;12(1):6516. doi:10.1038/s41467-021-26845-0
168. Hamsici S, White AD, Acar H. Peptide framework for screening the effects of amino acids on assembly. *Science Advances*. Published online January 2022. doi:10.1126/sciadv.abj0305

169. Gunay G, Hamsici S, Lang GA, Lang ML, Kovats S, Acar H. Peptide Aggregation Induced Immunogenic Rupture (PAIIR). *Advanced Science*. 2022;n/a(n/a):2105868. doi:10.1002/advs.202105868
170. Moujalled D, Strasser A, Liddell JR. Molecular mechanisms of cell death in neurological diseases. *Cell Death Differ*. 2021;28(7):2029-2044. doi:10.1038/s41418-021-00814-y
171. Leong YQ, Ng KY, Chye SM, Ling APK, Koh RY. Mechanisms of action of amyloid-beta and its precursor protein in neuronal cell death. *Metab Brain Dis*. 2020;35(1):11-30. doi:10.1007/s11011-019-00516-y
172. Finn TE, Nunez AC, Sunde M, Easterbrook-Smith SB. Serum Albumin Prevents Protein Aggregation and Amyloid Formation and Retains Chaperone-like Activity in the Presence of Physiological Ligands. *Journal of Biological Chemistry*. 2012;287(25):21530-21540. doi:10.1074/jbc.M112.372961
173. Zhao M, Guo C. Multipronged Regulatory Functions of Serum Albumin in Early Stages of Amyloid- β Aggregation. *ACS Chem Neurosci*. 2021;12(13):2409-2420. doi:10.1021/acchemneuro.1c00150
174. Picón-Pagès P, Bonet J, García-García J, et al. Human Albumin Impairs Amyloid β -peptide Fibrillation Through its C-terminus: From docking Modeling to Protection Against Neurotoxicity in Alzheimer's disease. *Computational and Structural Biotechnology Journal*. 2019;17:963-971. doi:10.1016/j.csbj.2019.06.017
175. Kakinen A, Javed I, Faridi A, Davis TP, Ke PC. Serum albumin impedes the amyloid aggregation and hemolysis of human islet amyloid polypeptide and alpha synuclein. *Biochimica et Biophysica Acta (BBA) - Biomembranes*. 2018;1860(9):1803-1809. doi:10.1016/j.bbamem.2018.01.015
176. Travkova OG, Moehwald H, Brezesinski G. The interaction of antimicrobial peptides with membranes. *Advances in Colloid and Interface Science*. 2017;247:521-532. doi:10.1016/j.cis.2017.06.001
177. Moore AN, Hartgerink JD. Self-Assembling Multidomain Peptide Nanofibers for Delivery of Bioactive Molecules and Tissue Regeneration. *Acc Chem Res*. 2017;50(4):714-722. doi:10.1021/acs.accounts.6b00553
178. Heuvel M van den, Baptist H, Venema P, Linden E van der, M. Löwik DWP, Hest JCM van. Mechanical and thermal stabilities of peptide amphiphile fibres. *Soft Matter*. 2011;7(20):9737-9743. doi:10.1039/C1SM05642E
179. Yakupova EI, Bobyleva LG, Vikhlyantsev IM, Bobylev AG. Congo Red and amyloids: history and relationship. *Biosci Rep*. 2019;39(1):BSR20181415. doi:10.1042/BSR20181415

180. Lakowicz JR, ed. Fluorescence Sensing. In: *Principles of Fluorescence Spectroscopy*. Springer US; 2006:623-673. doi:10.1007/978-0-387-46312-4_19
181. Chan DI, Prenner EJ, Vogel HJ. Tryptophan- and arginine-rich antimicrobial peptides: Structures and mechanisms of action. *Biochimica et Biophysica Acta (BBA) - Biomembranes*. 2006;1758(9):1184-1202. doi:10.1016/j.bbamem.2006.04.006
182. de Jesus AJ, Allen TW. The role of tryptophan side chains in membrane protein anchoring and hydrophobic mismatch. *Biochimica et Biophysica Acta (BBA) - Biomembranes*. 2013;1828(2):864-876. doi:10.1016/j.bbamem.2012.09.009
183. Sawai H, Domae N. Discrimination between primary necrosis and apoptosis by necrostatin-1 in Annexin V-positive/propidium iodide-negative cells. *Biochemical and Biophysical Research Communications*. 2011;411(3):569-573. doi:10.1016/j.bbrc.2011.06.186
184. Hou L, Liu K, Li Y, Ma S, Ji X, Liu L. Necrotic pyknosis is a morphologically and biochemically distinct event from apoptotic pyknosis. *Journal of Cell Science*. Published online January 1, 2016;jcs.184374. doi:10.1242/jcs.184374
185. Savini F, Bobone S, Roversi D, Mangoni ML, Stella L. From liposomes to cells: Filling the gap between physicochemical and microbiological studies of the activity and selectivity of host-defense peptides. *Peptide Science*. 2018;110(5):e24041. doi:10.1002/pep2.24041
186. Andrade S, Loureiro JA, Pereira MC. The Role of Amyloid β -Biomembrane Interactions in the Pathogenesis of Alzheimer's Disease: Insights from Liposomes as Membrane Models. *ChemPhysChem*. 2021;22(15):1547-1565. doi:10.1002/cphc.202100124
187. Horger KS, Estes DJ, Capone R, Mayer M. Films of Agarose Enable Rapid Formation of Giant Liposomes in Solutions of Physiologic Ionic Strength. *J Am Chem Soc*. 2009;131(5):1810-1819. doi:10.1021/ja805625u
188. Chibowski E, Szcześ A. Zeta potential and surface charge of DPPC and DOPC liposomes in the presence of PLC enzyme. *Adsorption*. 2016;22(4-6):755-765. doi:10.1007/s10450-016-9767-z
189. Arosio P, Knowles TP, Linse S. On the lag phase in amyloid fibril formation. *Physical Chemistry Chemical Physics*. 2015;17(12):7606-7618. doi:10.1039/C4CP05563B
190. Stanyon HF, Viles JH. Human Serum Albumin Can Regulate Amyloid- β Peptide Fiber Growth in the Brain Interstitium: IMPLICATIONS FOR ALZHEIMER DISEASE *. *Journal of Biological Chemistry*. 2012;287(33):28163-28168. doi:10.1074/jbc.C112.360800

191. Biancalana M, Koide S. Molecular mechanism of Thioflavin-T binding to amyloid fibrils. *Biochimica et Biophysica Acta (BBA) - Proteins and Proteomics*. 2010;1804(7):1405-1412. doi:10.1016/j.bbapap.2010.04.001
192. Sang JC, Lee JE, Dear AJ, et al. Direct observation of prion protein oligomer formation reveals an aggregation mechanism with multiple conformationally distinct species. *Chem Sci*. 2019;10(17):4588-4597. doi:10.1039/C8SC05627G
193. Ziaunys M, Sakalauskas A, Sneideris T, Smirnovas V. Lysozyme Fibrils Alter the Mechanism of Insulin Amyloid Aggregation. *International Journal of Molecular Sciences*. 2021;22(4):1775. doi:10.3390/ijms22041775
194. Makwana PK, Jethva PN, Roy I. Coumarin 6 and 1,6-diphenyl-1,3,5-hexatriene (DPH) as fluorescent probes to monitor protein aggregation. *Analyst*. 2011;136(10):2161-2167. doi:10.1039/C0AN00829J
195. Kumar P, Nagarajan A, Uchil PD. Analysis of Cell Viability by the Lactate Dehydrogenase Assay. *Cold Spring Harb Protoc*. 2018;2018(6):pdb.prot095497. doi:10.1101/pdb.prot095497
196. Lichlyter DJ, Grant SA, Soykan O. Development of a novel FRET immunosensor technique. *Biosensors and Bioelectronics*. 2003;19(3):219-226. doi:10.1016/S0956-5663(03)00215-X
197. Irwin M, Tare M, Singh A, et al. A Positive Feedback Loop of Hippo- and c-Jun-Amino-Terminal Kinase Signaling Pathways Regulates Amyloid-Beta-Mediated Neurodegeneration. *Front Cell Dev Biol*. 2020;8:117. doi:10.3389/fcell.2020.00117
198. Hao Y, Chun A, Cheung K, Rashidi B, Yang X. Tumor Suppressor LATS1 Is a Negative Regulator of Oncogene YAP. *Journal of Biological Chemistry*. 2008;283(9):5496-5509. doi:10.1074/jbc.M709037200
199. Abylkassov R, Xie Y. Role of Yes-associated protein in cancer: An update. *Oncology Letters*. 2016;12(4):2277-2282. doi:10.3892/ol.2016.4955
200. Bond S, Lopez-Lloreda C, Gannon PJ, Akay-Espinoza C, Jordan-Sciutto KL. The Integrated Stress Response and Phosphorylated Eukaryotic Initiation Factor 2 α in Neurodegeneration. *Journal of Neuropathology & Experimental Neurology*. 2020;79(2):123-143. doi:10.1093/jnen/nlz129
201. Ohno M. Roles of eIF2 \pm kinases in the pathogenesis of Alzheimer's disease. *Front Mol Neurosci*. 2014;7. doi:10.3389/fnmol.2014.00022
202. Chang RCC, Wong AKY, Ng HK, Hugon J. Phosphorylation of eukaryotic initiation factor-2 α (eIF2 α) is associated with neuronal degeneration in Alzheimer's disease: *NeuroReport*. 2002;13(18):2429-2432. doi:10.1097/00001756-200212200-00011

203. Lee DY, Lee KS, Lee HJ, et al. Activation of PERK Signaling Attenuates A β -Mediated ER Stress. Feany MB, ed. *PLoS ONE*. 2010;5(5):e10489. doi:10.1371/journal.pone.0010489
204. Yerlikaya A, Kimball SR, Stanley BA. Phosphorylation of eIF2 α in response to 26S proteasome inhibition is mediated by the haem-regulated inhibitor (HRI) kinase. *Biochemical Journal*. 2008;412(3):579-588. doi:10.1042/BJ20080324
205. Saiki M, Shiba K, Okumura M. Structural stability of amyloid fibrils depends on the existence of the peripheral sequence near the core cross- β region. *FEBS Letters*. 2015;589(23):3541-3547. doi:10.1016/j.febslet.2015.10.015
206. Chiti F, Dobson CM. Protein misfolding, functional amyloid, and human disease. *Annu Rev Biochem*. 2006;75:333-366. doi:10.1146/annurev.biochem.75.101304.123901
207. Sipe JD, Benson MD, Buxbaum JN, et al. Nomenclature 2014: Amyloid fibril proteins and clinical classification of the amyloidosis. *Amyloid*. 2014;21(4):221-224. doi:10.3109/13506129.2014.964858
208. Linse S. Mechanism of amyloid protein aggregation and the role of inhibitors. *Pure and Applied Chemistry*. 2019;91(2):211-229. doi:10.1515/pac-2018-1017
209. R. Sahoo B, J. Cox S, Ramamoorthy A. High-resolution probing of early events in amyloid- β aggregation related to Alzheimer's disease. *Chemical Communications*. 2020;56(34):4627-4639. doi:10.1039/D0CC01551B
210. Stefani M. Biochemical and biophysical features of both oligomer/fibril and cell membrane in amyloid cytotoxicity. *The FEBS Journal*. 2010;277(22):4602-4613. doi:10.1111/j.1742-4658.2010.07889.x
211. Luheshi LM, Tartaglia GG, Brorsson AC, et al. Systematic In Vivo Analysis of the Intrinsic Determinants of Amyloid β Pathogenicity. *PLOS Biology*. 2007;5(11):e290. doi:10.1371/journal.pbio.0050290
212. Hane F, Leonenko Z. Effect of Metals on Kinetic Pathways of Amyloid- β Aggregation. *Biomolecules*. 2014;4(1):101-116. doi:10.3390/biom4010101
213. Hamsici S, Gunay G, Acar H. Controllable membrane damage by tunable peptide aggregation with albumin. *AIChE Journal*. 2022;n/a(n/a):e17893. doi:10.1002/aic.17893
214. Meisl G, Kirkegaard JB, Arosio P, et al. Molecular mechanisms of protein aggregation from global fitting of kinetic models. *Nat Protoc*. 2016;11(2):252-272. doi:10.1038/nprot.2016.010

215. Cecchi C, Stefani M. The amyloid-cell membrane system. The interplay between the biophysical features of oligomers/fibrils and cell membrane defines amyloid toxicity. *Biophysical Chemistry*. 2013;182:30-43. doi:10.1016/j.bpc.2013.06.003
216. Kuperstein I, Broersen K, Benilova I, et al. Neurotoxicity of Alzheimer's disease A β peptides is induced by small changes in the A β 42 to A β 40 ratio. *EMBO J*. 2010;29(19):3408-3420. doi:10.1038/emboj.2010.211
217. Cizas P, Budvytyte R, Morkuniene R, et al. Size-dependent neurotoxicity of beta-amyloid oligomers. *Arch Biochem Biophys*. 2010;496(2):84-92. doi:10.1016/j.abb.2010.02.001
218. Venegas C, Heneka MT. Danger-associated molecular patterns in Alzheimer's disease. *Journal of Leukocyte Biology*. 2017;101(1):87-98. doi:10.1189/jlb.3MR0416-204R
219. Heneka MT, Kummer MP, Latz E. Innate immune activation in neurodegenerative disease. *Nat Rev Immunol*. 2014;14(7):463-477. doi:10.1038/nri3705
220. Bolognesi B, Kumita JR, Barros TP, et al. ANS Binding Reveals Common Features of Cytotoxic Amyloid Species. *ACS Chem Biol*. 2010;5(8):735-740. doi:10.1021/cb1001203
221. Kaye R, Head E, Thompson JL, et al. Common Structure of Soluble Amyloid Oligomers Implies Common Mechanism of Pathogenesis. *Science*. 2003;300(5618):486-489. doi:10.1126/science.1079469
222. C. Lee SJ, Nam E, Jin Lee H, G. Savelieff M, Hee Lim M. Towards an understanding of amyloid- β oligomers: characterization, toxicity mechanisms, and inhibitors. *Chemical Society Reviews*. 2017;46(2):310-323. doi:10.1039/C6CS00731G
223. Menendez-Gonzalez M, Gasparovic C. Albumin Exchange in Alzheimer's Disease: Might CSF Be an Alternative Route to Plasma? *Front Neurol*. 2019;10:1036. doi:10.3389/fneur.2019.01036
224. Oropesa-Nuñez R, Seghezza S, Dante S, et al. Interaction of toxic and non-toxic HypF-N oligomers with lipid bilayers investigated at high resolution with atomic force microscopy. *Oncotarget*. 2016;7(29):44991-45004. doi:10.18632/oncotarget.10449
225. Berghe TV, Vanlangenakker N, Parthoens E, et al. Necroptosis, necrosis and secondary necrosis converge on similar cellular disintegration features. *Cell Death Differ*. 2010;17(6):922-930. doi:10.1038/cdd.2009.184
226. Efimova I, Catanzaro E, Van der Meeren L, et al. Vaccination with early ferroptotic cancer cells induces efficient antitumor immunity. *J Immunother Cancer*. 2020;8(2):e001369. doi:10.1136/jitc-2020-001369

227. Tesniere A, Schlemmer F, Boige V, et al. Immunogenic death of colon cancer cells treated with oxaliplatin. *Oncogene*. 2010;29(4):482-491. doi:10.1038/onc.2009.356
228. Oli AN, Oli UC, Ejiofor OS, Nwoye CU, Esimone CO. An assessment, in mice, of the safety of the childhood immunization vaccines sourced from three south-eastern states of Nigeria. *Trials in Vaccinology*. 2016;5:8-14. doi:10.1016/j.trivac.2015.10.001
229. Martin TA, Ye L, Sanders AJ, Lane J, Jiang WG. *Cancer Invasion and Metastasis: Molecular and Cellular Perspective*. Landes Bioscience; 2013. Accessed October 9, 2020. <https://www.ncbi.nlm.nih.gov/books/NBK164700/>